Democratic and Popular Republic of Algeria
Ministry of Higher Education and Scientific Research
Echahid Hamma Lakhdar University of El-Oued
Faculty of Technology
Electrical engineering department

Doctorate Thesis

Submitted in fulfilment of the requirements for the degree of
Doctor of Science in Electronics

Entitled :

Study and optimization of perovskite-based solar cells

by
Abdelkader HIMA

Examination committee:

Pr. BOUBAKER BENHOUA	Professor	Chairman	University of El oued
Dr. NACEREDDINE LAKHDAR	M.C.A	Supervisor	University of El oued
Dr. BRAHIM LAKEHAL	M.C.A	Examiner	University of Batna2
Dr. SOUHIL KOUDA	M.C.A	Examiner	University of Batna2
Dr. ABDELKADER MEDJOURI	M.C.A	Examiner	University of El oued

2020

Abstract

Renewable energy technologies are in plain evolution due to the international demand of electric power and the pollutant fossil energy depletion. Since a while, Researches in the field of solar energies are in exponential evolution, and the use of new generation photovoltaics is attracting researchers attention. One of the most new generation solar cell promising technologies is the introduction of perovskite materials. These latter have some important characteristics suitable for solar energy harvesting namely adapted band gap to solar radiation absorption, abundant materials in the nature, low cost processing and excellent absorption factor. In this thesis, solar cells based on perovskite materials have been proposed and investigated in order to enhance the power conversion efficiency of the devices. These materials include methyl ammonium lead tri-iodide ($MAPbI_3$), methyl ammonium tin tri-iodide ($MASnI_3$) and methyl ammonium germanium tri-iodide ($MAGeI_3$). Different structures of solar cells based on $MAPbI_3$ and $MASnI_3$ are numerically modeled using the ATLAS-Silvaco and SCAPS softwares to improve their performances. Therefore, an optimization process is applied to these structures to find the better power conversion efficiency of solar cells. In addition, Ge-perovskite solar cell designs are studied and investigated to improve the performance of these devices. Moreover, diverse kinds of electron transporting layers (ETLs) and hole transporting layers (HTLs) are inserting in Ge-perovskite solar cell in order to enhance the power conversion efficiency of perovskite devices. Found results shows that the n-i-p structure of $TiO_2 \setminus MASnI_3 \setminus$ spiro-OMeTAD with layer thickness of 100 nm, 500 nm, and 200 nm respectively gives a Power conversion efficiency of 9.56%. It is to underline the new proposed and optimized structure based on non-toxic p-i-n structure $CuSBS_2 \setminus CH_3NH_3GeI_3 \setminus C_{60}$ with layer thickness of 50 nm, 950 nm, and 50 nm respectively gives a high power conversion efficiency of 23.58%. Thus, the obtained results potentialy provide a guidance for design and fabrication of future Ge-perovskite solar cells for enhanced power conversion efficiency.

Keywords : Perovskite, Photovoltaic solar cell, Silvaco Atlas, SCAPS, I-V characteristics, power conversion efficiency.

ملخص

إن تكنولوجيات الطاقة المتجددة في تطور مضطرد وذلك راجع للطلب العالمي المتزايد على الطاقة الكهربائية واستنفاد الطاقة الأحفورية الملوثة. منذ فترة، أصبحت الأبحاث في مجال الطاقات الشمسية في تطور هائل ، كما أن استخدام الجيل الجديد من الخلايا الكهروضوئية جذب انتباه الباحثين. إحدى أحدث التقنيات الواعدة في مجال تطوير الخلايا الشمسية هي إدخال مواد البيروفسكايت. تحتوي هذه الفئة من المواد على بعض الخصائص المهمة المناسبة لامتصاص الطاقة الشمسية نذكر منها الحزمة النافذة المناسبة لامتصاص الإشعاع الشمسي، وفرة هذه المواد في الطبيعة، التكلفة المنخفضة للمعالجة وكذا عامل الامتصاص الممتاز. في هذه الأطروحة، تم تصميم ودراسة مجموعة من الخلايا الكهروضوئية المعتمدة على بعض من مواد البيروفسكايت بهدف تحسين المردود الطاقوي لها. هذه المواد تضم مثيل أمونيوم الرصاص ثلاثي الأيوديد ($MAPbI_3$) ومثيل أمونويم القصدير ثلاثي الأيوديد ($MASnI_3$) ومثيل أمونويم الجرمانيوم ثلاثي الأيوديد ($MAGeI_3$). تمت محاكاة ونمذجة عدة بنى لخلايا كهروضوئية متكونة من $MAPbI_3$ و$MASnI_3$ باستخدام برنامجي سيلفاكو أطلس وسكابس بغية تحسين خصائصها. وعليه، تم تطبيق خوارزمية تحسين على هذه البنى للحصول على أفضل مردود طاقوي للخلايا الكهروضوئية. بالموازاة، تم دراسة ونمذجة تصاميم لخلايا شمسية تعتمد على بيروفسكايت الجرمانيوم من أجل تحسين خصائصها. كما تم التطرق إلى إدراج مختلف طبقات نقل الإلكترونات (ETL) وطبقات نقل الثقوب (HTL) للخلايا الشمسية المعتمدة على بيروفسكايت الجرمانيوم من أجل تحسين المردود الطاقوي لأجهزة البيروفسكايت. النتائج المتحصل عليها تبين أن البنية TiO_2\$MASnI_3$\spiro-OMeTAD n-i-p ذات السمك الطبقي 100 nm، 500 nm و200 nm على التوالي تنتج مردود طاقوي قدره 9.56 %. كما أنه يجدر الإشارة إلى البنية الجديدة التي تحصلنا عليها وهي غير سامة من النوع p-i-n $CuSBS_2$\$MAGeI_3$\$C_{60}$ ذات السمك الطبقي 50 nm، 950 nm و50 nm على التوالي والتي أعطت مردودا طاقويا قيمته 23.58%. وعليه فقد تحصلنا على نتائج جد مهمة توفر للمصممين والمصنعين المستقبليين لبيروفسكايت الجرمانيوم تصورا جيدا عن المردود الطاقوي الأمثل.

الكلمات المفتاحية

البيروفسكايت، الخلايا الكهروضوئية، سيلفاكو أطلس، الخاصية I-V، مردود التحويل الطاقوي.

Résumé

Les technologies des énergies renouvelables sont en évolution accrue en raison de l'augmentation de la demande internationale en puissance électrique et de l'épuisement des énergies fossiles polluantes. Depuis un certain temps, les recherches dans le domaine des énergies solaires connaissent une évolution exponentielle et l'utilisation des systèmes photovoltaïques de nouvelle génération attire l'attention des chercheurs. L'introduction des matériaux à base de pérovskite est l'une des technologies les plus prometteuses en matière de cellules solaires. Cette dernière classe de matériaux présente certaines caractéristiques importantes adaptées à la récolte d'énergie solaire, à savoir une bande interdite adaptée à l'absorption du rayonnement solaire, des matériaux abondants dans la nature, un traitement à faible coût et un excellent facteur d'absorption. Dans cette thèse, nous avons proposé et étudié des matériaux pérovskites pour améliorer le rendement en puissance des dispositifs photovoltaïque. Ces matériaux englobent le méthylammonium plomb tri-iodure ($MAPbI_3$), le méthylammonium étaint tri-iodure ($MASnI_3$) et le méthylammonium germanium tri-iodure ($MAGeI_3$). En utilisant les matériaux $MAPbI_3$ et $MASnI_3$, nous avons analysé numériquement des cellules solaires de structures différentes à l'aide des logiciels Silvaco Atlas et SCAPS afin d'améliorer leurs performances. Ainsi, un processus d'optimisation a été appliqué sur ces structures dans le but d'en atteindre la valeur optimale de rendement en puissance des cellules solaires. En outre, des cellules solaires à base de Ge ont été étudiés et optimisés afin d'améliorer les performances de ces dispositifs. En plus, différents types de couches de transport d'électrons (ETL) et celles de trous (HTL) ont été insérés dans les cellules solaire basées sur le perovskite à Ge afin d'augmenter les performances des dispositifs à pérovskites. Les résultats obtenues montrent que la structure n-i-p $TiO_2 \setminus MASnI_3 \setminus$ spiro-OMeTAD avec les épaisseurs de couches de 100 nm, 500 nm, et 200 nm respectivement donne un rendement en psuissance de 9.56%. Il est à souligner que la nouvelle structure non-toxique p-i-n $CuSBS_2 \setminus CH_3NH_3GeI_3 \setminus C_{60}$ avec les épaisseurs de couches de 50 nm, 950 nm, et 50 nm respectivement donne un rendement énergétique de 23.58%. Par conséquent, les résultats obtenues fournissent un guide potentiel pour la conception et la réalisation de future cellules solaires à base de pérovskite à germanium avec un rendement élevé.

Mots clés : Perovskite, cellules photovoltaïques, Silvaco Atlas, SCAPS, Charactéristique I-V, rendement de convertion en puissance.

DEDICATION

I dedicate this modest work :
To the man of my life, my eternal example, my moral support and source of joy and happiness, the one who has always sacrificed himself for me to succeed, may god keep you in his vast paradise, you my father.
To the light of my days, the source of my efforts, the flame of my heart, my life and my happiness, mother that I adore.
Special dedication to my wife, Soumaya for her support, advice, tolerance, patience and trust in me.
To the people of whom I enjoyed the presence in this day, to my sons Mohamed, Djasser and the chick Ghaith and my dear daughter Souha, I dedicate this work whose great pleasure comes back to them first and foremost for their advice, and encouragement.
To the people who always helped and encouraged me, who were always by my side, and who accompanied me on my way to achieve this thesis, my kind friends, colleagues of study and colleagues of work.
I say thank you

ACKNOWLEDGMENT

Firstly, I thank Allah, the Most High, for the opportunity He gave me to study, to research and to write this thesis. Thank Allah, my outmost thanks, for giving me the ability, the strength, attitude and motivation through this research and to complete this work.

My greetings to my research director Dr. Lakhdar Nacereddine for his helpful efforts and guidance throughout this work.

A very special gratitude goes out to Pr. BENHAOUA Boubaker for accepting to be the president of my oral examination committee.

Warm thanks for the oral examination committee for accepting to judge this modest work namely : Dr. KOUDA Souhil, Dr. LAKEHAL Brahim and Dr. MEDJOURI Abdelkader.

TABLE OF CONTENTS

LIST OF FIGURES

LIST OF TABLES

ABREVIATIONS AND NOMENCLATURE

Abreviations

AM1.5 Normalized air mass spectrum

CuI Copper Iodide

ETL Electron transporting layer

GW Green's function and Wick's theorem of density functional theory

HOMO Highest occupied molecular orbital

HTL Hole transporting layer

LUMO Lowest unoccupied molecular orbital

$MAGeI_3$ Methyl ammonium germanium tri-iodide

$MAPbBr_3$ Methyl ammonium leade tri-bromide

$MAPbCl_3$ Methyl ammonium leade tri-chloride

$MAPbI_3$ Methyl ammonium leade tri-iodide

$MAPbI_{3-x}Br_x$ Mixed methyl ammonium leade iodide-bromide

$MAPbI_{3-x}Cl_x$ Mixed methyl ammonium leade iodide-chloride

$MASnI_3$ Methyl ammonium tin tri-iodide

NREL National renewable energy laboratory

P3HT poly(3- hexylthiophene-2.5- diyl)

PCE Power convertion efficiency

PTAA poly(thiophene-3- acetic acid)

PVK Perovskite

spiro-OMeTAD 2.2′.7.7′-tetrakis(N.N-di-p-methoxyphenylamine)-9.9′ -spirobiflu-orene

SRH Shockley-Read-Hall

Nomenclature

A Cross section area

A_α Absorption pre-factor

A^* Material dependant constant

A^{**} Material dependant constant

α Absorption coefficient

c Speed of light

χ Electron affinity

D Diffusion coefficient

D_n Diffusion coefficient of electrons

D_p Diffusion coefficient of hole

E Electric field

Ec Lower energy level in the conduction band

$E_{cbottom}$ Bottom energy of the conduction band

E_{ctop} Top energy of the conduction band

E_F Fermi level

E_{Fn} Quazi-Fermi level of electons in the conduction band

E_{Fp} Quazi-Fermi level of holes in the valence band

Eg Band gap energy

E_p Phonen energy associated at the absorption

ϵ Local permittivity

ϵ_r Relative permittivity

η Power conversion efficiency

Ev Higher energy level in the valence band

$E_{vbottom}$ Bottom energy of the valence band

E_{vtop} Top energy of the valence band

F_0 Normally photon Flux

$f(E)$ Probability that an electron state is occupied

FF Fill factor

$g_c(E)$ Density of states function

G_n Generation rate for electrons

G_p Generation rate for holes

h Constant of Planck

I_L Photogenerated current

I_m Current at the optimum operating point

I_n Electron current

I_p Hole current

Isc Short circuit current

J_0 Saturation current density

$J_{diffusion}$ Total diffusion current density

J_{drift} Drift current density

J_n Electron current density

J_{ndiff} Diffusion current density of electrons

J_p Hole current density

J_{pdiff} Diffusion current density of holes

Jsc Short circuit dencity of current

J Total current density

k Boltzmann constant

L Diffusion length of carriers

λ Photon wavelength

m_n Effective mass of the electron

m_p Effective mass of the hole

μ Mobility

μ_n Electron mobility

μ_{n0} Zero field Pool-Frenkel electron mobility

μ_p Hole mobility

μ_{p0} Zero field Pool-Frenkel hole mobility

n Electron concentration

n_n^0 Electron concentration in the n-doped region in thermal equilibrium

N_A Concentration of acceptors

N_D Concentration of donors

n_i Concentration of intrinsic carriers

ν Light frequency

p Hole concentration

p_p^0 Hole concentration in the p-doped region in thermal equilibrium

P_{in} Total incident light power

ψ Electrostatic potencial

q Electric charge

R Reflectivity of the surface to normally incident light

ρ Local space charge density

R_n Recombination rate for electrons

R_p Recombination rate for holes

R_s Series resistance

R_{sh} Shunt resistance

σ Conductivity

T Absolute temperature

τ Lifetime of carriers

τ_c Mean free time

τ_n Lifetime of electrons

τ_p Lifetime of holes

V_b Built in potencial

V_m Voltage at the optimum operating point

v_n Drift velocity of electron

Voc Open circuit voltage

v_p Drift velocity for holes

INTRODUCTION

Nowadays, with the rapid increase of global energy consumption and the exhaustion of polluted fossil fuel reserves, a sustainable and clean energy become of primary interest for the humanity and the environment. In the present era, there are many renewable energy sources, including but not limited to: wind power, wave energy and solar energy. One of the most promising renewable source of power is the photovoltaic energy which was discovered firstly in 1839 by the French physicist Becquerel. Later, in 1883, Fritts fabricated the first successful semiconductor/metal junction with a power conversion efficiency (PCE) of approximately 1% using selenium. After 70 years, a group of researcher from the US Bell Labs (Parson et al.) fabricated a solar cell that reached a PCE of 4.5% using crystalline silicon [1]. One of the most innovative photovoltaic technologies is the perovskite based solar cell. This new technology have achieved high PCE values within a decade [2]. Perovskite materials are appropriate for light harvesting due to their high absorbance, long electron/hole life time, low processing costs and material abundance in the nature.

In the last few years, there has been a surge of interest in the use of perovskite materials in photovoltaic solar cell research has developed exponentially [3], prompting researchers to invest in research to improve the performance of perovskite based photovoltaic cells as well as trying to understand the various internal mechanisms that control several characteristics, including hysteresis [4–8], power conversion efficiency [9–14] and stability [15–18]. In this context, power conversion efficiency of perovskite based solar cells was stepped from 3.8% in 2009 [19] up to 22.1% in 2016 [20] and then to 25.2 % in 2019 [21, 22]. This latter

can be affected by many parameters such as fabrication technology and process [23–25], electron transport material choice and parameters [26,27], hole transport material choice and parameters [28–30], thickness of different layers [31,32] and optical and electrical parameter tuning [33].

Recently, many authors have reported simulations for perovskite based solar cell using free device softwares such as SCAPS [34,35], wxAMPS [36] and GPVDM [37] which are based on one physical model : the drift diffusion transport model. To reach a closer simulated model that describes experimental results, SILVACO ATLAS device software [38] presents a large multitude of physical models including drift diffusion transport model. It has different material models (for organic and inorganic) for recombination and mobility to help users doing the best choice for each material making them closer to experimental behavior. Furthermore, it is based on resolving of different equations mainly Poisson's equation and carrier continuity equations for electrons and holes.

The key idea of this thesis is to study and optimize different perovskite solar cell designs in order to enhance their electrical and optical parameters. Therefore, Pb, Sn and Ge-based perovskite solar cell structures are investigated and optimized by incorporating of different electron transporting layer (ETL) and hole transporting layer (HTL) to improve the electrical performances for future high stability and high efficiency perovskite solar cells.

LAYOUT OF THE THESIS

This thesis is organized as follows :

Chapter 1, in which principal required knowledge on semiconductor physics are presented. Then, an overview of solar cell fundamentals is exhibited to help beginners have the necessary terminology used in the field of photovoltaics. The second chapter highlights necessary skills needed to explore perovskite material characteristics and working principals. Also, it presents different perovskite solar cell structures and diverse hole and electron transporting materials used in perovskite solar cells.

Detailed description of both software simulation programs : Silvaco Atlas and Solar Cell Capacitance Simulator (SCAPS) used in this work are given in chapter three.

Simulation and optimization of different PVK solar cell structures using both perovskite materials $MAPbI_3$ and $MASnI_3$ are reported in chapter four. In chapter five, numerical modeling of $MAGeI_3$ based solar cells are proposed and studied. In addition, both ETL and HTL effect on performances of perovskite solar cells are dedicated in this chapter. In conclusion, some suggestions for future perovskite solar cells are included.

CHAPTER 1

SOLAR CELL FUNDAMENTALS

1.1 Introduction

Solar cell is the basic component in a photovoltaic system that converts light energy into electrical energy. For the fabrication of solar cells, a semiconductor material is used in most cases. The power transformation mechanism from light to electricity consists of absorbing photon energy to generate pairs of electron–hole in a semiconductor and thus splitting the charge carrier. The PN junction is generally the main charge carrier splitting device. Accordingly, the analysis of solar cell-based PN junction will offer us clues to optimize these devices with respect to many parameters, namely but not restricted to : power conversion efficiency, processing expenses, production process energy consumption, production equipment, etc.

The main parameters of the semiconductor that can determine a solar cell's structure and efficiency are:

1. Doping concentration of atoms that has two different types: atoms of donors that donate free electrons or atoms of acceptors that accept electrons. The atom concentrations of donor and acceptor are denoted respectively by N_D and N_A and determine the width of a junction's space-charge region.

2. Mobility μ and charge carriers ' diffusion coefficient D are used to define carriers ' motion relative to drift and diffusion processes, respectively.

3. The overabundance carriers ' lifetime τ and diffusion length L depict the procedures of recombination-generation.

4. The band gap energy Eg, and the α absorption coefficient portray a semiconductor's capacity to absorb optical radiation.

This chapter highlights the fundamental characteristics of semiconductors, some features of standard PN junction, and the fundamentals of solar cells to recognize not only ordinary solar cells, but also the latest solar cell type.

1.2 Principal properties of semiconductors

1.2.1 Energy bands and carriers concentration

For floating electron clouds, the atoms of a given material have orbits, each orbit is characterized by a discrete level of energy. Due to nuclear interaction, which produces a continuous energy band, once in crystal material condition, the energy levels separated into detached but tightly spaced levels. The lower energy level in the upper energy band is called the conduction band and denoted Ec, the upper energy level in the lower energy band is called the valence band and denoted Ev and the energy gap Ec - Ev is called the band gap Eg which is an important parameter in solar cell [39] (see Figure 1.1).

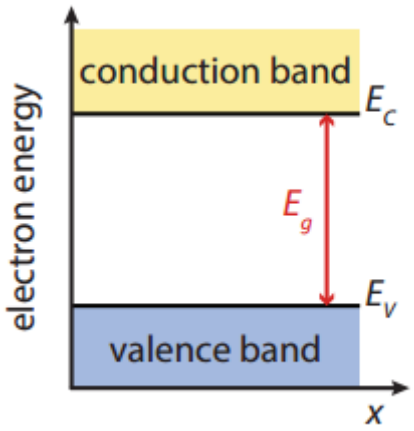

Figure 1.1 – Energy bands representation of intrinsic semiconductors.

In $0°K$, all the conduction band's energy levels are full of electrons, and the valence band's energy levels are empty. Some bonds begin to break at room temperature due to the absorbed thermal energy, resulting in mobile electrons and holes being created (see Figure 1.2).

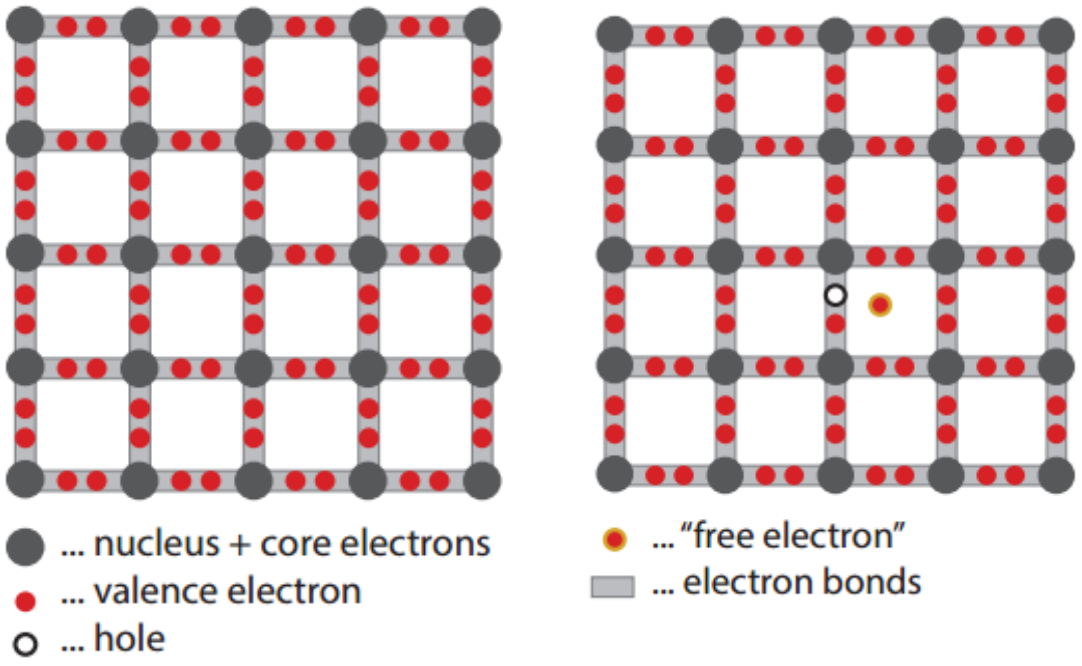

(a) With no broken bonds

(b) With broken bonds

Figure 1.2 – Bonding samples.

In Figure 1.2a, the unbroken bonds are shown in a crystalline state of a specified sample material, and in Figure 1.2b, the impact of bond break that produces free electron leaving a hole in the bond is shown. The bond's left hole allows a neighborhood electron to jump into this vacant place and restore the bond. This mechanism will be repeated sequentially producing in opposite directions displacement a of couple of electron hole [39].

An intrinsic material is categorized by a number of free thermally generated electron/hole pairs that are much larger than the number of electron-hole pairs generated by internal impurities. The concentration of electrons in intrinsic materials is equal to that of holes. For instance, there are about $1.5 \times 10^{10} cm^{-3}$ broken bonds in intrinsic silicon (Si) at $300°K$. This amount gives the concentration of the hole p and the concentration of the electron n in the intrinsic material with $n = p = 1.5 \times 10^{10} cm^{-3}$ at $300°K$. In that case, this density is called concentration of the intrinsic carrier denoted n_i.

The electron concentration in the conduction band can be written as:

$$n = \int_{E_{cbottom}}^{E_{ctop}} g_c(E) \times f(E) \times dE \tag{1.1}$$

Where $E_{cbottom}$ is the bottom energy of the conduction band, E_{ctop} denotes the top energy of the conduction band, $g_c(E)$ is the density of states and $f(E)$ is the probability that an electron state is occupied.

Assuming that $g_c(E)$ and $f(E)$ (called also the Fermi-Dirac distribution function) are given by equations 1.2 and 1.3 respectively, n is obtained from 1.4 :

$$g_c(E) = \left(\frac{4\sqrt{2}\pi m_n}{h^3}\right)^{\frac{3}{2}} (E - Ec)^{\frac{1}{2}} \tag{1.2}$$

$$f(E) = \frac{1}{1 + e^{\frac{E-E_F}{kT}}} \approx e^{(-\frac{E-E_F}{kT})} \tag{1.3}$$

$$n = 2\left(\frac{2\pi m_n kT}{h^2}\right)^{\frac{3}{2}} \exp\left(-\frac{Ec - E_F}{kT}\right) = Nc \exp\left(-\frac{Ec - E_F}{kT}\right) \tag{1.4}$$

Where E_F denotes the Fermi level, k is the Boltzmann constant, T presents the absolute temperature, m_n is the effective mass of the electrons, h is the Planck's constant, and Nc is the effective density of states of electrons in the conduction band.

Similarly, equations 1.5, 1.6 and 1.3 can be used to calculate the concentration of holes p in the valence band which is expressed by equation 1.7 :

$$p = \int_{E_{vbottom}}^{E_{vtop}} g_v(E) \times (1 - f(E)) \times dE \tag{1.5}$$

$$g_v(E) = \left(\frac{4\sqrt{2}\pi m_p}{h^3}\right)^{\frac{3}{2}} (E - Ev)^{\frac{1}{2}} \tag{1.6}$$

$$p = 2\left(\frac{2\pi m_p kT}{h^2}\right)^{\frac{3}{2}} \exp\left(\frac{Ev - E_F}{kT}\right) = Nv \exp\left(\frac{Ev - E_F}{kT}\right) \tag{1.7}$$

Where E_{vtop} is the top energy of the valence band, $E_{vbottom}$ denotes the bottom energy of the valence band, $g_v(E)$ is the density of states, m_p presents the effective mass of the holes, and Nv denotes the effective density of states of holes in the valence band.

If the product of $p \times n$ is taken we will get the following equation:

$$\begin{aligned} pn = n_i^2 &= NcNv \exp\left(\tfrac{Ev-Ec}{kT}\right) \\ &= NcNv \exp\left(-\tfrac{Eg}{kT}\right) \end{aligned} \tag{1.8}$$

It is clear from 1.8 that n_i is independent of the Fermi level position. In the case of intrinsic material we have $n = p = n_i$ as :

$$\begin{aligned} n_i &= Nc \exp\left(\frac{E_F - Ec}{kT}\right) \\ &= Nv \exp\left(\frac{Ev - E_F}{kT}\right) \end{aligned} \tag{1.9}$$

From equation 1.9 it is easy to deduce E_F :

$$\begin{aligned} E_F &= \frac{Ec+Ev}{2} + \frac{kT}{2} \ln\left(\frac{Nv}{Nc}\right) \\ &= Ec - \frac{Eg}{2} + \frac{kT}{2} \ln\left(\frac{Nv}{Nc}\right) \end{aligned} \tag{1.10}$$

An extrinsic material is characterized by a number of free thermal generated pairs electron-hole much lower than the number of pairs electron-hole generated from inner impurities. In the case of Si doped by V group atoms such as phosphorus (P), four electrons form covalent bonds with its four neighboring Si atoms. The fifth electron stays free, and consequently, it becomes a conduction electron with negative charge. In this circumstances, the Si material is called n-type semiconductor, and P material is called Donor. The electron (majority carriers) concentration is given by $n = N_D$, where N_D is the donor concentration. The hole (minority) concentration is obtained from the expression 1.8 as:

$$p = \frac{n_i^2}{N_D} \tag{1.11}$$

and hence, the Fermi level can be expressed by:

$$Ec - E_F = kT \ln \frac{Nc}{N_D} \tag{1.12}$$

for n-type materials.

Similarly, in the case of Si doped by III group atoms such as boron (B), three electrons form covalent bonds with its three neighboring Si atoms. The fourth hole stays free, and consequently, it becomes a conduction hole with positive charge. In this circumstances, the Si material is called p-type semiconductor, and B material is called Acceptor. The hole (majority carriers) concentration is given by $p = N_A$, where N_A is the acceptor concentration. The electron (minority) concentration is obtained from the expression 1.8 as:

$$n = \frac{n_i^2}{N_A} \tag{1.13}$$

and hence, the Fermi level can be expressed by:

$$E_F - Ev = kT \ln \frac{Nv}{N_A} \tag{1.14}$$

for p-type materials.

The concentration of impurities can be controlled to obtain p-type or n-type material. Figure 1.3 illustrates an example of the range of doping levels in c-Si [39].

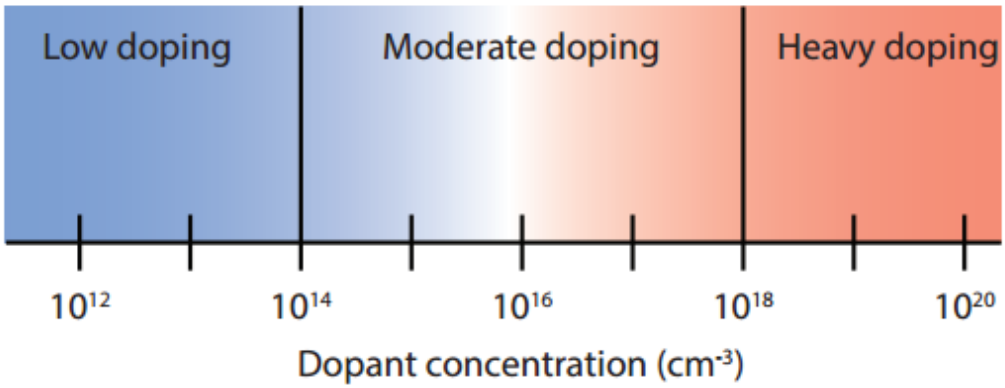

Figure 1.3 – The range of doping levels used in c-Si

1.2.2 Transport properties

Charge transport in semiconductor materials is based on two principal mechanisms namely : drift and diffusion models.

The drift transport principal is based on application of an electric field E on an area of a semiconductor material, which accelerates the electrons in the direction opposite of the electric field and the holes in the direction of the electric field. This movement can be described by average drift velocities v_n and v_p for electrons and holes, respectively, which can be expressed by 1.15 and 1.16 in the case of low electric fields [40].

$$\begin{aligned} v_n &= -\frac{q\tau_c}{m_n} E \\ &= -\mu_n E \end{aligned} \tag{1.15}$$

$$\begin{aligned} v_p &= \frac{q\tau_c}{m_p} E \\ &= \mu_p E \end{aligned} \tag{1.16}$$

Where μ_n is the electron mobility, μ_p is the hole mobility, τ_c is the mean free time and q is the electric charge.

Considering the case of a p-type semiconductor material with a cross-sectional area of A and hole concentration of p as presented in Figure 1.4. Application of an electric field E yields the hole current density J_p expressed by:

$$J_p = -\frac{I_p}{A} = pqv_p = pq\mu_p E \tag{1.17}$$

Where I_p is the hole current. Similarly, the electron current density J_n can be expressed by:

$$J_n = \frac{I_n}{A} = -nqv_n = nq\mu_n E \tag{1.18}$$

Where I_n is the electron current.

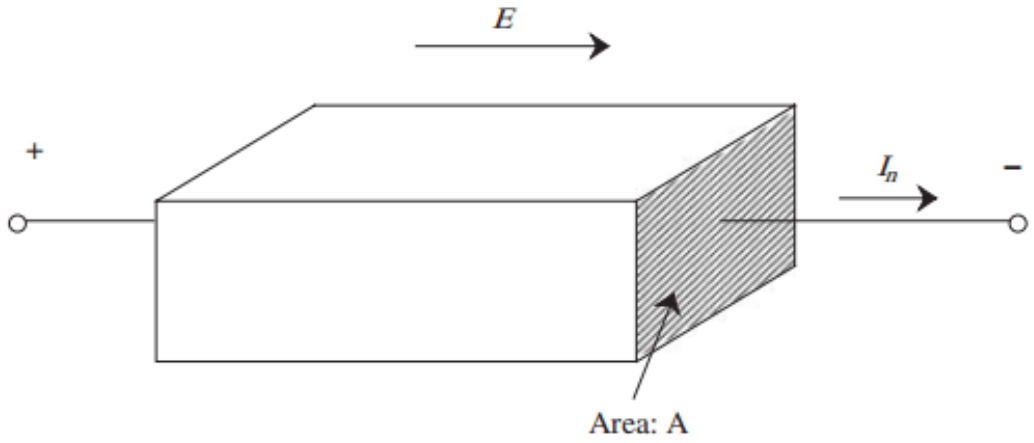

Figure 1.4 – Semiconductor example to consider hole/electron current density

The drift current density J_{drift} is hence obtained by the following expression :

$$J_{drift} = J_n + J_p = \left(nq\mu_n + pq\mu_p\right) E = \sigma E \tag{1.19}$$

Where σ denotes the conductivity.

The diffusion transport principal is based on the movement of charge carriers from the high concentration region to the lower concentration one. The currents obtained is denoted the diffusion currents, which are proportional to the gradient in particle concentration. For electrons and holes, they are given as:

$$J_{ndiff} = qD_n \nabla n \tag{1.20}$$

$$J_{pdiff} = -qD_p \nabla p \tag{1.21}$$

Where J_{ndiff} and J_{pdiff} are the diffusion current density of electrons and holes, respectively. However, D_n and D_p are the diffusion coefficients of electron and hole, respectively. Combining 1.20 and 1.21 leads to the expression of total diffusion current density $J_{diffusion}$:

$$J_{diffusion} = q(D_n \nabla n - D_p \nabla p) \tag{1.22}$$

The parameters D_n and D_p are related to μ_n and μ_p respectively by the Einstein relationship as:

$$\frac{D_n}{\mu_n} = \frac{D_p}{\mu_p} = \frac{kT}{q} \tag{1.23}$$

Combining 1.19 and 1.22 leads to the total current density J expressed as:

$$\begin{aligned} J &= J_{drift} + J_{diffusion} \\ &= q\left(p\mu_p + n\mu_n\right) E + q\left(D_n \nabla n - D_p \nabla p\right) \end{aligned} \tag{1.24}$$

1.3 Basic semiconductor equations

Years of conducted research into device physics have resulted in mathematical model that can be operated on any semiconductor device. This model is the following five equations that link together the electrostatic potential and the carrier densities.

$$div\left(\varepsilon \nabla \psi\right) = -\rho \tag{1.25}$$

$$\frac{\partial n}{\partial t} = \frac{1}{q} div \overrightarrow{J_n} + G_n - R_n \tag{1.26}$$

$$\frac{\partial p}{\partial t} = -\frac{1}{q} div \overrightarrow{J_p} + G_p - R_p \tag{1.27}$$

$$\overrightarrow{J_n} = -q\mu_n n \nabla E_{Fn} \tag{1.28}$$

$$\overrightarrow{J_p} = -q\mu_p p \nabla E_{Fp} \tag{1.29}$$

Where

ψ denotes the electrostatic potential

ϵ is the local permittivity,

ρ is the local space charge density,

G_n and G_p are the generation rates for electrons and holes, respectively.

R_n and R_p are the recombination rates for electrons and holes, respectively

E_{Fn} and E_{Fp} are the quasi-Fermi levels.

The expression 1.25 is the Poisson's equation, the expressions 1.26 and 1.27 are called the carrier continuity equations and the expressions 1.28 and 1.29 are the transport equations [38].

1.4 Optical Absorption and Recombination

The photon energy is $h\nu$, where ν is the light frequency. Photon energy and wavelength λ are linked by the expression given by:

$$\lambda\,(\mu m) = \frac{c}{\nu} = \frac{hc}{h\nu} = \frac{1.2398}{h\nu\,(eV)} \tag{1.30}$$

Where c is the speed of light in vacuum.

To enable electrons from the valence band to move up to the conduction band and hence create a pair electron-hole, it have to be excited by a photon energy bigger than the band gap energy Eg. The energy excess $h\nu - Eg$ is dissipated as heat (see Figure 1.5).

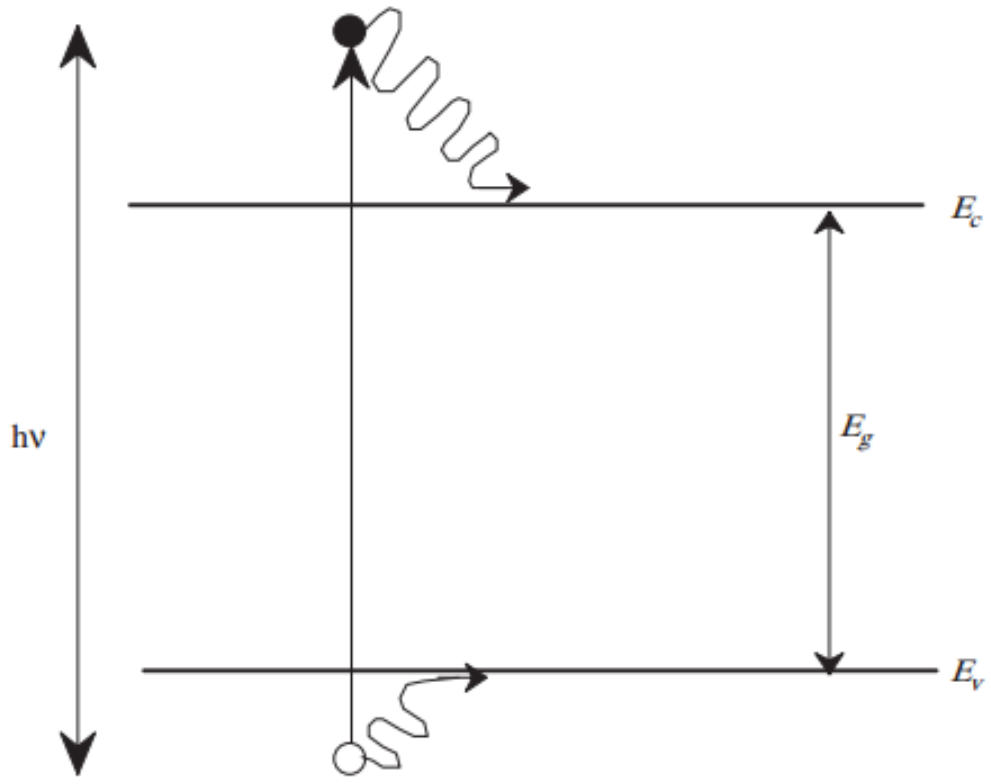

Figure 1.5 – Process of optical absorption

If the photon energy is less than the band gap energy, it is transmitted throw the semiconductor layer and we get a transparent material. Generated charge carriers are available within a short time called lifetime τ and can move for a maximal distance called diffusion length L.

Assuming that a semiconductor surface is exposed to a light with photon flux of F_0 normally in units of photons per unit area per unit time, the number of photons absorbed within a depth of x and $x + \Delta x$ is given by:

$$F(x + \Delta x) - F(x) = -\alpha F(x)\Delta x \tag{1.31}$$

Where α is the absorption coefficient. Taking initial condition $F(0) = (1 - R)F_0$, it gives:

$$F(x) = (1 - R)F_0 e^{-\alpha x} \tag{1.32}$$

Where R is the reflectivity of the surface to normally incident light. The absorption coefficient α is expressed by 1.33 for direct gap semiconductor, and 1.34 for indirect gap semiconductor.

$$\alpha = A^*(h\nu - Eg)^{\frac{1}{2}} \tag{1.33}$$

$$\alpha = \frac{A^{**}\left(h\nu - Eg + E_p\right)^2}{e^{E_p/kT} - 1} + \frac{A^{**}\left(h\nu - Eg - E_p\right)^2}{1 - e^{-E_p/kT}} \tag{1.34}$$

Where A^* and A^{**} are material dependent constants, and E_p is the phonon energy associated at the absorption [40].

After light exposure on semiconductor is stopped, the excess electrons will recombine with holes, until the equilibrium state is reached again. The recombination rate is one of the most responsible processes that determine solar cell performances. It reduces the current gathered in the solar cell. However, the optical generation rate is in general higher than the recombination rate, so the recombination have a negligible effect on solar cell current. It is to notice that the recombination rate is responsible of the saturation current density determination; the more recombination, the higher the saturation current density (which effects the solar cell voltage and hence power conversion efficiency of the solar cell).

Processes responsible for generation recombination in a semiconductor material are known to fall into six main categories namely : phonon transitions, photon transitions, Auger transitions, surface recombination, impact ionization and tunneling [38].

Within the forbidden gap of the semiconductor, phonon transitions appear in the presence of a trap (or defect). This is fundamentally a two-step technique whose theory was obtained first from Shockley and Read [41] and then from Hall [42].

Photon transition is the next physical mechanisms to be regarded for generation/recombination. This mechanism mainly happens in one stage and is therefore a process for direct generation/recombination. It involves two partial procedures. An electron loses energy in the order of the band gap for radiative recombination and moves from the conduction band to the valence band. An electron shifts from the valence band to the conduction band for optical generation.

Auger recombination happens through a transition of three particles by capturing or emitting a mobile carrier. The basic physics for such procedures is uncertain and usually a more qualitative knowledge [43] is adequate.

In addition to generation/recombination, electrons or holes can be recombined or generated at interfaces within the bulk of the semiconductor. The recombination rate of the surface may be even higher than in the bulk [44].

The impact ionization model assumed that the electrical field will be high enough in any space charge region with a sufficiently high reverse bias to accelerate free carriers to a point where they will have sufficient energy to generate more free carriers when they collide with the crystal atoms. Two basic requirements must be met in order to obtain adequate energy. First of all, the electrical field must be high enough. Then, the distance between the free carrier's collisions must be sufficient to allow acceleration to a sufficiently elevated velocity. In other terms, the carrier must achieve the Eibetween collisions of ionization energy. If the rate of generation of these free carriers is big enough, this method will eventually result in a breakdown of the avalanche.

The tunneling principal is based on the knowledge that when there is a sufficiently elevated electrical field within a local band bending device, it can be adequate to allow electrons to tunnel from the valence band into the conduction band through internal field emission. Therefore, in the conduction band, an extra electron is produced and so a hole in the valence band. This generation mechanism is applied into the right side of the continuity equations [45–47].

1.5 PN junction

The commonly used realization in solar cell technology is the well-known PN junction consisting of adjacent p-doped and n-doped areas as shown in Figure 1.6.

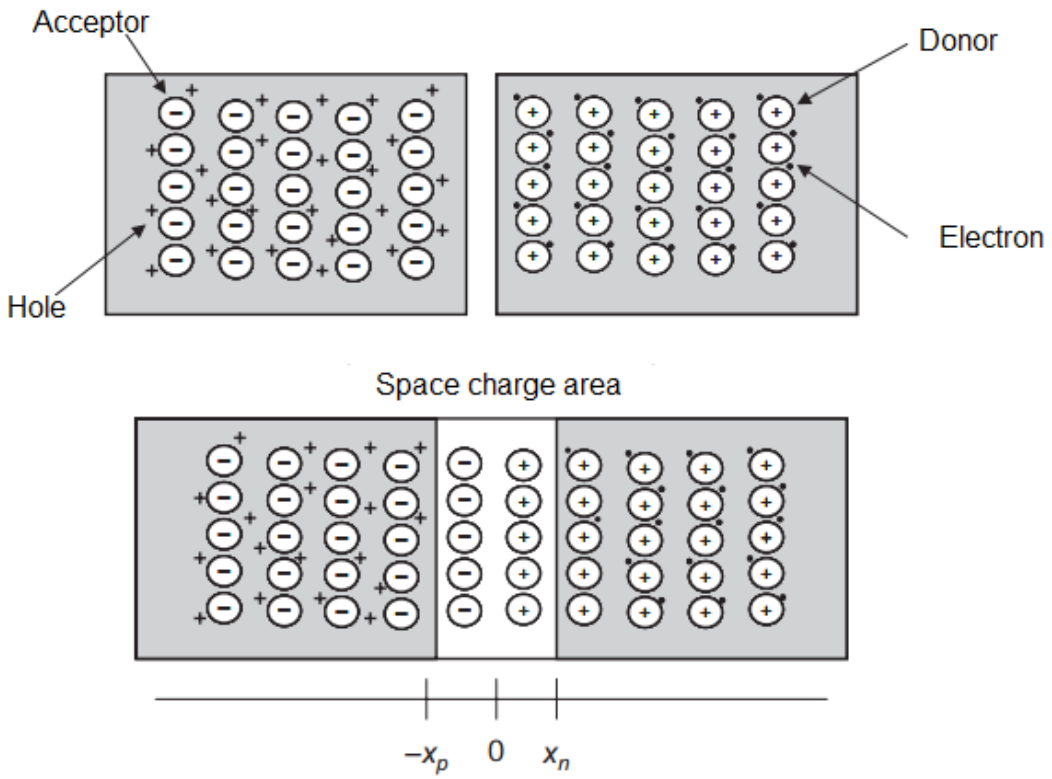

Figure 1.6 – Typical PN junction.

The levels of doping in the darkness are N_D and N_A. The electron (hole) density in the n (p) area in the thermal equilibrium is $n = N_D$ ($p = N_A$). The Fermi levels are close to the conduction band for the n-doped semiconductor and close to the valence band for the p-doped semiconductor, according to equations 1.4 and 1.7. Once the two areas are linked together, we have a steady electrochemical potential in equilibrium and therefore an alignment of E_F. Electrons and holes concentration gradients between p-and n-region cause electrons to diffuse to p-doped and holes to the n-doped crystal where they recombine. Because the entire semiconductor is neutral, immobile ionized doping atoms stay. They create a region of space-charge ρ that produces a field according to the equation of Poisson. This field opposes the current of diffusion and holds it in equilibrium, which is represented by a constant E_F. The potential difference is labeled the built-in potential V_b and reflects the distance between the Fermi levels of the neutral n-doped and p-doped areas, which can be specified by the concentrations of the equilibrium charge carrier n_n^0 (electron concentration in the n-doped region in thermal equilibrium) and p_p^0 (hole concentration in the p-doped region in thermal equilibrium) according to equations 1.4 and 1.7 by the expression given as:

$$V_b = \frac{kT}{q} \ln \frac{N_A N_D}{n_i^2} \tag{1.35}$$

Electron-hole pairs are produced under illumination when photon energy exceeds the band gap. The amount of pairs of electron–hole is proportional to the intensity of light. The drift of electrons to the n-side and that of holes to the p-side occurs in the depletion area due to the electrical field generated by the ionized impurity particles. When an external wire is short-circuited as shown in Figure 1.7, this charge separation outcomes in the current stream from n-to p-side. The electron – hole pairs produced from the edge of the depletion area within a distance of diffusion length contribute to the photocurrent due to the diffusion of surplus carriers up to the area of space charge.

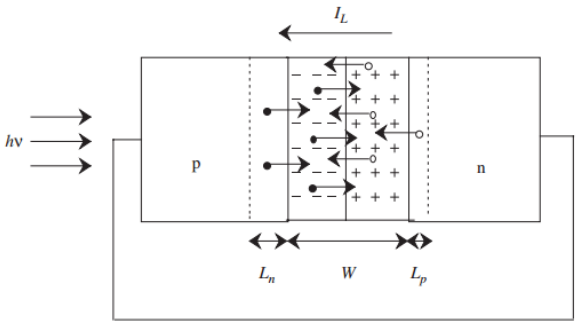

Figure 1.7 – Schematic illustration of carrier flow under illuminated p–n junction in the case of short-circuited.

When the illuminated PN junction is open-circuited, the voltage is produced as a result of the separation of the charge carrier. Figures 1.8a and 1.8b show the energy band diagrams of the PN junction in the short-circuited and open-circuited current, respectively.

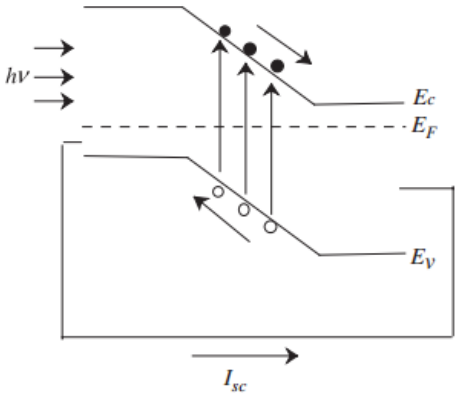

(a) The short-circuited current

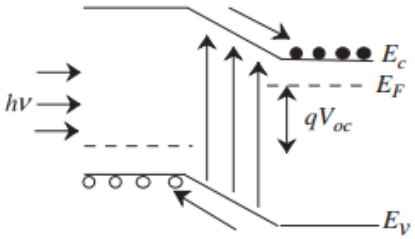

(b) The open-circuited current

Figure 1.8 – Energy band diagrams of illuminated p–n junction.

When the p-and n-side are short-circuited, if the series resistance is zero, the current is called the short-circuit current Isc and is equal to the photogenerated current I_L. When the p-and n-side are isolated, electrons migrate in the direction of n-side and holes in the direction of p-side, creating the potential generation. Developed voltage is called the Voc open-circuit voltage. Figure 1.12 shows the current-voltage features of the p–n junction under illumination and darkness.

1.6 Equivalent circuit

Figure 1.9 presents the equivalent circuit of an illuminated PN junction solar cell which is similar to an ideal diode. The equation 1.36 describes the PN junction relation between J and V.

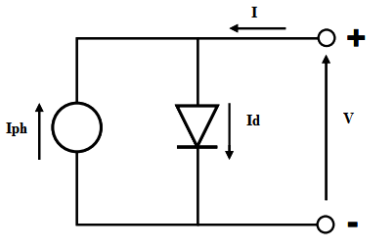

Figure 1.9 – Ideal solar cell equivalent circuit under illumination.

$$J = J_0 \left[exp\left(\frac{qV}{kT}\right) - 1 \right] - J_{ph} \tag{1.36}$$

Where Voc is the open circuit voltage, Jsc is the short circuit density of current, J_{ph} represents the photo-generated density of current and J_0 is the saturation current density.

The dark diode current density is presented by the first term in equation 1.36. However, the second term presented the photo-generated current density [48].

In practice, J is influenced by a series resistance R_s, and a shunt resistance R_{sh} of the solar cell which make the equivalent circuit similar to the Figure 1.10.

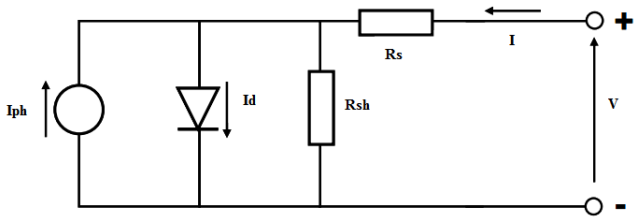

Figure 1.10 – Real solar cell equivalent circuit under illumination.

The equation 1.37 presents the relation between J and V in case of real solar cell:

$$J = J_0 \left[exp\left(\frac{q\,(V - AJR_s)}{kT} \right) - 1 \right] + \frac{V - AJR_s}{R_{sh}} - J_{ph} \tag{1.37}$$

Where A is the area of the solar cell.

The effect of both R_s and R_{sh} on J-V characteristics is presented in Figure 1.11.

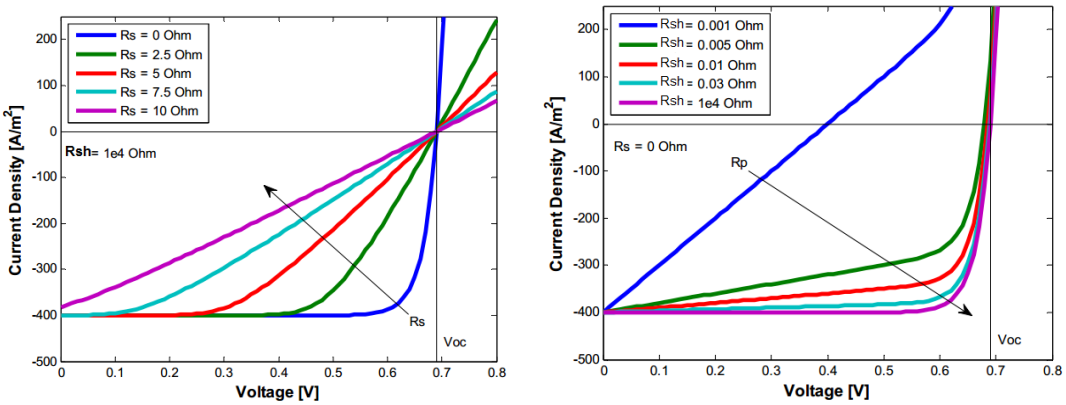

(a) Series resistance effect

(b) Shunt resistance effect

Figure 1.11 – Effect of series and shunt resistance on J-V characteristics.

1.7 Electrical parameters of a solar cell

A PN junction solar cell has four principal parameters namely : Voc, Jsc, FF and η (PCE) (see Figure 1.12). To derive analytical expressions of the output parameters, the simple p–n structure with the homogeneously doped abrupt junction, as shown in Figure 1.7, is considered for the case of the low-injection level. It consists of a p-type emitter layer on the n-type base layer.

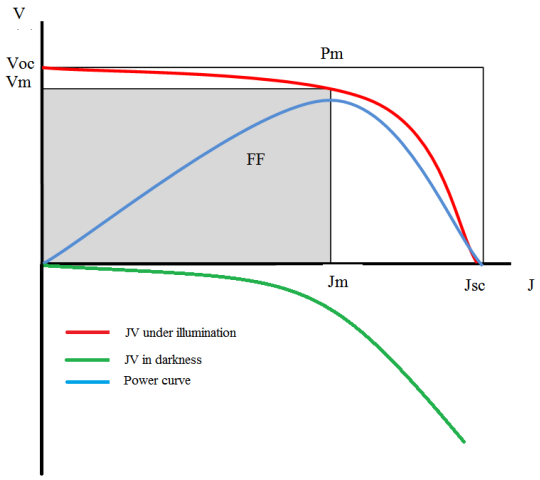

Figure 1.12 – Electrical parameters of a p–n junction.

1.7.1 Short circuit current

When the electrodes of a solar cell are short circuited, the current that flows through the external circuit is called the short circuit current Isc. It depends on the photon flux density incident on the solar cell, that is determined by the spectrum of the incident light. For the standard solar cell measurements, the spectrum is standardized to the AM1.5 spectrum. In order to remove Isc dependence on area of a solar cell, the short-circuit current density Jsc is often used to describe the maximum current delivered by a solar cell.

1.7.2 Open circuit voltage

In the case of no charge between solar cell electrodes, the Voc is the voltage in which no current flows through the external circuit. The Voc is the maximum voltage that a solar cell can deliver. For a real PN junction solar cell, open-circuit voltage is provided by:

$$Voc = \frac{nkT}{q} \ln\left(\frac{Jsc}{J_0} + 1\right) \tag{1.38}$$

It is obvious that the saturation current density should be low and that the current density of the short circuit should be big in order to obtain a big open-circuit voltage.

1.7.3 Fill Factor

The fill factor is the ratio between the maximum power $P_m = J_m \times V_m$ generated by a solar cell and the product of Voc and Jsc (equation 1.39).

Figure 1.12 presents the fill factor FF of the solar cell when it is operated under a conditions that give the maximum output power, the voltage V_m and the current I_m at the optimum operating point. The following expression defines the formula of the FF :

$$FF = \frac{V_m I_m}{VocIsc} \tag{1.39}$$

1.7.4 Power Conversion Efficiency

The solar cell's Power Conversion Efficiency (PCE) η is defined as the ratio of the maximum electrical output power generated to the total incident light power P_{in} as expressed by:

$$\eta = \frac{V_m I_m}{P_{in}} = \frac{VocIscFF}{P_{in}} \tag{1.40}$$

The photovoltaic parameters are assessed under conventional test circumstances: the air mass AM1.5 spectrum with an incident power density of $1000W/m^2$and a temperature of $25°C$. To enhance efficiency, all three photovoltaic parameters Voc, Isc and FF need to be maximized.

1.8 Conclusion

Actually, most used solar cells in the industry are based on semiconductor materials that exhibit special behavior suitable for light energy conversion to electrical form. A typical solar cell can be modeled as a PN junction where light energy is absorbed by the active layer and generate a pairs of free electron-hole that moves under the drift and diffusion mechanism to generate electrical current. In this chapter, various basic theoretical knowledge in the physics of semiconductors which is the origin of solar cell technology was presented. Therefore, the PN junction which is the principal element that describes the solar cell behavior is discussed in order to highlight its principal properties under different conditions. Then, Mechanism of drift and diffusion is discussed in order to understand the way of electron-hole pairs current generation. Also, equivalent electrical circuit of a solar cell based on a PN junction was presented in both ideal and real models to clarify diverse electrical parameters.

CHAPTER 2

PEROVSKITE MATERIALS AND THEIR IMPLEMENTATION IN SOLAR CELLS

2.1 Introduction

Solar cell technologies are composed into four generations regarding to their development stages as presented in Figure 2.1 [49].

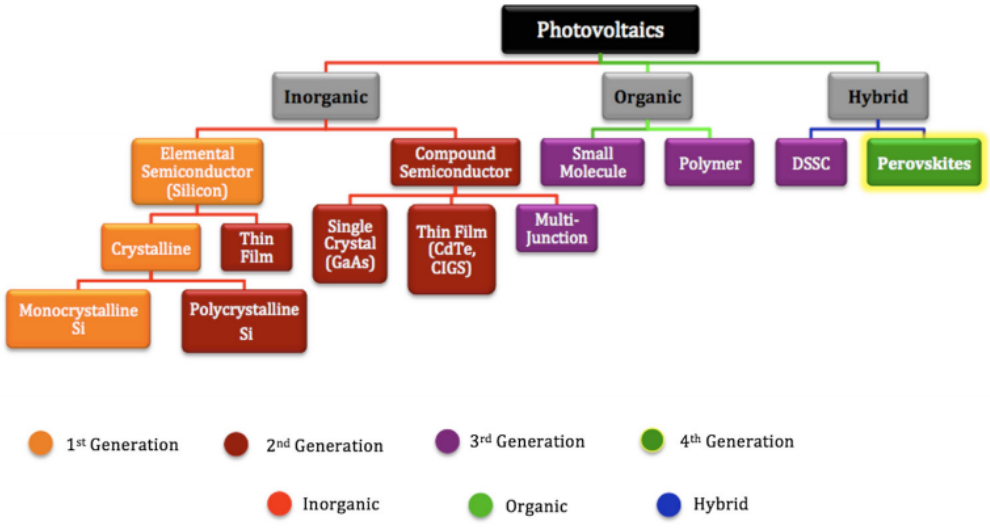

Figure 2.1 – Classification of photovoltaic technologies [49].

The perovskite based solar cells (PSC) belongs to the fourth generation technology which is characterized by high power efficiency and low processing costs. In the present chapter we will discuss a brief history of PSC evolution in the last decade, then an overview of perovskite structure, different kinds and characteristics of perovskites. Principal perovskite materials will be discussed. The last part of this chapter is focused on operation of PSC.

2.2 History

In 1839, the Russian mineralogist Gustav Rose have discovered the mineral calcium titanate ($CaTiO_3$) in calc-silicate contact metamorphic rocks (Figure 2.2) in the Ural Mountains of Russia [50] and he called it "Perovskite" in honor of Russian mineralogist, Count Lev Alexevich von Perovski. The first application of the perovskite materials (PVK) in photovoltaics was acheived by the Tokyo-based group of Tsutomu Miyasaka [51] where they recorded a power conversion efficiency of 2.2% in 2006 and later 3.8% in 2009 [19]. The power conversion efficiency of PSC increased then up to 6.5% in 2011 [9], up to 20.1% in 2015 [52], up to 22.1% in 2016 [20] and then up to 25.2 % in 2019 [21, 22]. The Figure 2.3 represents the development of PCE of different photovoltaic devices [21].

Figure 2.2 – Perovskite mineral [50].

From the NREL 2019 chart (Figure 2.3), it is to notice that perovskite technology has a PCE of an exponential rise in a decade, which proof its importance.

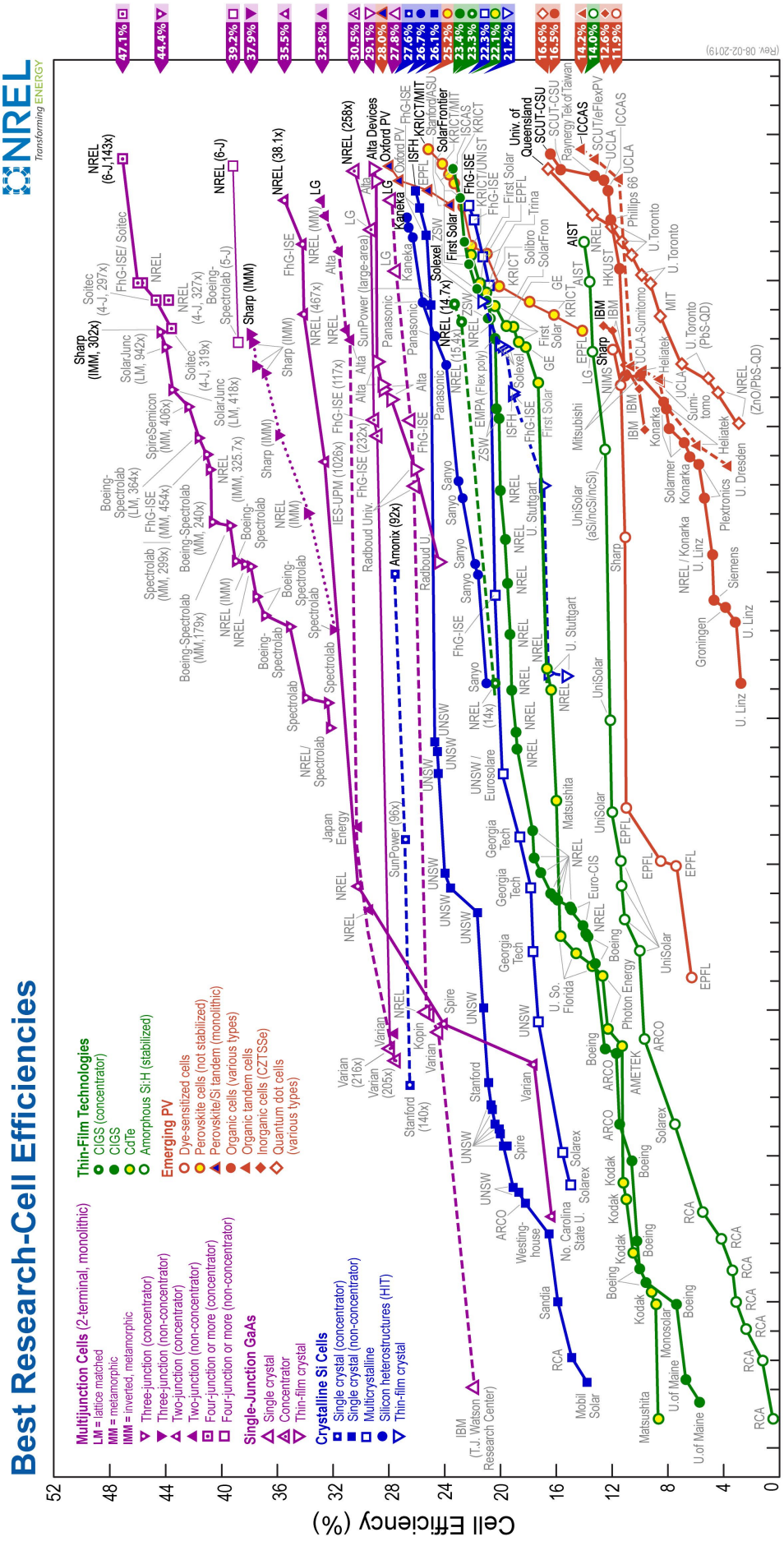

Figure 2.3 – Efficiency evolution of perovskite solar cells until 2019 [21].

2.3 Perovskite crystalline structure

The general crystalline molecular structure of perovskite materials ABX_3, where A and B are cations and X an anion, is presented in Figure 2.4. Whereas, it is shown that a typical unit cell structure of a fundamental perovskite molecule is constituted by the A cation situated in vertex of the face-centred cubic lattice, the B cation and the X anion who occupy the core and apex of the octahedra, respectively [53].

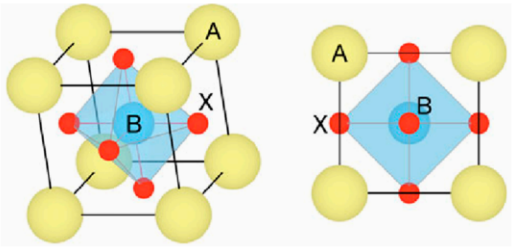

Figure 2.4 – Molecular structure of ABX_3 perovskite [53].

The A cation belongs to group organic or inorganic material of (methyl ammonium $CH_3NH_3^+$, ethyl ammonium $CH_3CH_2NH_3^+$, formamidinium $HC(NH_2)_2^+$, Cs^+, Rb^+), the B metal cation can be from (Ge^{2+}, Sn^{2+}, Pb^{2+}) and the X anion can be one of material group (O^{2-}, F^-, Cl^-, Br^-, I^-, and S^{2-}) [49, 54]. Combination of different A, B, and X elements yields hundreds of perovskite materials [53, 55–58].

2.4 Types of perovskite

According to A cation perovskites can be divided into two classes : inorganic perovskites and hybrid (organic/inorganic) perovskites. However, perovskite materials can be considered as halide and non-halide class according to the X anion [56]. Halide perovskites have a halogen material in the X anion, and have the advantage of high power conversion efficiency, whereas, non-halide perovskites are less toxic and more stable [56]. However, Hybrid perovskites can be classified regarding to environmental point of view as : toxic and non-toxic (environmentally friendly).

It is to notice that B and X may be simple or mixed materials (such as $B = Sn_{1-x}Pb_x$ or $X = I_{3-x}Br_x$) [53].

In this thesis, our work is focused on hybrid halide perovskites where the cation A is the methyl ammonium $CH_3NH_3^+$, the B cation group is (Ge^{2+}, Sn^{2+}, Pb^{2+})) and the anion X is a halogen from the group (Cl^-, Br^-, I^-), because of its suitability to photovoltaic applications [49]. In the rest of this thesis studied perovskite is denoted MABX3 (MA for methyl ammonium).

The most common PVK materials used in photovoltaics are Methyl ammonium lead tri-iodide ($\mathbf{MAPbI_3}$), Methyl ammonium lead tri-bromide ($\mathbf{MAPbBr_3}$), mixed Methyl ammonium lead iodide-chloride ($\mathbf{MAPbI_{3-x}Cl_x}$) and mixed Methyl ammonium lead iodide-bromide ($\mathbf{MAPbI_{3-x}Br_x}$) [59, 60].

2.5 Characteristics of Perovskites

Perovskites have the advantage of good optical and electrical characteristics more adapted to photovoltaics comparing with conventional silicon. Principal Perovskite characteristics are, but not limited to

- Good optical properties and a high absorption coefficient [61];
- Ability to absorb solar energy efficiently [62];
- Large dielectric constant providing charge carrier easy movement [63];
- pair electron/hole can be transmitted in the same time because of the good diffusion length that reaches even more than $1\mu m$ [64–67];
- low recombination losses [59];
- low material costs [59];
- possibility of anion/cation substitution for bandgap tuning [59];
- needs advanced control of the morphology of the film and properties of the material [59];
- the use of toxic substance like lead [59];
- cell instability [59];
- high proneness to moisture [59].
- material degradation and hysteresis [68]

2.6 Overview on some Perovskites

In the next sections will be studied the advantages and disadvantages of most suitable $MABX_3$ perovskites for solar cell technology.

$MAPbI_3$

The methyl ammonium lead halide is the toxic element of hybrid perovskites category because of the lead substitution in cation B situation. However, it presents the better light absorption coefficient making it the best candidate for perovskite solar cell applications. In the visible light range, its effective absorption coefficient is around $1.0 \times 10^{-5}(mol.L^{-1})^{-1}cm^{-1}$ at a thickness of $550nm$ which enable it to absorb the full light in film. $MAPbI_3$ diffusion lengths are $L_n = 130nm$ and $L_p = 100nm$ for electrons and holes respectively [69,70]. It has a good electrical transport properties and favorable bandgap (arround 1.55 eV) which is close to the optimum value for a single junction solar cell [71].

$MAPbBr_3$

The Br substitution in halide anion position yields a high band gap energy of 2.3 eV, less optical absorption in the infrared region and higher *Voc* (1.16 V [72], 1.3 V [73]) compared to $MAPbI_3$ [71]. Quality of deposited bromide films is good according to [74] XRD measurements which reported no remnants of CH_3NH_3Br and $PbBr_2$ in the synthesized $MAPbBr_3$ which is indicating that all of the $PbBr_2$ is converted into $MAPbBr_3$ and the CH_3NH_3 has been completely used up [75].

$MAPbCl_3$

This chloride based n-type perovskite has a large band gap that reaches 3.09 eV [76] and is the most stable comparing with $MAPbI_3$ and $MAPbBr_3$ [77]. The **$MAPbCl_3$** is more suitable for light-emitting devices [78].

$MAPbI_{3-x}Cl_x$

The X anion in this perovskite is a mixed material. Its absorption coefficient is similar to the $MAPbI_3$. Whereas, the $MAPbI_{3-x}Cl_x$ diffusion length is higher with $L_n = 1100nm$ and $L_p = 1200nm$ [69,70]. Properties of this perovskite can be tuned with I and Cl fractions. This leads to changes in the energy band gap (Figure 2.5) as well as the optical absorption band width. However, it has a

high electron-hole diffusion length ranging from $100nm$ to $1\mu m$ [71]. In [79], Snaith and and co-workers denoted that $MAPbI_{3-x}Cl_x$ exhibited better stability and carrier transport compared to its pure iodide equivalent. Figure 2.5 presents energy band gap of $MAPbI_{3-x}Cl_x$ in function of Cl composition.

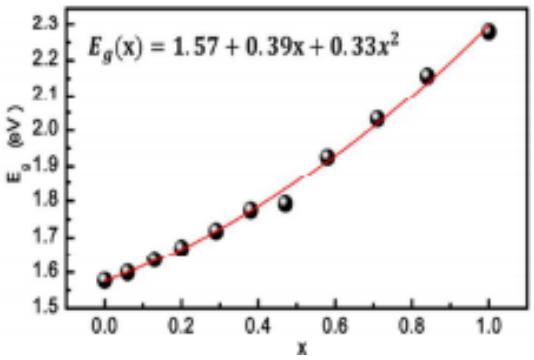

Figure 2.5 – Variation of Eg in function of Cl composition in $MAPbI_{3-x}Cl_x$ [72].

The energy levels and absorbance of some halide perovskites is reported in Figure 2.6.

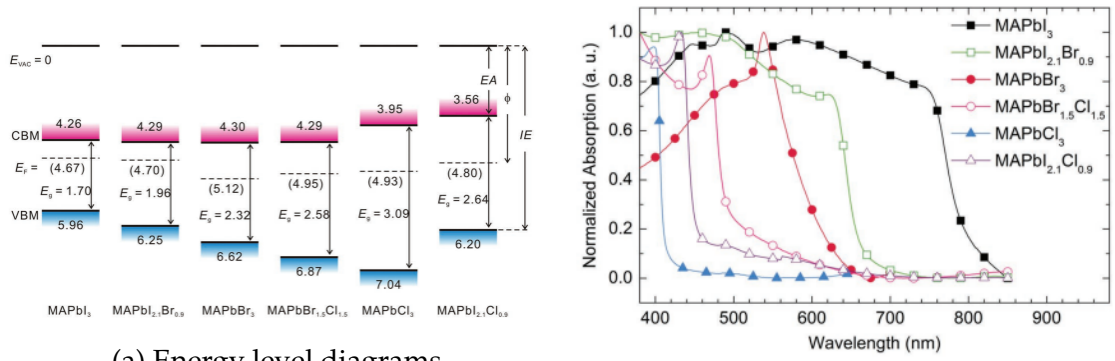

(a) Energy level diagrams.

(b) absorption spectra.

Figure 2.6 – Energy level and absorption spectra for some halide perovskite [80].

$MASnI_3$

The **$MASnI_3$** is a good candidate for lead free perovskite. The relativistic GW (Green's function and Wick's theorem of density functional theory) calculations on the electronic and optical properties predict $MASnI_3$ to be a better electron transporter than $MAPbI_3$ [49, 81]. $MASnI_3$ exhibited a band gap of 1.3 eV that permit it to cover a wide range of light spectrum [82]. The major limitation when using $MASnI_3$ perovskites is oxidation of Sn from Sn^{2+} to Sn^{4+} in air, which limits device performance [82].

$MAGeI_3$

Germanium based perovskite is another lead free material. $\mathbf{MAGeI_3}$ was synthesized with a wide band gap of 1.9 eV [83]. However, this material exhibited a major disadvantage of instability because of the high oxidation tendency of Ge^{2+} and emergence of deep defect states [83–85]

2.7 perovskite based solar cells operation

perovskite based solar cells are usually fabricated by a perovskite absorbing layer sandwiched between an electron transporting layer (ETL) and a hole transporting layer (HTL) according to an n-i-p or p-i-n structure (see Figure 2.7). The charge generation process of the perovskite absorbing layer responsible on light harvesting is not well understood because of the complex nature of the medium [71]. The charge transport dynamics in PSC suppose that the electron-hole pairs are generated directly after photo-excitations in perovskite material and then dissociated into free charge carriers where electrons diffuse into the ETL and the holes into the HTL in less than 2 ps [74,79,86] under the effect of built-in electric field generated by the difference of workfunction between the cathode and the anode.

PSC can be classified into four structures as shown in Figure 2.7:

1. n-i-p planar heterojunction
2. p-i-n inverted planar heterojunction
3. n-i-p mesoscopic heterojunction
4. p-i-n mesoscopic heterojunction

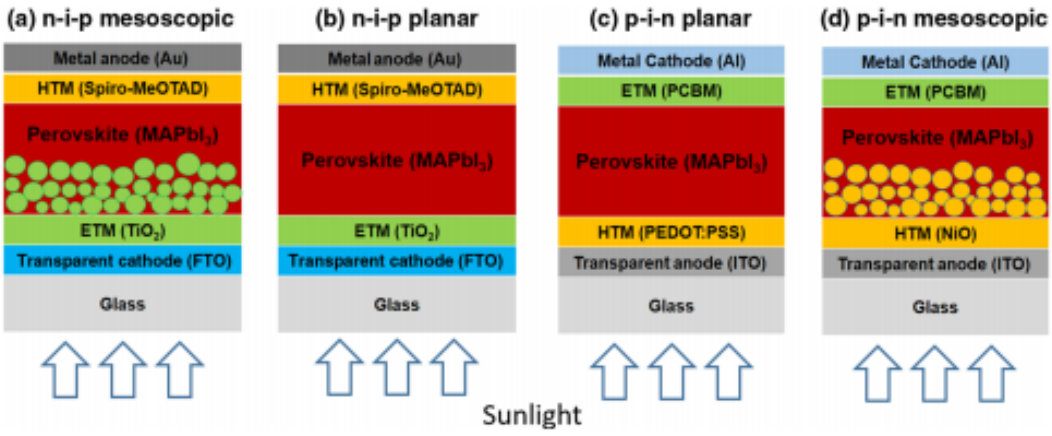

Figure 2.7 – Different PSC structures [87].

In this thesis, we investigated both n-i-p and p-i-n planar heterojunction-based PSC. This choice is made because of previous research efforts that confirmed the superiority of planar structures in term of charge carrier mobility that reached over $20cm^2V^{-1}s^{-1}$ than mesoporous ones [88–91].

2.7.1 n-i-p planar heterojunction-based PSC

Figure 2.8 illustrates a sample PSC structure based on n-i-p planar heterojunction, where it can be noticed that this structure have the folowing characteristics :

1. the HTL used is the 2,2′,7,7′-tetrakis(N,N-di-p-methoxyphenylamine)-9,9′-spirobifluorene (spiro-OMeTAD),
2. the front layer is the ETL,
3. the used ETL can be : TiO_2, $c-TiO_2$, ZnO, Ta_2O_5, Al_2O_3, ZrO_2, SnO_2,
4. the PVK material can be based on Pb^{+2}, Sn^{+2}, or Ge^{+2}.

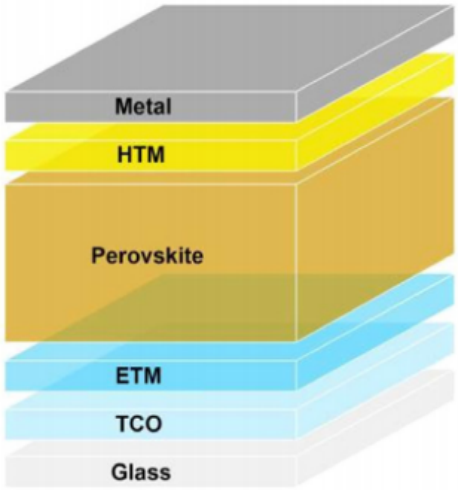

Figure 2.8 – n-i-p planar heterojunction-based PSC design.

The n-i-p planar architecture of PSC is an evolution of the mesoscopic structure, because the absence of mesoporous metal oxide layer leads to an overall simpler structure [78]. Without mesoporous layer, PSC can achieve high efficiency by a judicious control of different layers that constitute the cell (PVK, ETL, HTL as well as electrodes) [92]. Therfore, with the same materials and approach, a planar n-i-p PSC shows increased Voc and *Jsc* relative to a mesoscopic PSC device; however, the planar configuration also had more severe J-V hysteresis which calls into question the accuracy of the reported efficiencies [87].

2.7.2 p-i-n planar heterojunction-based PSC

Figure 2.9 shows a sample structure of PSC based on n-i-p planar heterojunction, where it can be noticed that this structure have the folowing characteristics :

1. the HTL used is the poly(3,4-ethylenedioxythiophene) poly(styrene-sulfonate) (PEDOT:PSS),
2. the front layer is the HTL,
3. the used ETL can be the C_{60} or its derivatives such as C_{61}, [6,6]-phenyl C_{61}-butyric acid methyl ester ($PC_{61}BM$), [6,6]-phenyl C_{71}-butyric acid methyl ester ($PC_{71}BM$), 1',1'',4',4''- Tetrahydro-di[1,4] methanonaphthaleno [1,2:2', 3', 56,60:2'',3'']][5,6]fullerene-C_{60} (ICBA).
4. the PVK material can be based on Pb^{+2}, Sn^{+2}, or Ge^{+2}.

In p-i-n structure, HTL is deposited first followed by PVK layer then ETL. Jeng et al. have deposited the first p-i-n PSC with PCE of 3.9% [93]. Later in 2017, Hu et al. developed a high efficiency p-i-n PSC achieving a PCE of 18.2% [94]. Actually, p-i-n planar structure recorded the highest PCE, offers low-temperature processing and negligible hysteresis behavior [78]. Kim et al. also observed that J-V hysteresis problem is significantly reduced comparing by the n-i-p structure because of use of the PEDOT:PSS or any other inorganic hole-transporting materials [95].

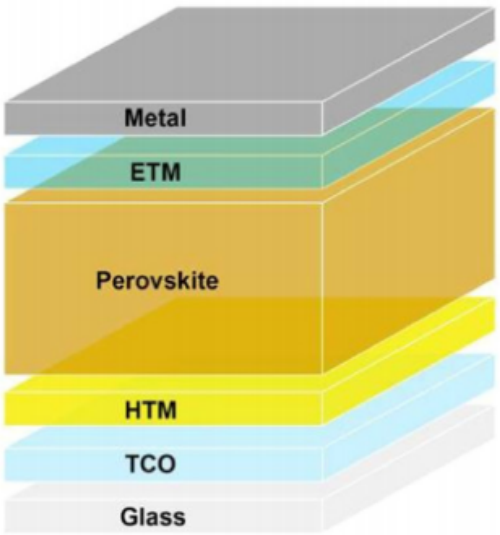

Figure 2.9 – p-i-n planar heterojunction-based PSC design.

2.7.3 ETL materials used in PSC

In PSC, ETL belongs to two principal categories : organic and inorganic materials. In regular structure (n-i-p) the most used ETL is the inorganic one, whilst in the inverted structure (p-i-n) the most used is the organic type [78]. An ideal ETL material is supposed to have two principal characteristics : an energy level compatible with that of perovskite to enhance injection of photo-generated electrons and hence reducing energy losses; and innately high electron mobility to boost fast electron transportation [96]. Consequently, ETL material acts as selective layer for electron transportation to the anode.

Figure 2.10 shows energy levels for some inorganic ETL materials. Actually, the most suitable ETL for n-i-p structure is the titanium dioxide (TiO_2) because it has excellent electron-transporting properties. Regarding to high temperature processing of TiO_2 that reaches more than $500°C$, it is not suitable neither for temperature sensitive materials nor for low cost PSC [97]. For the last reasons, researchers developed low temperature processing for TiO_2 fabrication based on several ways such as sol-gel method [98], chemical path deposition method [99] and solution-processed [100].

In comparison with TiO_2, oxide of zinc (ZnO) shows higher electron mobility (bulk mobility, $205 - 300 cm^2 V^{-1} s^{-1}$) and can be easily deposited via a low-temperature process which requires no heating or sintering [101], which makes it a good candidate for TiO_2 replacement. However, ZnO presents a chemical instability, so it is not suitable for long term commercialization [78].

Lately, SnO_2 is to be another candidate for ETL material substitution because of its wide bandgap, high transparency, high electron mobility, excellent optical and electrical properties and low temperature processing [78].

Indium oxide (In_2O_3) is also a promising ETL material which have excellent optical and electrical properties including a wide band gap, high electron mobility, and good light-transmitting properties. Based on these advantages, Fang et al. [98] employed a low-temperature solution-processed In_2O_3 nanocrystalline film as an ETL in PSCs for the first time and achieved an efficiency exceeding 13%.

Furthermore, WOx is a possible potential ETL material for its good chemical stability, wide band gap, and high electron mobility. Wang et al. [102] applied WOX as an electron selective layer in PSCs through a simple, low-temperature solution process which exhibited comparable light transmittance and photoelectric conversion efficiency to TiO_2, but with higher electric conductivity as well as short-circuit current density; however, they obtained a lower open-circuit voltage.

Because of some excellent properties such as wide band gap and high thermal and chemical stability, CeO_x is also being considered as a promising material for ETLs. Though CeO_x has already been used in different solar cells for its outstanding properties, Wang et al. reported using CeO_x as an ETL material in PSCs for the first time in 2017. They demonstrated that solution-processed CeOx (x = 1.87) based PSCs could be prepared via a facile, simple sol-gel method at a low temperature (150°C), as a possible alternative to high-temperature sintering-processed TiO_2-based PSCs. The CeO_x-based planar PSCs achieved a PCE as high as 14.32% with good stability [103].

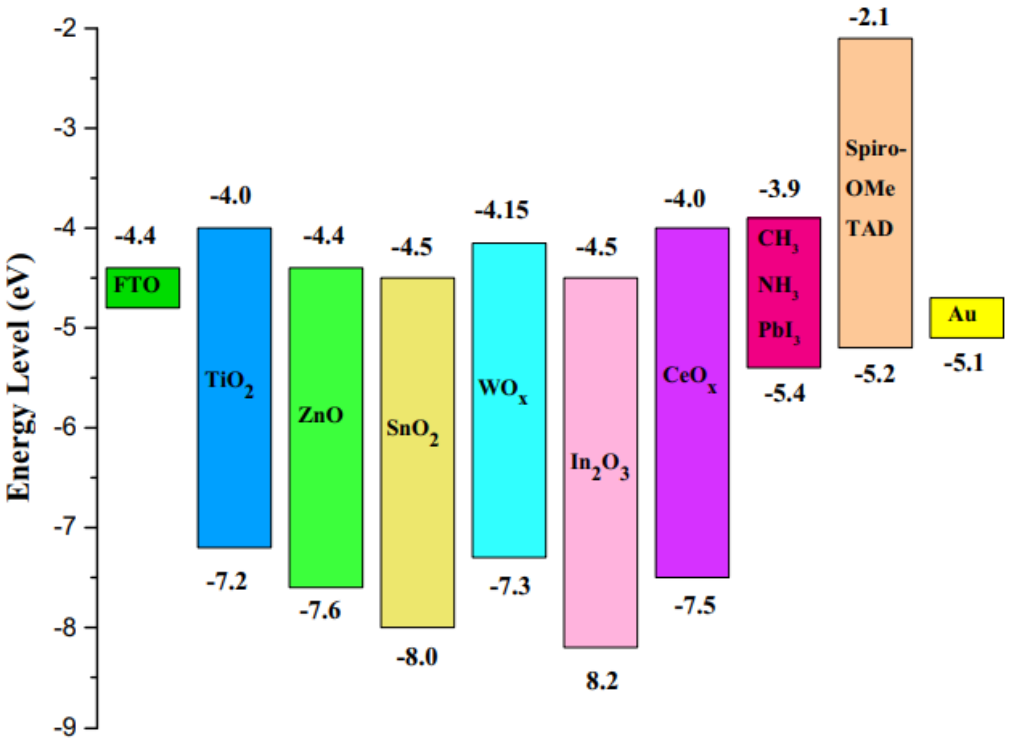

Figure 2.10 – Energy level for different inorganic ETL materials.

Figure 2.11 demonstrates energy levels for some organic ETL materials.

Organic ETL materials such as fullerenes (C_{60}) and their derivatives (including [6,6]-phenyl-C61-butyric acid methyl ester ($PC_{61}BM$), indene C60 bis-adduct (ICBA), and [6,6]-phenyl-C71-butyric acid methyl ester ($PC_{71}BM$)) have seen very widespread use as ETLS in p-i-n structure PSC due to their good bandgap alignment, sufficient electron mobility, and amenability to a low-temperature solution-based deposition process. PCBM has high electrical conductivity and has been the most commonly used as ETL material of the fullerene derivatives. It has been shown to efficiently quench the photoluminescence of MAPbI3, lending it a high probability of efficient charge transfer [104]. Jeng et al. tested different fullerene derivatives as ETMs in inverted planar PSCs and found that devices with $PC_{61}BM$ outperformed those prepared with C_{60} and ICBA [93]. The lowest unoccupied molecular orbital (LUMO) energy level of C_{60} compared to $PC_{61}BM$ (4.5 eV vs. 3.9 eV) explains the *Voc* drop in PSC devices prepared with C_{60}, whereas cells prepared with ICBA (which has a higher LUMO energy level than $PC_{61}BM$) yield a higher Voc [93]. Wang et al. also observed similar results regarding the photovoltage in planar PSC devices [105]. Other than the fullerene derivatives, there are other organic materials that have been evaluated as ETLs in inverted PSC architectures. For example, Malinkiewicz et al. demonstrated that organoborane compounds like 3TPYMB could be suitable as an ETL material for inverted PSCs [104]. They found that 3TPYMB-based PSCs achieved a PCE of 5.5% which compares somewhat favorably with expensive PCBM-based devices which exhibited 10% PCE [104].

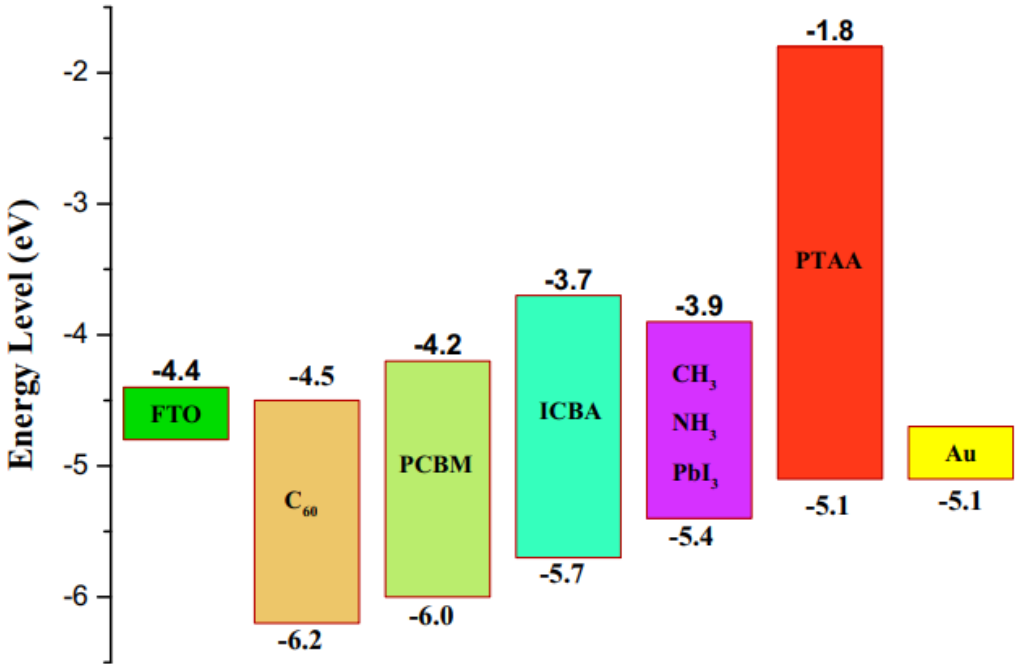

Figure 2.11 – Energy level for different organic ETL materials.

2.7.4 HTL materials used in PSC

The HTL material is responsible of hole extraction and transportation to the cathode. An ideal HTL material should have some basic characteristics, including a well-matched highest occupied molecular orbit (HOMO) energy level relative to the perovskite layer for efficient interfacial hole transfer, good internal hole mobility, and good thermal and photochemical stability [29]. HTL materials can be classed into three types namely : small molecules, polymeric and inorganic. Figure 2.12 presents a summary of most HTL materials used in PSC.

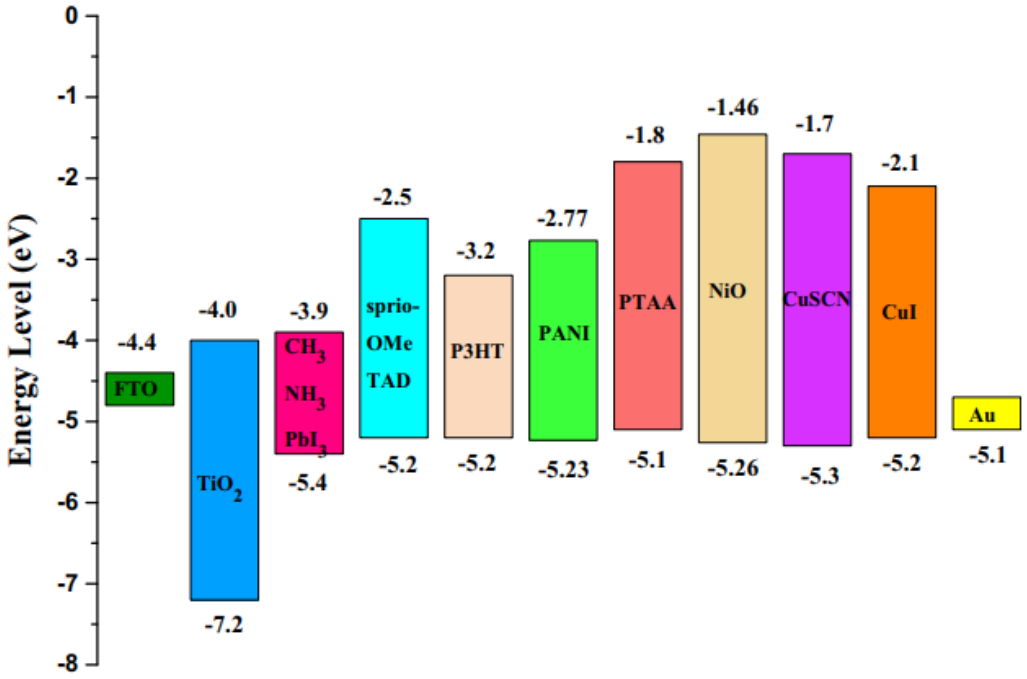

Figure 2.12 – Energy level for HTL materials [78].

Small molecules HTL materials have the advantage of the relatively simple processing and extensive modifiability [78].The most common small molecule used in n-i-p structure is the famous spiro-OMeTAD which has some encouraging advantages namely : efficient hole transportation, small series resistance and small interfacial losses, thereby aid to enhance *FF* and Voc [92]. However, this material is high cost processing which is the main disadvantage, it is 10 times more expensive than gold [106]. Furthermore, the addition of ionic additives such as bis(trifluoromethane)sulfonimide lithium salt (Li-TFSI) and 4-tert-butyl pyridine (TBP) and co-dopants are required to improve the innate conductivity and hole mobility of Spiro-OMeTAD [107], which further increases the fabrication cost of Spiro-OMeTAD-containing PSCs.

Concerning the polymeric HTL materials such as polyaniline (PANI), poly (triarylamine) (PTAA), and poly(3-hexylthiophene-2,5-diyl) (P3HT) they offer higher hole mobility than the small-molecule HTL materials and, also typically, have excellent film-forming properties due to their polymeric nature [29]. Heo et al. reported that PTAA yielded a significantly higher PCE (12%) compared to P3HT (6.7%) [108]. Although at the early stages P3HT-based PSCs exhibited lower efficiencies due to the high rates of charge recombination compared to other HTMs (like Spiro-OMeTAD) [109], recently, P3HT HTM-based PSC devices have shown competitive efficiencies with carefully controlling the thickness of P3HT to avoid problems associated with voltage loss and high resistance [110, 111]. Xion et al. demonstrated that PANI could act as both the sensitizer and the hole-transporting material in PSCs and reported a PCE of 7.34% as well as excellent long-term stability [112]. A common used HTL in p-i-n PSC structure is the PEDOT:PSS which is a water soluble polymer. Recently the PCE of PEDOT:PSS-based PSC increased rapidly and approaching 19% [113]. However the acidity of such compound pose a fundamental threat to the long-term stability of the PSCs.

Inorganic HTL materials are used in n-i-p PSC for their intrinsic high stability, high internal charge mobility, and generally low cost [109]. Many different inorganic materials have been investigated as HTMs, including CuI (PCE 14.7%) [114], NiO (PCE 12.5%) [115], and CuSCN (PCE 17.5%) [116]. The CuI HTL-based PSCs showed low open-current voltagewhichcan be attributedto higher recombination losses, as was determined via impedance spectroscopy [117]. Optimization of the thickness of the HTL is a promising way to improve the performance of PSC devices. Qin et al. optimized the thickness of a CuSCN-based HTL and were able to achieve a PCE of 12.4% as well as a high short-circuit current due to the enhanced charge extraction from the perovskite and efficient hole transportation to the cathode [118]. Chen et al. found that film thickness of NiOx HTL plays a crucial role in device performance,and with adequate oxygen flow doping of 10%,they managed to improve the performance of hole extraction/-electron blocking layer achieving a PCE of 11.6% [119].

2.8 Conclusion

Perovskites are a wide range of semiconductor materials that exceeds hundreds of types and combinations with the ABX_3 molecular structure. The most used perovskites in solar cell applications are the methyl ammonium halide wher the B metal cation is Pb, Ge or Sn. This chapter exhibited the perovskite architecture and some principal perovskite materials used in photovoltaic technology. It is

noticed that $MAPbI_3$ is the most suitable material for solar energy conversion. However, the lead free $MASnI_3$ and $MAGeI_3$ indicates a good alternative low toxic materials for solar energy harvesting. Therfore, the operation of perovskite solar cells has been described, where both p-i-n and n-i-p planar heterojunction-based PSC will be investigated in this work.

CHAPTER 3

OVERVIEW ON NUMERICAL SIMULATORS

3.1 Introduction

The importance of modeling and simulation of the performance of PVK solar cells cannot be overemphasized. Software simulations present a powerful tool for performance prediction in solar cell application because of the high cost of experiments. One of the most used software simulators for semiconductor behavior is the technology computer aided design (TCAD) software program : Atlas 2018, from the American society Silicon Valley Corporation (Silvaco) [38]. Silvaco Atlas is a powerful text oriented 2D/3D device simulator that we used to predict the electrical characteristics of specific solar cell structure. It provides a set of physical models for different materials, so that users can chose the appropriate one that matches specific material behavior (electrical, optical, ...). In addition, the Solar Cell Capacitance Simulator (SCAPS version 3.3.07) is also a free software used for photovoltaic simulations in this thesis. SCAPS is a 1D graphical oriented simulator developed at the department of Electronics and Information Systems (ELIS) of the University of Gent, Belgium [120]. This software is the result of teamwork of Alex Niemegeers, Marc Burgelman, Koen Decock, Johan Verschraegen and Stefaan Degrave.

In this chapter, simulation softwares are briefly described to have an overview of modeling techniques for each one. More information about each software can be found in more details in [38, 120].

3.2 Silvaco Atlas description

Silvaco Atlas is a 2D and 3D device simulator. It helps researchers to predict semiconductor behavior prior to experimental efforts to enable saving money and time. It is a text oriented simulator in which one have to write a code describing the simulated device and the necessary parameters to be studied.

Figure 3.1 presents the different inputs/outputs of Atlas, where it is distinguished two input files one containing instructions (with .in extension) to be executed and the other holds the structure to be simulated (with .str extension). The command file is generated and/or edited using DeckBuild, while the structure file can be generated and/or edited using DevEdit or Athena. It is to be underlined that Atlas is a device simulator, Athena is used for structure definition and deposition, DevEdit is used for mesh generation, DeckBuild is used for command edition and TonyPlot is used for result visualization. Nonetheless, it is remarked three output files :

1. Run time output that contains details of simulation process such as progress, errors and warnings.
2. Log file that contains obtained final I-V values.
3. Solution file that stores more 2D and 3D data relative to the values of solution variables within the device at a given bias point.

The two last output files can be exploited by TonyPlot for result visualization [38].

Every statement in Atlas software have th following format :

<Statement> <parameter>=<values>

where

- statement : is an Atlas keyword

- parameter : is a set of parameters needed by the Atlas statement.

- value : is the corresponding value of the "parameter".

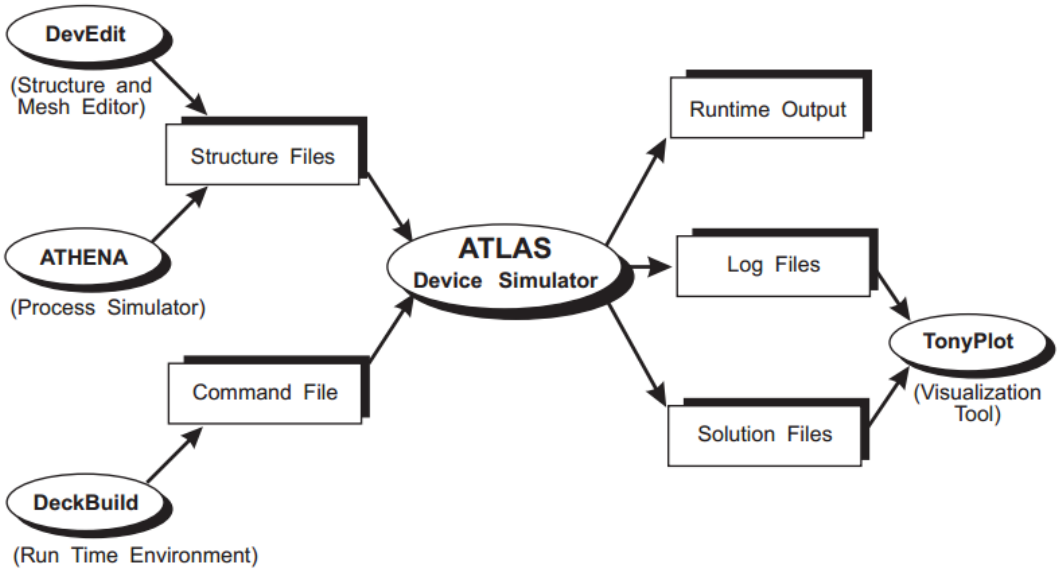

Figure 3.1 – Atlas inputs and outputs.

Parameters in the statement may have four different types of values: logical, integer, real or character.

For example in the following line of code

DOPING P.TYPE CONC=2e15 REGION=3 OUTFILE=output.dop

"DOPING" is the statement, and the remaining are parameters and their corresponding values.

In Atlas, statements are not case sensitive, but being executed under DeckBuild they are case sensitive.

Atlas commands are classified into groups and have imperatively to follow the order presented in Figure 3.2. Firstly, we have to specify the structure to be simulated, then define the material models, after that selection of numerical method to resolve differential equations system, followed by giving the solution specifications and finally analyzing/visualizing the results.

A judicious programming technique is to use a set of constants to define common variables, for example :

set thicketl=0.100
set thickpvk=0.700
set thickhtl=0.200

These commands define the variables "thicketl" (ETL thickness), "thickpvk" (perovskite layer tickness) and "thickhtl" (HTL thickness) to be assigned the values of 0.100 μm, 0.700 μm and 0.200 μm, respectively, which can be modified easily if it is needed.

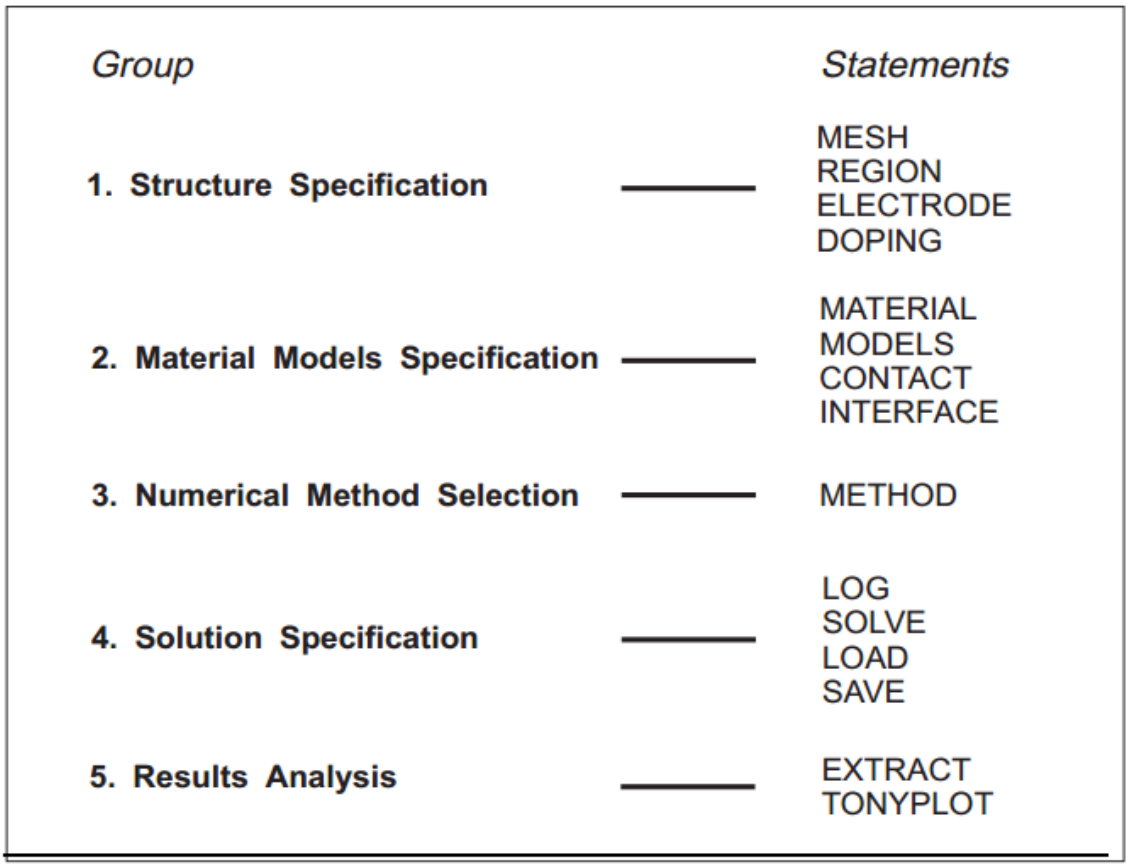

Figure 3.2 – Command order in Atlas.

3.2.1 Structure specification

The first used statement to precise structural parameters is "MESH", which makes a grid with a set of horizontal and vertical lines to describe the device shape. It can be defined according two forms : the standard and the automatic. The first form (standard meshing), can be written according to the following form :

MESH SPACE.MULT=<VALUE>
X.MESH LOCATION=<VALUE> SPACING=<VALUE>
Y.MESH LOCATION=<VALUE> SPACING=<VALUE>

The SPACE.MULT parameter value is used as a scaling factor for the mesh created by vertical and horizontal lines generated by X.MESH and Y.MESH statements, respectively. Its default value is 1. If its value is greater than 1 it will create coarser mesh for fast simulation, and if its value is less than 1 it will create finer mesh for increased accuracy.

The LOCATION parameter value specifies the X.MESH or Y.MESH location.

The second form (automatic meshing) can be written according to the following statement :

```
MESH AUTO
X.MESH LOCATION=-1.0 SPACING=0.1
X.MESH LOCATION=1.0 SPACING=0.1
```

Where SPACING parameter value defines the X direction spacing between vertical grid lines in the LOCATION value position. Y direction meshing will be generated later in the REGION statement. Auto meshing is usually used in devices that have homogeneous X direction (that's the case in solar cells devices). In our work we used the auto meshing, an example of mesh of perovskite solar cell structure is presented in Figure 3.3 according to the following deck :

```
MECH auto
X.MESH LOCATION=0.0 SPACING=0.01
X.MESH LOCATION=1.0 SPACING=0.01
REGION num=1 user.material=TiOx user.group=semiconductor \
bottom thickness=$thicketl ny=$thicketlx*100 donors=3e19
REGION num=2 user.material=CH3NH3SnI3 user.group=semiconductor \
bottom thick=$thickpvk ny=$thickpvk*100 accep=3.2e15
REGION num=3 user.material=spiro user.group=semiconductor bottom \
thick=$thickhtl ny=$thickhtl*100 accep=1e18
```

The second statement "REGION" is used to define materials assigned to each zone of the studied solar cell (see the deck above). Therefore, every REGION statement has the following syntax (in the case of automatic mesh) :

```
REGION number=<integer> <material_type> <user.group=material_group> \
<position> <thick=layer_thickness> <ny=number_of_lines> \
<charge_carrier_concentration>
```

Where the region number must begin from 1 and increases for each subsequent region statement. Atlas software supports up to 15000 different regions,

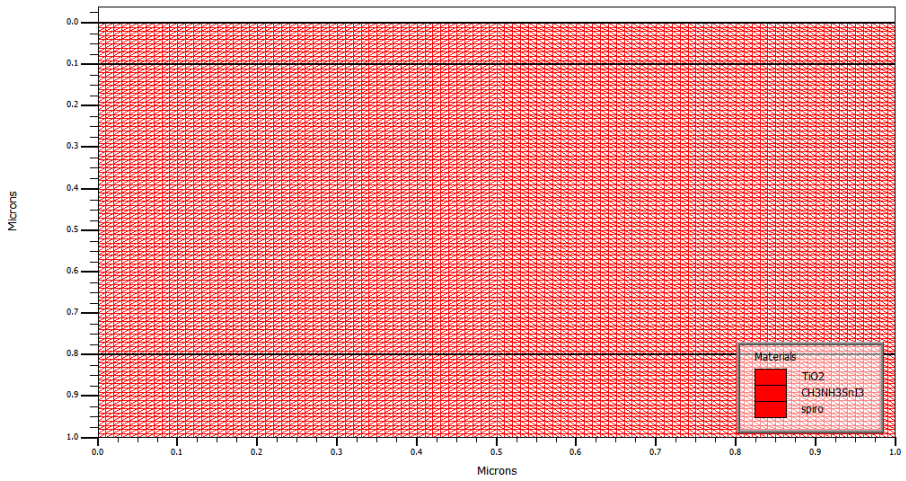

Figure 3.3 – Typical perovskite solar cell structure mesh.

"material_type" defines the name and type of material, in Atlas there is predefined materials in its database, however user can define new materials with the "user.material" parameter.
"user.group" parameter value defines the user defined material group which can take one of three values : conductor, insulator or semiconductor.
"position" parameter can take either "BOTTOM" or "TOP" character values to indicate layer position according to the previous layer.
"thickness" (can be written "thick" only) parameter value gives the layer thickness and "ny" parameter value gives the number of horizontal lines to be generated by the automatic meshing.
"charge_carrier_concentration" parameter defines the charge carrier concentration value of the actual layer. In Atlas there are two types of charge carriers : ACCEPTORS (ACCEP) or DONNORS (DONNOR).

The backslash character indicates that the command continues on the next line.

The third statement is "ELECTRODE" which can be used to define at least one electrode that contacts a semiconductor material as shown in the following line command :

ELECTRODE NUM=<integer> NAME=<electrode_name> <position_parameters> MATERIAL=<material_type>

Where NUM value is an integer that must begin by 1, NAME value specified the electrode name (anode or cathode ...), and "position_parameters" indicates the electrode position on the device (TOP or BOTTOM in the case of automatic meshing) and the MATERIAL parameter value indicates the type of the material (from Atlas database or from user defined materials). For example the following command lines :

ELECTRODE NUM=1 NAME=cathode TOP MATERIAL=ITO
ELEC NUM=2 NAME=anode BOTTOM MATERIAL=gold

determine two electrodes an ITO cathode on top and a gold anode on the bottom. It is to note that Atlas supports up to 50 different electrodes.

The fourth (optional) statement is "DOPING". It is used to specify analytical doping distributions or have Atlas read in profiles that come from either process simulation or experiment.

DOPING <distribution_type> <dopant_type> <position_parameters>

Where "distribution_type" defines the analytical doping distribution (Gaussian, uniform, ...), "dopant_type" indicates whether the dopant is p-type or n-type and "position_parameters" gives the exact zone where doping is applied. For example :

DOPING gaussian p.type conc=2e17 region=5

Which indicates that we have a Gaussian p-type doping in the fifth region with a concentration value of 2e17.

Figure 3.4 demonstrates region and electrodes specification for a typical perovskite solar cell used in our simulations.

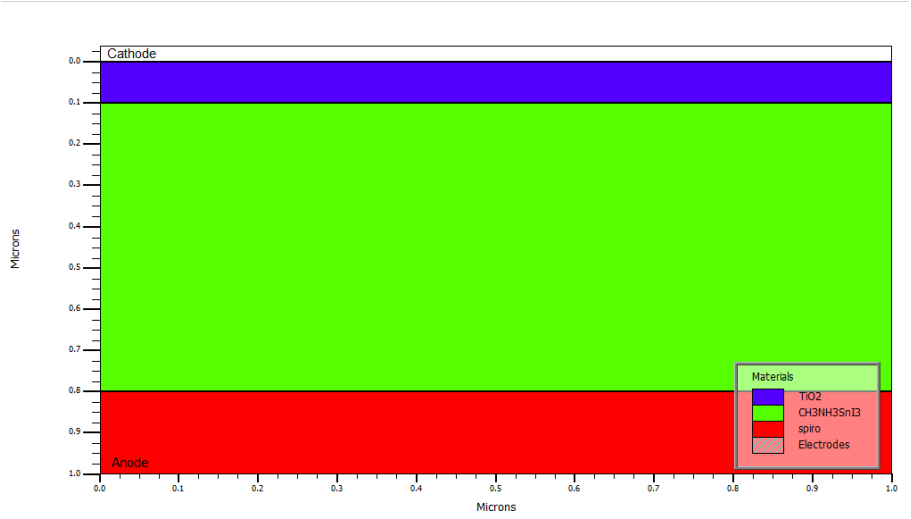

Figure 3.4 – Regions and electrodes specification of typical perovskite solar cell.

3.2.2 Material and model specifications

When structure mesh, geometry and doping profiles are defined, we can modify the parameters of contacts, materials and interfaces. Then, we choose physical models which will be used by Atlas during the device simulation. To accomplish these actions, CONTACT, MATERIAL, INTERFACE, MOBILITY and MODEL statements are used and presented in the following formats :

CONTACT NAME=<contact_name>
WORKFUNCTION=<contact_workfunction>

The contact statement is defined the contact name and the workfunction value.

MATERIAL MATERIAL=material_type \
USER.DEFAULT=default_material_type \
EG300=material_band_gap AFFINITY=material_affinity NC300=NC_value \
NV300=NV_value PERMITTIVITY=relative_permittivity \
TAUP=_tau_p TAUN=tau_n

Where MATERIAL parameter value indicates the material type and USER.DEFAULT parameter value gives the basic material type parameters to be assigned to the new user defined material "material_type". However, the EG300, AFFINITY, NC300, NV300, PERMITTIVITY, TAUP and TAUN parameters values indicates the material band gap Eg at $300°K$, the electron affinity χ, the conduction band effective density of states Nc, the valence band effective density of states Nv, the relative permittivity ϵ_r, hole Shockley-Read-Hall (SRH) recombination lifetime τ_p and electron SRH recombination lifetime τ_n respectively.

INTERFACE <set_of_parameters>

That last statement is used to define interface parameters such as charge density and surface recombination velocity at interfaces between different layers.

MOBILITY <mobility_parameters>

The MOBILITY statement is defined different material mobility parameters according to the material's model.

MODEL MATERIAL=material_type <set_of_material_models>

The MATERIAL statement associate the "material_type" with a set of mobility and recombination models such as : SRH, Langevin, Auger, Poole-Frenkel ...

The following code elucidate these statements :

```
CONTACT NAME=cathode WORKFUNCTION=3.8
CONTACT NAME=anode WORKFUNCTION=5.1

MATERIAL MATERIAL=CH3NH3SnI3 user.default=Organic \
EG300=1.3 affinity=4.17 NC300=1e18 NV300=1e18 permittivity=8.2 \
taup=1.e-6 taun=1.e-6
MATERIAL MATERIAL=spiro user.default=Organic \
EG300=3 affinity=2.45 NC300=2.2e18 NV300=1.9e19 permittivity=3 \
taup=1.e-7 taun=1.e-7
MATERIAL MATERIAL=TiOx user.default=Organic \
EG300=3.2 affinity=4 NC300=2e18 NV300=2e19 permittivity=19 \
taup=1.e-7 taun=1.e-7
INTERFACE S.N=1e8 S.P=0.1 Y.MIN=0.095 Y.MAX=0.105 S.S
MOBILITY MATERIAL=CH3NH3SnI3 MUN0=1.6 MUP0=1.6 \
e0n.pfmob=1e5 e0p.pfmob=1e5
MOBILITY MATERIAL=TiOx MUN=0.20 MUP=0.10
MOBILITY MATERIAL=spiro MUN0=2e-4 MUP0=2e-4 \
e0n.pfmob=1e5 e0p.pfmob=1e5
MODEL MATERIAL=TiOx conmob srh
MODEL MATERIAL=CH3NH3SnI3 pfmob langevin srh
MODEL MATERIAL=spiro pfmob langevin
```

From this example we have the following device structure parameters :

- Two contacts : a cathode of a workfunction value of 3.8 and an anode with a workfunction value of 5.1.
- Three user defined materials with their appropriate electrical and optical parameters.
- An interface between the TiO2 layer and the CH3NH3SnI3 layer (see Y.MIN and Y.MAX values) with an electron surface recombination velocity (S.N) value of 1×10^8 and a hole surface recombination velocity (S.P) value of 1×10^8 with application of semiconductor-semiconductor (S.S) interfacing model.
- Define the mobility parameter values for each layer according to the models assigned later.
- TiOx material associated to the concentration dependent mobility model and the SRH recombination model.
- CH3NH3SnI3 material associated to Pool-frenkel mobility model, Langevin recombination model and SRH recombination model.

- spiro material associated to Pool-frenkel mobility model and Langevin recombination model.

Note :
MUN, MUP, MUN0, MUP0, e0n.pfmob and e0p.pfmob are the electron mobility μ_n, the hole mobility μ_p, the zero field Pool-Frenkel electron mobility μ_{n0}, the zero field Pool-Frenkel hole mobility μ_{p0}, the Pool-Frenkel electron characteristic field and the Pool-Frenkel hole characteristic field, respectively.

3.2.3 Numerical method selection

Parameters in the METHOD statement are used to set the solution technique, specify options for each technique and tolerances for convergence according to the following syntax :

METHOD <gp> <mdp>

Atlas software have various calculation methods among them, three basic types : decoupled (GUMMEL), fully coupled (NEWTON) and decoupled and fully decoupled (BLOCK).

The default used method is NEWTON. However, users can define more than one method as presented in the following line code :

METHOD NEWTON GUMMEL BLOCK

3.2.4 Solution specification

When the device and resolution method are well defined according to the three last sections, the Atlas software is ready to calculate different device output parameters using LOG, SOLVE, LOAD and SAVE statements.

LOG statement is used to define output file name that contains all captured simulation data (especially I-V characteristics) using the following instruction;

LOG OUTFILE=<file_name>

For example the following statement logged data to Sim1.log file :
LOG OUTFILE=Sim1.log

SOLVE statement is used to calculate specific bias points, for example the following line code is used to obtain convergence for the equations used to calculate bias points from 0 V to 1.2 V with a 0.02 step at the anode :

SOLVE vanode=0 vstep=0.02 vfinal=1.2 name=anode

It is to notice that a good initial guess is recommended prior to this line of code using the following instruction :

SOLVE init

LOAD and SAVE statements are used to load previous solutions from a file as initial guess or store all node point information into a specific file, respectively. Th statements can be written as following :

LOAD INFILE=<filename>

SAVE OUTFILE=<filename>

It is to notice that in case of optoelectronic device simulations, one or more light beam have to be defined using the BEAM statement that needs Luminous 2D software (a part of Silvaco family dedicated to optical analysis). The following instruction precised the light source region (NUM=1), location (S.TOP means on top and X.O gives the X position), angle (ANGLE value gives the incidence angle) and solar spectra (AM1.5) :

BEAM NUM=1 S.TOP X.O=0.5 ANGLE=90 AM1.5 VERBOSE TR.MATRIX

In the last statement VERBOSE and TR.MATRIX are logical parameters used to Enables a higher level of diagnostic run-time printing and Specifies that optical absorption and photogeneration analysis in Luminous 2D will be done using the Matrix Method respectively.

3.2.5 Result analysis

In this section, EXTRACT and TONYPLOT statements are used to pick up relevant results and to draw necessary curves and characteristics.

Series of EXTRACT statements are used to display specific results on the run-time output, for example :

```
EXTRACT INIT INFILE="kha1nv1.e-001.log"
EXTRACT NAME="Jsc" max(curve(v."anode", i."cathode"))
EXTRACT NAME="JscmAcm2" $Jsc*1e08*1e03
EXTRACT NAME="Voc" x.val from \
curve(v."anode", i."cathode") where y.val=0.0
EXTRACT NAME="Pm" max(curve(v."anode", (v."anode" * i."cathode")))
EXTRACT NAME="Vm" x.val from curve(v."anode", (v."anode"*i."cathode") ) \
where y.val=$"Pm"
```

EXTRACT NAME="Im" $"Pm"/$"Vm"
EXTRACT NAME="FF" ($"Pm"/($"Jsc"*$"Voc"))*100
EXTRACT NAME="Opt_int" max(beam."1")
EXTRACT NAME="Eff" (1e8*$Pm/$"Opt_int")*100

The first instruction specify the filename file used for parameter extraction, and the second one is used to extract the short circuit density of current Jsc (A/m^2). The next statement for unit changing of Jsc from A/m^2 t mA/cm^2. The fourth statement extracts the Voc (V) characteristics. The next three statements are used to extract solar cell max power Pm, max voltage Vm and max density of current Jm, respectively. After that, the fill factor is deduced from previous parameters, then the light beam is normalized and the last statement is used to extract the power conversion efficiency Eff.

TONYPLOT statement is used to plot I-V curves from file.log using the following instruction;

TONYPLOT <file.log>

3.3 SCAPS description

SCAPS program is a 1D graphical oriented software based on drift and diffusion physical model. The graphical interface of SCAPS 3.3.07 is shown in Figure 3.5 [120].

Once SCAPS software is started, simulation steps are:

1. Clic the orange "Set problem" button to define the problem, thus the geometry, materials and all properties of studied device.
2. Indicate the circumstances in which one want to do the simulation, i.e. specify the working point using zone 1 in Figure 3.5.
3. Indicate what curves one needs to calculate, i.e. which measurement one wants to simulate using the fields in zone 2 in Figure 3.5 (I-V,capacitance-voltage characteristics C-V, frequency-voltage characteristic C-F or quantum efficiency characteristics QE).
4. Set up calculation using gray buttons in zone 3 of 3.5 and then start the appropriate calculations using red buttons. It is to notice that it is possible to do single shot, batch, recorder or curve fitting calculations or even execute a script.
5. Display the simulated curves using buttons in zone 4.

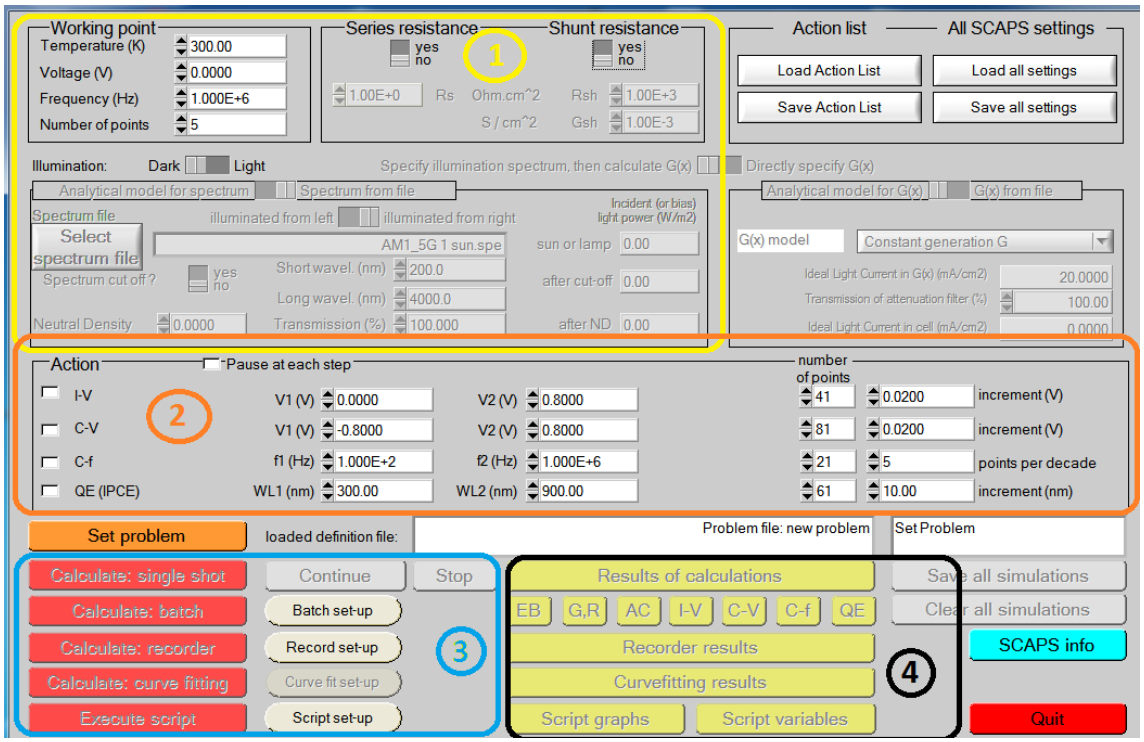

Figure 3.5 – Graphical interface of SCAPS.

Problem definition

By clicking on "Set problem" button (Figure 3.5) we will obtain the graphical interface presented in Figure 3.6.

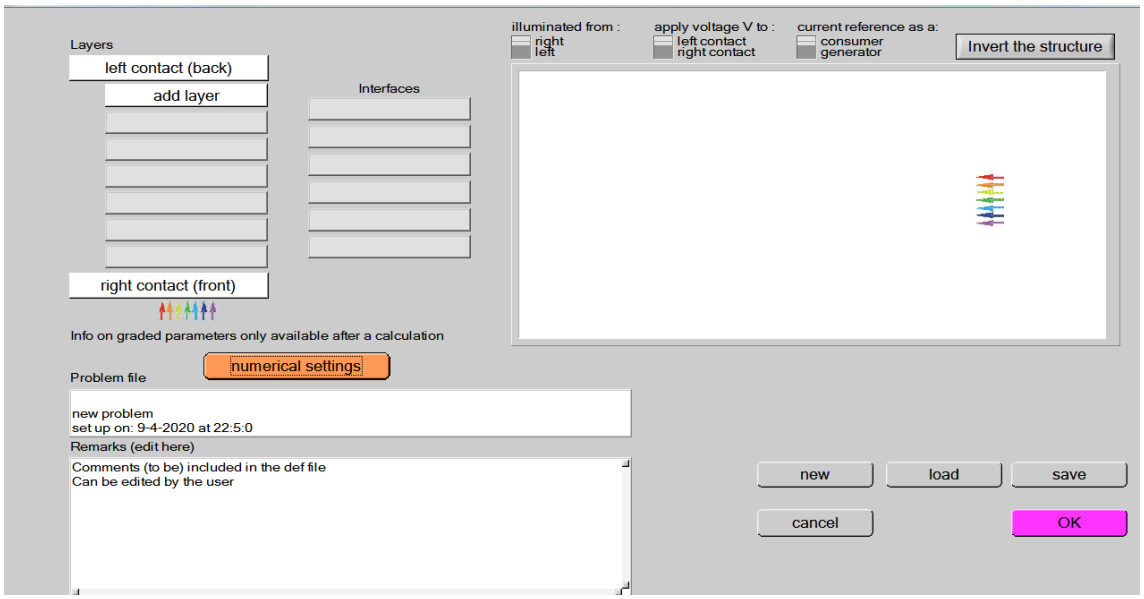

Figure 3.6 – Problem definition interface.

In the interface given by Figure 3.6, different layers can be determined in which we can define seven layers in case of solar cell architeture. Therefore, we can fill the appropriate parameters (including material defects) of each layer, and we can define interlayer defects as given in Figure 3.7.

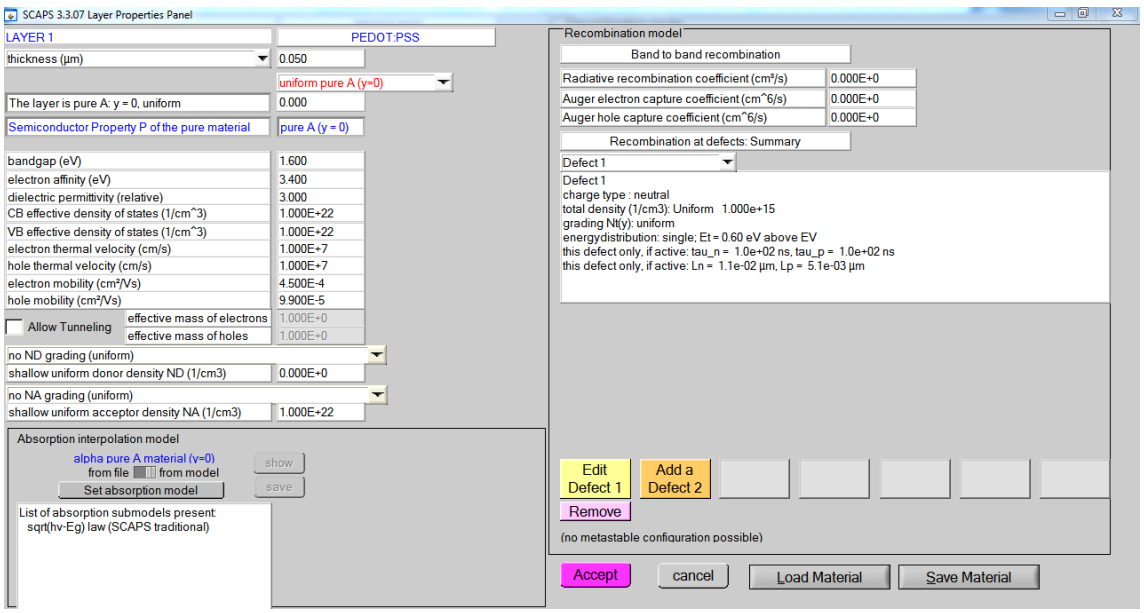

Figure 3.7 – Different electrical and optical parameters of each layer.

For each material it is possible to add defects using "Add defect 1" button (see Figure 3.7) to get the defect properties panel presented in Figure 3.8.

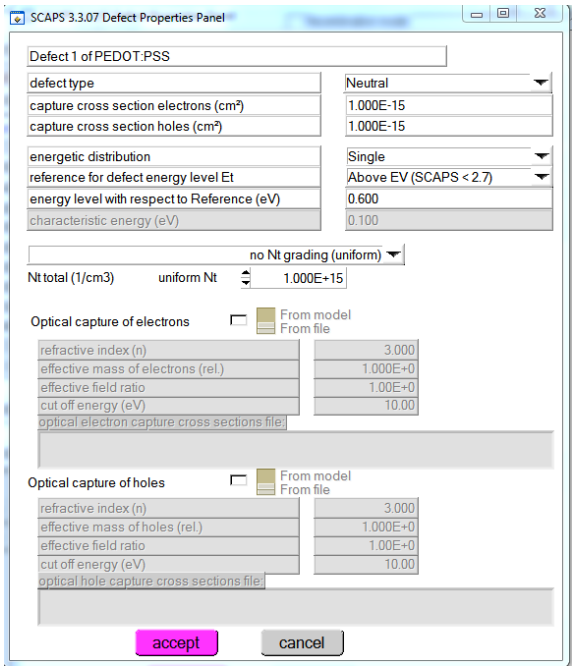

Figure 3.8 – Material defect properties panel.

Once different layers electrical, optical and defect parameters are filled, it is possible to add interlayer defects by clicking on the appropriate button (see Figures 3.6 and 3.9)

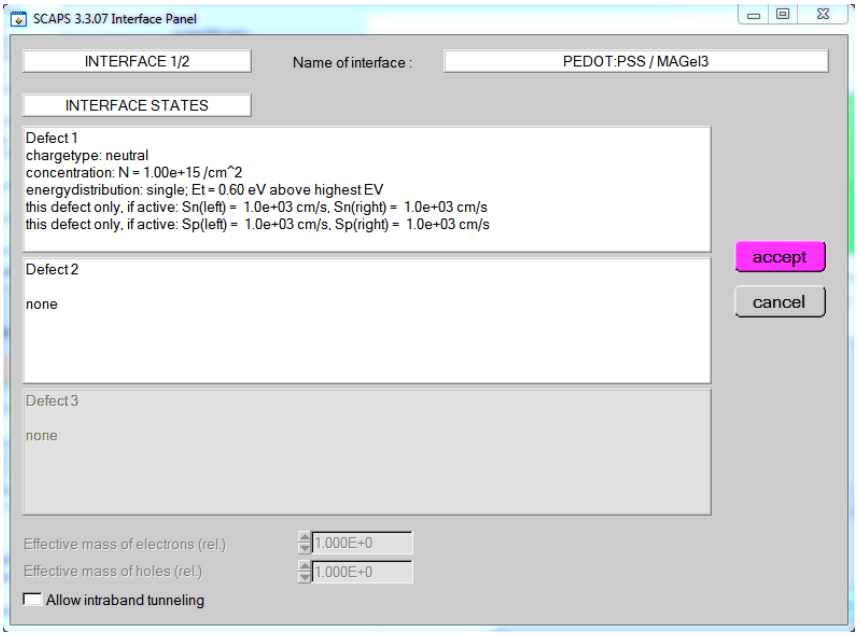

Figure 3.9 – Interlayer defect panel.

Figure 3.10 presents the hole typical perovskite solar cell with material and interlayer defects.

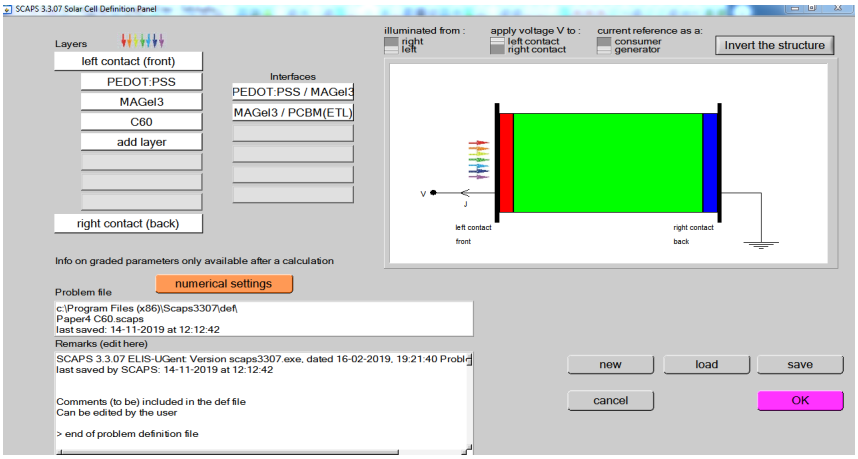

Figure 3.10 – Solar cell definition panel with a typical perovskite solar cell with material and interlayer defects.

By clicking on OK button in Figure 3.10 we will get back to a pannel similar to Figure 3.5, where the "Calculate: single shot" button is then used to begin selected simulation in zone 2 (see results panel on Figure 3.11).

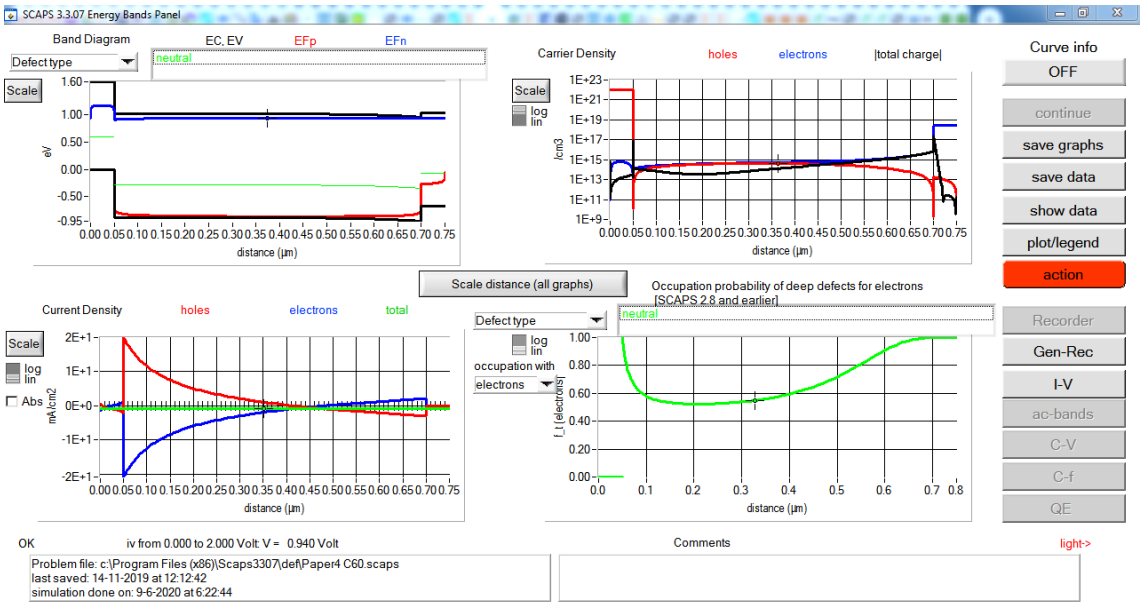

Figure 3.11 – Energy bands panel.

In Figure 3.11, it is possible to visualize the IV curves and extracted Voc, Jsc, FF and PCE by clicking on "I-V button", and hence obtain the I-V panel shown in the following Figure.

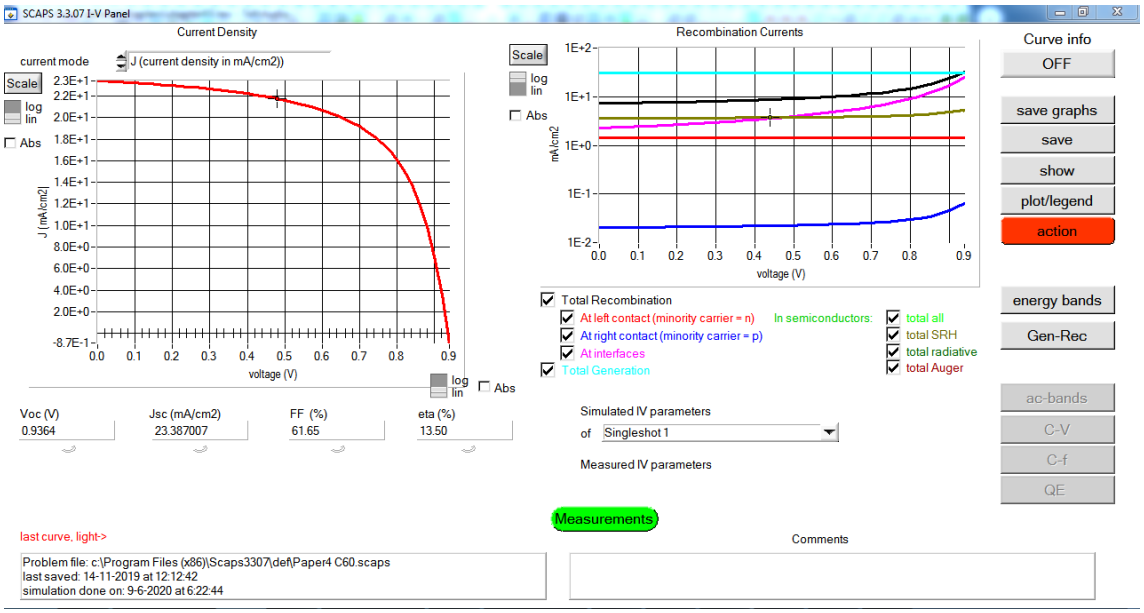

Figure 3.12 – I-V panel.

3.4 Solar radiation spectra

Simulations are achieved under the reference AM1.5 solar spectra presented in Figure 3.13. This spectra is known as the ASTM G173 spectra represents terrestrial solar spectral irradiance on a surface of specified orientation under one and only one set of specified atmospheric conditions. These distributions of power (watts per square meter per nanometer of bandwidth) as a function of wavelength provide a single common reference for evaluating spectrally selective PV materials with respect to performance measured under varying natural and artifical sources of light with various spectral distributions. The conditions selected were considered to be a reasonable average for the 48 continguous states of the United States of America (U.S.A.) over a period of one year. The tilt angle selected is approximately the average latitude for the contiguous U.S.A.

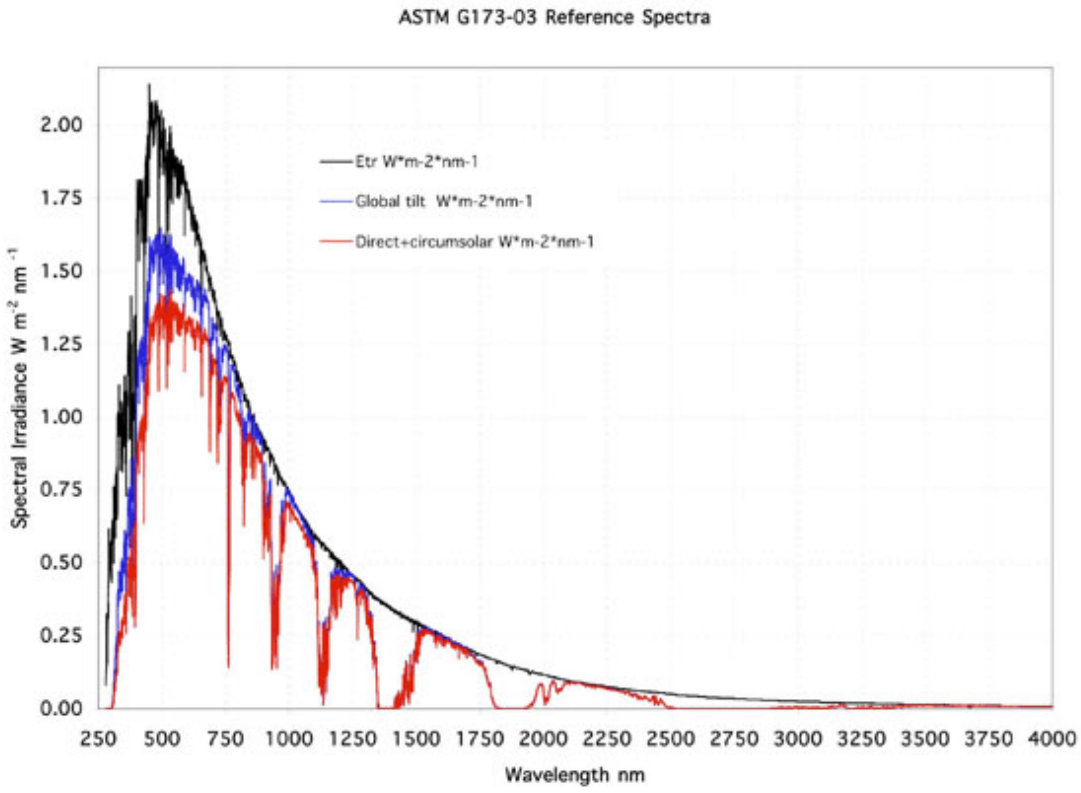

Figure 3.13 – Reference spectra AM1.5.

The receiving surface is defined in the standards as an inclined plane at 37° tilt toward the equator, facing the sun (i.e., the surface normal points to the sun, at an elevation of 41.81° above the horizon)

The specifed atmospheric conditions are:

1. the 1976 U.S. Standard Atmosphere b with temperature, pressure, aerosol density (rural aerosol loading), air density, molecular species density specified in 33 layers
2. an absolute air mass of 1.5 (solar zenith angle 48.19°s)
3. Angstrom turbidity (base e) at 500 nm of 0.084 c
4. total column water vapor equivalent of 1.42 cm
5. total column ozone equivalent of 0.34 cm
6. surface spectral albedo (reflectivity) of Light Soil as documented in the Jet Propulaion Laboratory ASTER Spectral Reflectance Database (http://speclib.jpl.nasa.gov.)

(See description of US standard atmosphere at http://www.pdas.com/atmos.html.)" [1]

To specify AM1.5 solar spectra, define AM1.5 parameter in the appropriate BEAM statement in Atlas. However, to specify this spectra in SCAPS, one have to choice the spectrum file AM1_5G1sun.spe (see Figure 3.14)

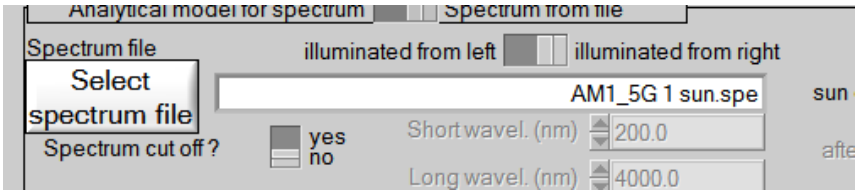

Figure 3.14 – Selecting AM1.5 spectrum in SCAPS.

3.5 Conclusion

This chapter was presented general informations on Atlas and SCAPS programs. It is noticated that Atlas is a 3D text oriented software with a set of statements to define device geometry, electrical and optical parameters and much more informations. It contains a variety of physical models, recombination models and mobility models. Also, the material database of Atlas is extensible. However, SCAPS is a 1D graphical oriented software, where we can fill different fields with appropriate material parameters, and then run the simulations to study and analyze different characteristics. It contains an initial material and solar spectrum database, and also is extensible. Both softwares will be used to study and investigate diverse perovskite based solar cells.

[1] https://rredc.nrel.gov/solar//spectra/am1.5/#about, consulted in 08.17.2019

CHAPTER 4

OPTIMIZATION OF DIFFERENT PEROVSKITE SOLAR CELLS

4.1 Introduction

In the last few years, there has been a surge of interest in the use of perovskite materials in photovoltaic solar cell research has developed exponentially [21], prompting researchers to invest in research to improve the performance of perovskite based photovoltaic cells as well as trying to understand the various internal mechanisms that control several characteristics, including hysteresis [4–8], power conversion efficiency (PCE) [9–13, 121] and stability [15–18].

Power conversion efficiency of perovskite based solar cells was stepped from 3.8% in 2009 [19] up to 25.2% in 2019 [21, 22]. In this context, experimental research investigations are made to increase conversion efficiency and enhance electrical performances of solar cells. Therefore, simulations efforts are also conducted to help sizing (thickness, doping density, band gap, ...) and minimizing experiment costs of solar cells

In this chapter, numerical simulations of diverse structures of perovskite based ($MAPbI_3$ and $MASnI_3$) photovoltaic solar cells have been studied in order to improve the electrical performances of these devices using Atlas 2018 software [38]. The key idea of this work is to find out better layer thicknesses of solar cells to

enhance them power conversion efficiency. For this reason, the effect of layer thickness of different materials (electron transport layer, hole transport layer and perovskite layer) on various electrical parameters of the studied solar cells are presented and discussed to find out optimal configuration.

4.2 Device structure and simulation methodology

As can be seen from Figure 4.1, the n-i-p perovskite based planar heterojunction solar cell design is considered where TiO_2 is used as electron transport layer (ETL), spiro-OMeTAD is used as hole transport layer (HTL) for both structures. $CH_3NH_3PbI_3$ and $CH_3NH_3SnI_3$ are used as absorber layer for the first and the second structure, respectively. All the work on the computer simulations was carried out using SILVACO ATLAS software to study the effect of different layer thicknesses on solar cell electrical performances, namely, Jsc, Voc, FF and PCE.

As other software simulators (SCAPS, GPVDM and wxAMPS) use the drift-diffusion model and don't make difference between organic or inorganic materials, the present work uses SILVACO ATLAS device software having different physical models such as the Organic model for the provskite and the HTL layers which are organic materials. Table 4.1 shows different material type and models for each layer of both structures used in the simulation. Therefore, the corresponding material proprieties [122–127] used for each layer are presented in Table 4.2. It is to note that Pool-frenkel field mobility model is suitable for organic material's mobility [123]. This should be done in conjunction with the Langevin recombination model. Langevin recombination is needed to enable exchange between charged carriers and singlet and triplet excitons [38, 125]. However carrier concentration model is recommended for TiO_2 mobility [122, 124] which is suitable to inorganic materials.

The absorption parameters of perovskite and hole transport layers are taken from literature [122, 128] while for TiO2 layer they are taken from SILVACO Atlas database [38]. It is to underline that the simulated structures are under a 300 °K temperature.

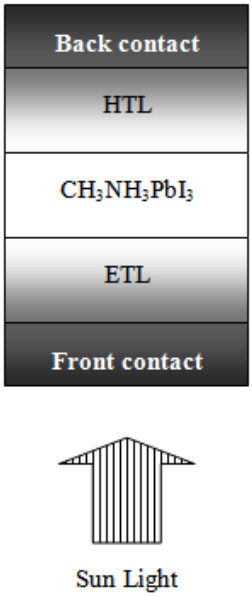

Figure 4.1 – First structure model

Table 4.1 – Different material type, mobility and recombination models for each layer.

Layer	**Material type**	**Mobility model**	**Recombination model**
ETL	inorganic	Carrier concentration	Shockley-Read-Hall (SRH)
HTL	organic	Poole-Frenkel field	Langevin and SRH
PVK	organic	Poole-Frenkel field	Langevin

Table 4.2 – Material property for each layer.

Material property	**spiro-OMeTAD**	**$MAPbI_3$**	**$MASnI_3$**	**TiO_2**
Thickness (nm)	700	200	200	100
Eg (eV)	3	1.55	1.3	3.2
χ (eV)	2.45	3.9	4.17	4
Nc (cm^{-3})	2.2×10^{18}	2×10^{18}	10^{18}	2×10^{18}
Nv (cm^{-3})	1.9×10^{19}	2×10^{19}	10^{18}	2×10^{19}
N_D (cm^{-3})	-	10^{13}	-	3×10^{19}
N_A (cm^{-3})	10^{18}	-	3.2×10^{15}	-
ϵ_r	3	100	8.2	19
μ_n $(cm^2V^{-1}s^{-1})$	2×10^{-4}	1	1.6	0.2
μ_h $(cm^2V^{-1}s^{-1})$	2×10^{-4}	1	1.6	0.1
τ_n (s)	10^{-7}	10^{-6}	10^{-6}	10^{-7}
τ_p (s)	10^{-7}	10^{-6}	10^{-6}	10^{-7}

In order to find the optimized layer thicknesses that corresponds with the maximum power conversion efficiency of both structures, the following steps have been applied using parameters in Table 4.2;

- Hole transport layer and electron transport layer thicknesses are constant and equal to 700 nm and 100 nm, respectively while the perovskite layer thickness is variable from 100 nm to 900 nm with a step of 100 nm.
- The optimal perovskite layer thickness that gives a maximal PCE value is fixed. The electron transport layer thickness is also fixed in 100 nm and the hole transport layer thickness will change from 100 nm to 900 nm with a step of 100 nm.
- The optimal hole transport layer thickness that gives a maximal PCE value is fixed. Also perovskite layer thickness has previously been fixed and electron transport layer thickness is variable from 100 nm to 900 nm with a step of 100 nm.

Finally, the obtained optimized layer thicknesses of different materials for both structures that match the maximal PCE value are found and discussed in next section.

4.3 Results and discussions

Simulations were carried out using parameters given in Tables 4.1 and 4.2. According to simulation methodology discussed above, Figure 4.2 shows the effect of $MAPbI_3$ and $MASnI_3$ perovskite layer thickness on different electrical parameters of the PSC. It is shown that Jsc (Figure 4.2a) increases with increasing of perovskite layer thickness in both cases ($MAPbI_3$ and $MASnI_3$) to a saturation values of $23.99 mA/cm^2$ and $19.03 mA/cm^2$, respectively. This can be explained by more material exposed to light and hence more absorbed energy in this layer which generates more pair electron-hole. Therefore, the electron mobility will be increased. It is noticed that the first structure demonstrates a better Jsc behavior. Figure 4.2b presents the variation of Voc along the perovskite layer thickness. This later is approximately still constant around 1.1 V and 0.8 V in both structures the first and the second, respectively. However, the FF is decreasing from 88.09 % to 63.59 % when the perovskite thickness layer is increasing in case of the first structure and similarly variation for the case of second structure. This is due to the internal recombination in PVK material because of the short charge carriers life time (τ_n, τ_h) that do not allow enough time for charge carrier to get conduction band at PVK material.

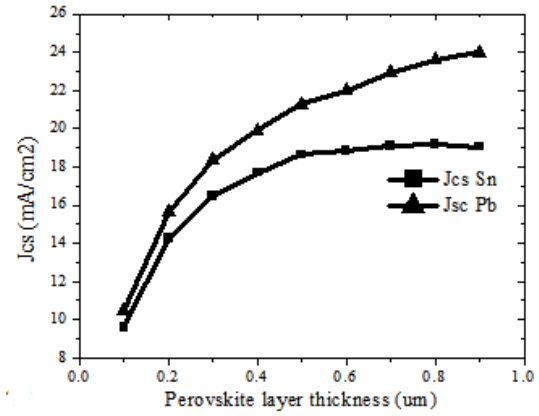

(a) PVK thickness effect on Jsc

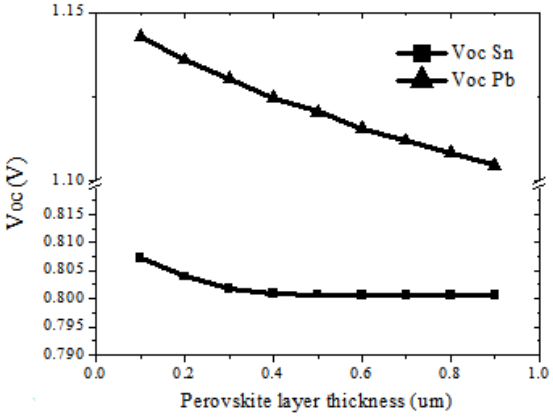

(b) PVK thickness effect on Voc

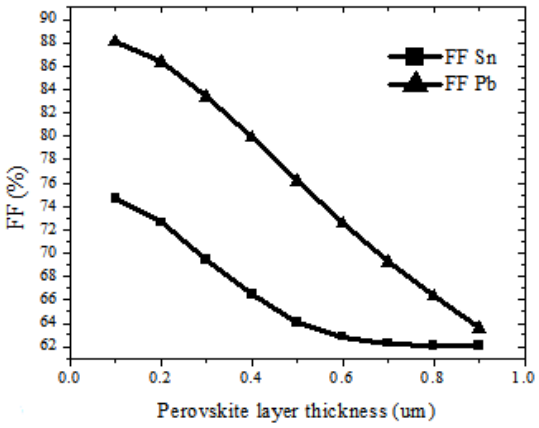

(c) PVK thickness effect on FF

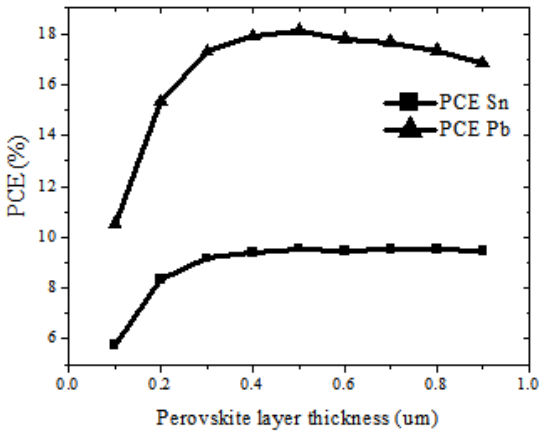

(d) PVK thickness effect on PCE

Figure 4.2 – Effect of $MAPbI_3$ and $MASnI_3$ perovskite layer thickness on electrical parameters of both structures, where hole transport layer and electron transport layer thickness are 700 nm and 100 nm, respectively

The variation of PCE for both structures as function of perovskite layer thickness is shown in Figure 4.2c. As can be seen from the last mentioned figure, PCE is increasing with increases of $MAPbI_3$ perovskite layer thickness from 10.54 % to a maximal value of 18.14 % which corresponds to thickness values of 100 nm and 500 nm, respectively, then decreases to 16.84 % with the thickness of 900 nm. Whereas, for the $MASnI_3$ perovskite based structure, the power conversion efficiency increased considerably from the perovskite layer thickness of 100 nm to 500 nm which corresponds to 5.78 % and 9.56 %, respectively. This can be explained by a considerable increasing of Jsc between 100 nm and 500 nm and a noticeable decreasing in FF at 900 nm. It is evident that $MAPbI_3$ perovskite based structure shows a better performance in comparison of that of $MASnI_3$ perovskite based structure. This can be explained by the difference of band gap and absorbance values of $MAPbI_3$ and $MASnI_3$.

Figure 4.3 illustrates the effect of hole transport layer thickness on Jsc, Voc, FF and PCE for both structures. The values of Jsc (Figure 4.3a) for both structures is around 21.1 mA/cm^2 and 18.5 mA/cm^2 for $MAPbI_3$ and $MASnI_3$, respectively. The variation of Voc as function of hole transport layer thickness is presented in Figure 4.3b where its value is around of 1.12 V for the first structure and 0.8 V for the second structure. Therefore, a slight effect of hole transport layer thickness on fill factor (Figure 4.3c) and it is approximately 76 % and 64.2 % for the first and second structure, respectively.

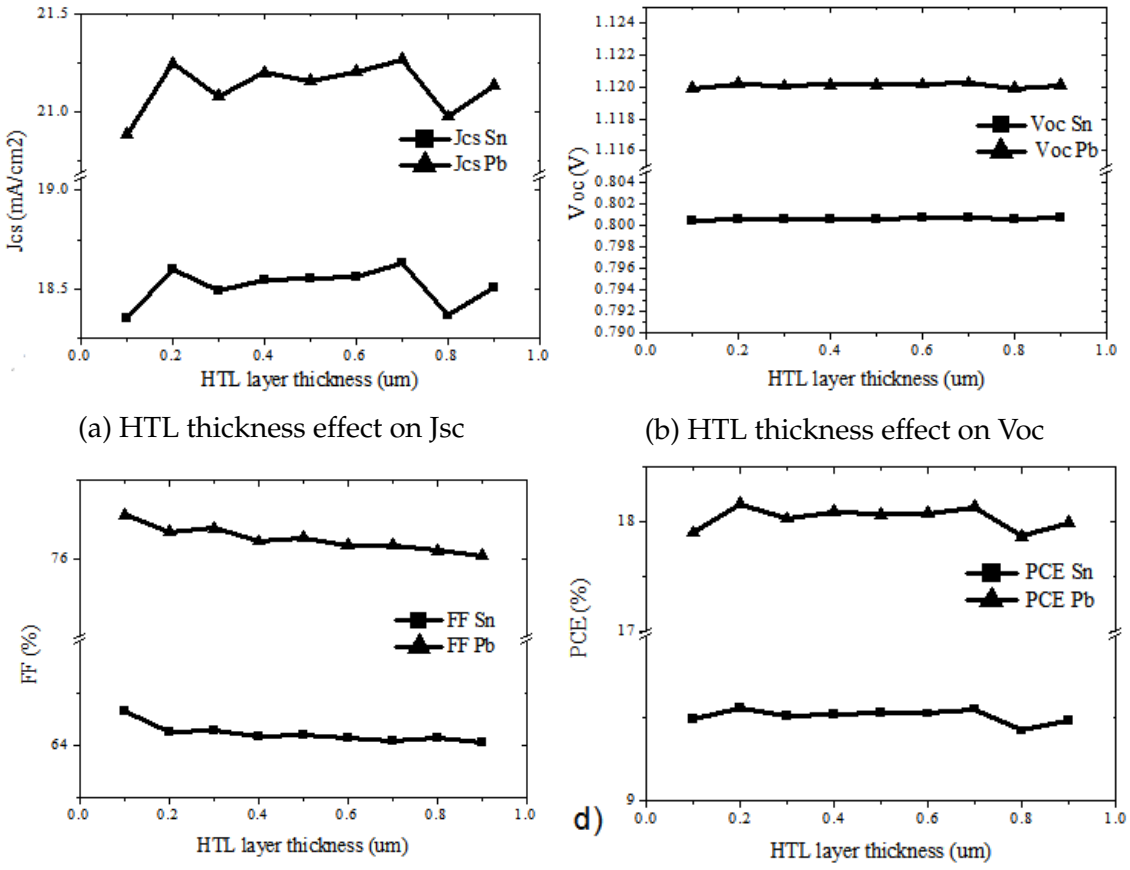

(a) HTL thickness effect on Jsc

(b) HTL thickness effect on Voc

(c) HTL thickness effect on FF

(d) HTL thickness effect on PCE

Figure 4.3 – Effect of hole transport layer thickness on electrical parameters of both structures, where perovskite and electron transport layer thicknesses are 500 nm and 100 nm, respectively.

In Figure 4.3d, the maximum power conversion efficiency is found at hole transport layer thickness of 200 nm which equals to 18.16 % for the first structure, whereas it is maximal, equals to 9.56 %, at hole transport layer thickness of 200 nm for second structure. It is clearly shown from figures that no considerable effect of hole transport layer thickness on different electrical parameters for both solar cells-based designs. This is due to the constant number of charge carriers generated in the PVK layer.

Figure 4.4 displays the effect of electron transport layer thickness on various electrical parameters of both structures. It is observed that no significant effect of electron transporting layer thickness on different electrical parameters (Jsc, Voc and FF according to Figures 4.4a, 4.4b and 4.4c, respectively) because of the invariable number of charge carriers generated in the PVK layer. Therefore, the maximum power conversion efficiency values obtained are 18.16 % and 9.56 % (Figure 4.4d) for the first and the second structure, respectively. These values correspond of electron transport layer thickness of 100 nm for both designs.

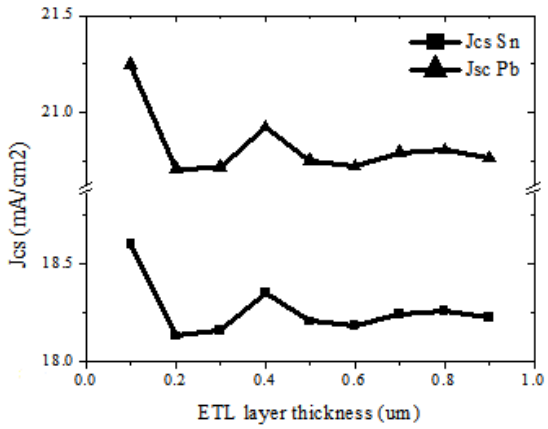

(a) ETL thickness effect on Jsc

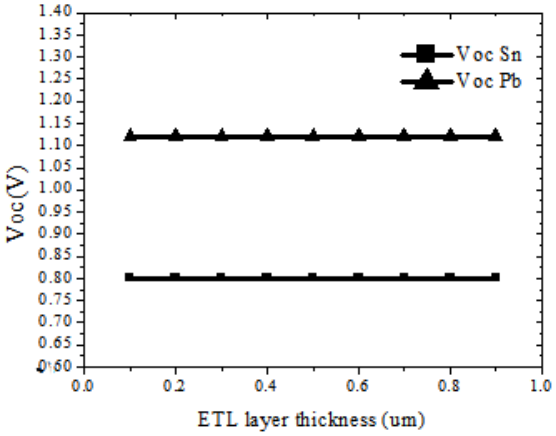

(b) ETL thickness effect on Voc

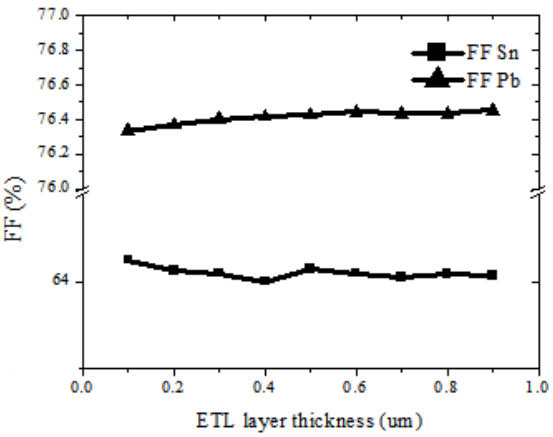

(c) ETL thickness effect on FF

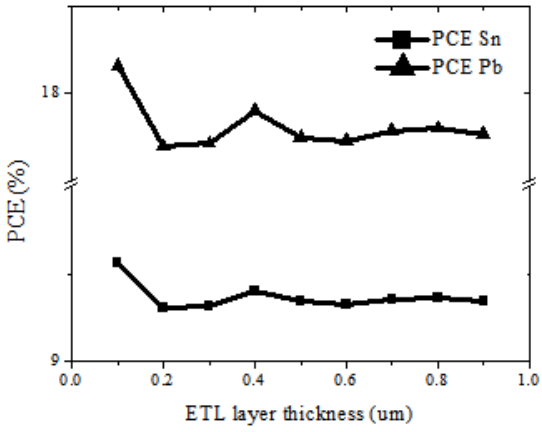

(d) ETL thickness effect on PCE

Figure 4.4 – Effect of hole transport layer thickness on electrical parameters of both structures, where perovskite and electron transport layer thicknesses are 500 nm and 100 nm, respectively.

From Figures 4.2, 4.3 and 4.4 it is noticeable that the maximal PCE value for simulated n-i-p heterojunction photovoltaic solar cell of $MAPbI_3$-based perovskite equals to 18.16 % and in case of $MASnI_3$-based perovskite it equals to 9.56 %. Moreover, the optimized layer thicknesses of perovskite, hole transporting layer and electron transporting layer for both solar cell designs obtained are equal to 500 nm, 200 nm and 100 nm, respectively.

Table 4.3 presents the values of different electrical parameters (Jsc, Voc, FF and PCE) of the simulated structures depending on layer thicknesses mentioned in Table 4.1, optimized ones, and experimental results found in literature [92, 129]. As can be seen from the Table 4.3, the optimized results are so close to experimental measurements except for the FF of the second structure, its value is different of experimental one and this is due to impurities found in real materials and interlayer defects established between ETL/PVK and HTL/PVK layers.

Using the obtained optimized layer thicknesses of both structures, the J-V characteristics of both optimized structures with comparison of that using no- optimized structure and experimental one are given in Figures 4.5a and 4.5b, respectively. It is demonstrated that optimized structures of both cases show a better performance in comparison of no-optimized structures. Hence, the obtained results are so close to experimental ones for the first structure [92].

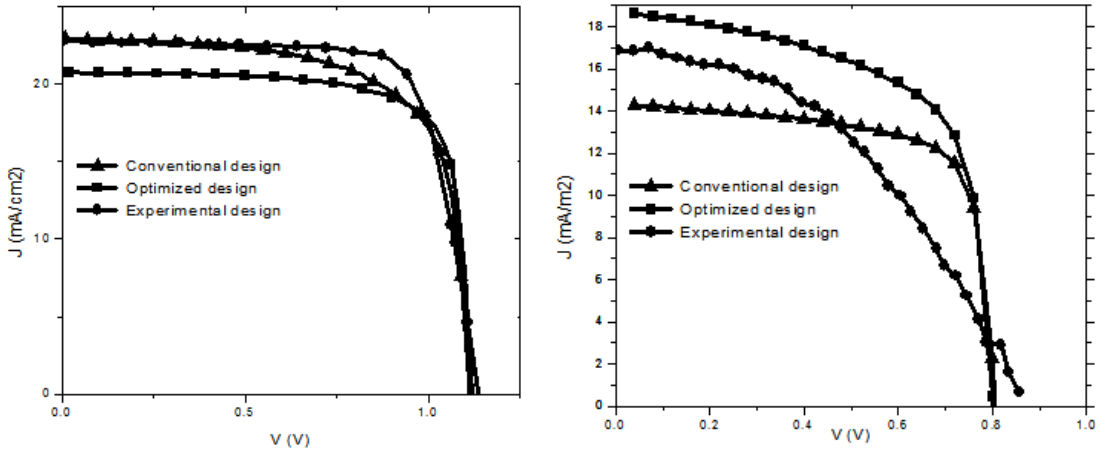

(a) First structure (b) Second structure

Figure 4.5 – J-V characteristics of conventional, optimized and experimental designs for both structures

Table 4.3 – Optimized electrical parameters for diverse device designs

Parameters		First structure			Second structure		
		No-optimized design	Optimized design	Experimental design	No-optimized design	Optimized design	Experimental design
Thickness	ETL	100	100	40	100	100	50
	HTL	700	200	200	700	200	600
	PVK	200	500	350	200	500	400
Jsc		22.93	21.24	22.75	14.25	18.63	16.8
Voc		1.11	1.12	1.13	0.8	0.8	0.88
FF		69.24	76.33	75.01	72.63	64.8	42
PCE		17.64	18.16	19.3	8.32	9.56	6.4

4.4 Conclusion

In this chapter, modeling and optimization of perovskite solar cells based on $MAPbI_3$ and lead free $MASnI_3$ according the n-i-p structure was presented. It is found that the perovskite layer thickness of both $MAPbI_3$-based solar cell and $MASnI_3$-based solar cells have an important effect on electrical parameters in comparison with that of hole and electron transporting layers. Therefore, the obtained results show that perovskite based on $MAPbI_3$ has better electrical performances than perovskite based on $MASnI_3$. The found optimized layer thicknesses values are 100 nm, 200 nm and 500 nm for electron transport layer, hole transport layer and perovskite layer, respectively, which provide the better power conversion efficiency of 18.16% and 9.56% for both $MAPbI_3$ and $MASnI_3$-based solar cell, respectively. Furthermore, the obtained results are close to experimental ones (in case of $MAPbI_3$-based structure) found in literature. Thus, this numerical model provides guidance and can be used to predict other solar cells-based devices for enhanced solar cells conversion efficiency.

CHAPTER 5

EFFICIENCY ENHANCEMENT OF $MAGEI_3$-BASED SOLAR CELLS

5.1 Introduction

Despite the high performance provided by lead halide perovskite material, the factor of instability and toxicity may hamper its commercial production [130–133]. The better way about improving these factors, an alternative candidate ecologic perovskite material is introduced and replacing the Pb-perovskite. The Ge-perovskite material may potentially provide analogous photovoltaic performances similar to Pb-perovskite devices. In this context, this chapter presents numerical simulations of lead free methylammonium germanium tri-iodide ($MAGeI_3$)-based solar cell using 1D-Solar Cell Capacitance Simulator (1D-SCAPS) developed at the Department of Electronics and Information Systems (ELIS), University of Gent, Belgium which is a one dimensional solar cell simulator based on the drift diffusion physical model [120]. The photovoltaic performances of Ge-perovskite solar cell is compared to that of Pb-perovskite solar cell and the obtained results are validated by experimental ones taken from literature [134] showing a good agreement between them. Therefore, the work is extended to study and investigate the ETL/HTL materials effect on Ge-perovskite solar cell design in order to enhance the electrical performances of solar cell. Moreover, the obtained results might indicate a suitable ETL/HTL materials for improving the photovoltaic performance of solar cells based on Ge-perovskite material.

5.2 Part 1 : ETM effect on performance of $MAGeI_3$-based solar cell

In typical perovskite solar cell design, a perovskite absorber material is sandwiched between an electron transport material (ETM) and a hole transport material (HTM). To improve the reproducibility and stability of perovskite solar cells, it is important to select suitable ETM of these devices. In this part, we will investigate and study perovskite solar cells based on germanium with diverse kinds of ETMs.

5.2.1 Device structure and methodology

The basic perovskite solar cell p-i-n structure is presented in Figure 5.1. It consists of three different layers, a perovskite absorbing layer (PAL) which is sandwiched between an electron transporting layer (ETL) and a hole transporting layer (HTL). The PAL represents one of both perovskite materials, $MAPbI_3$ or $MAGeI_3$. Whereas, the PEDOT:PSS is used as HTL and various material types are inserted as ETL. In perovskite devices, ETL is connected at metal back contact (silver, Ag) and HTL at the transparent conducting indium tin oxide (ITO). Note that the structure is illuminated under AM1.5 solar spectrum with 100 mW/cm^2 incident power density an 300 °K.

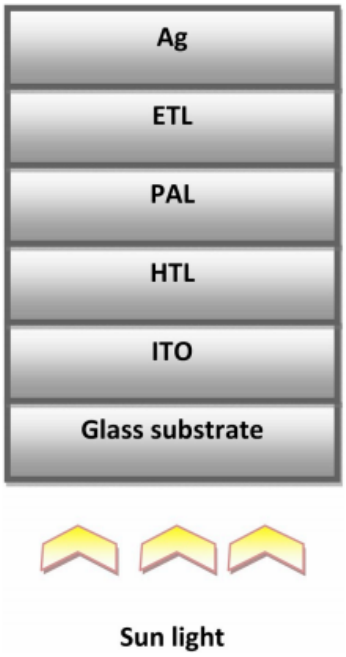

Figure 5.1 – p-i-n perovskite solar cell architecture.

In order to carry out our simulations, different parameter materials related to each layer and collected from recent experimental and simulation studies [81, 135–138] are summarized in Table 5.1. The pre-factor values, A_α, of both ETL and HTL is set to 10^5 to achieve the desired curve of absorption coefficient (α) which calculated using the following expression 5.1:

$$\alpha = A_\alpha \left(h\nu - Eg\right)^{1/2} \tag{5.1}$$

Where α is the absorption coefficient, Eg the band gap and ($h\nu$) the incident photons energy.

Table 5.1 – Material property for each layer of perovskite solar cell.

	ITO	PEDOT:PSS	$MAPbI_3$	$MAGeI_3$	PCBM
Eg (eV)	3.65	1.6	1.55	1.9	2
χ (eV)	4.8	3.4	3.75	3.98	3.9
$Nc(cm^{-3})$	5.8×10^{18}	10^{22}	2.2×10^{15}	10^{16}	2.5×10^{21}
$Nv(cm^{-3})$	10^{18}	10^{22}	2.2×10^{17}	10^{15}	2.5×10^{21}
$N_D(cm^{-3})$	10^{20}	0	10^{14}	10^{9}	2.93×10^{17}
$N_A(cm^{-3})$	0	10^{22}	5×10^{16}	10^{9}	0
ϵ	8.9	3	6.5	10	3.9
$\mu_n(cm^2V^{-1}s^{-1})$	10	4.5×10^{-4}	2	16.2	0.02
$\mu_h(cm^2V^{-1}s^{-1})$	10	9.9×10^{-5}	2	10.1	0.02
Defect density (cm^{-3})	-	2.5×10^{15}	1.5×10^{16}	10^{14}	10^{15}

Besides, optical models used for different PAL materials are taken from experimental results found in literature [81,131–133,135–139]. To investigate and study the Ge-perovskite solar cells, numerical simulations are performed to various p-i-n perovskite structures in order to show the influence of each perovskite material on perovskite solar cell performances. Using the methylammonium lead iodide ($MAPbI_3$) as perovskite material in p-i-n perovskite design, simulation results is compared with experimental ones found in literature [134]. Then, the lead-perovskite layer is changed into germanium-perovskite material at the same p-i-n perovskite design showing the effect of Ge-perovskite material on electrical performance of perovskite solar cell. In addition, the ETL material effect on Ge-perovskite solar cell performance is studied and investigated in order to ameliorate the power conversion of solar cell. Moreover, the appropriate ETL material-based perovskite structure may be considered as novel designing for future Ge-perovskite solar cells.

5.2.2 Results and discussions

Numerical modeling was carried out using 1D-SCAPS software and including various material properties given in Table 5.1 and Table 5.2. Firstly, the p-i-n solar cell structure, ITO/PEDOT:PSS/$MAPbI_3$/PCBM/Ag, based on Pb-perovskite material and corresponds to layer thicknesses of 30 nm, 400 nm and 30 nm for HTL, PAL and ETL, respectively is studied and analyzed. Figure 5.2 plots the J-V characteristics of both simulated and experimental Pb-based perovskite solar cell structure measured under reverse voltage. As can be seen from the figure, the obtained simulated results are very close to experimental ones taken from literature [134]. Therefore, the extracted photovoltaic parameters of both simulated and experimental results are presented in Table 5.4. These results indicate that no big difference between both simulated and experimental values which validate our model and the parameters used in the simulation. In second time, using p-i-n solar cell structure, ITO/PEDOT:PSS/$MAGeI_3$/PCBM/Ag, based on Ge-perovskite material and corresponds to the layer thicknesses of 50 nm, 400 nm and 50 nm for HTL, PAL and ETL, respectively. Figure 5.3 displays the variation of J-V characteristic of the Ge-perovskite solar cell. The photovoltaic parameters Jsc, Voc, FF and PCE resultant were 20.66 mA/cm^2 , 0.87 V, 59.79% and 10.79%, respectively. It is necessary to carry out an optimization process of the perovskite device. This can be done by varying the diverse thicknesses for absorber, HTL and ETL layers. In this context, the optimization process consists to fix two layer thicknesses and vary the remaining one. Then, in each case we select the layer thickness that gives the optimal PCE value.

Table 5.2 – Material proprieties of different ETL materials.

	IGZO	C_{60}	SnO_2	ZnO	TiO_2
Eg (eV)	3.05	1.7	3.5	3.3	3.2
χ (eV)	4.16	3.9	4	4.1	3.9
$Nc(cm^{-3})$	5×10^{18}	8×10^{19}	2.2×10^{17}	4×10^{18}	10^{21}
$Nv(cm^{-3})$	5×10^{18}	8×10^{19}	2.2×10^{16}	10^{19}	2×10^{20}
$N_D(cm^{-3})$	10^{18}	2.6×10^{18}	10^{17}	10^{18}	10^{19}
$N_A(cm^{-3})$	0	0	0	10^5	0
ϵ	10	4.2	9	9	9
$\mu_n(cm^2V^{-1}s^{-1})$	15	8×10^{-2}	20	100	20
$\mu_h(cm^2V^{-1}s^{-1})$	0.1	3.5×10^{-3}	10	25	10
Defect density (cm^{-3})	10^{15}	10^{14}	10^{15}	2×10^{17}	10^{15}

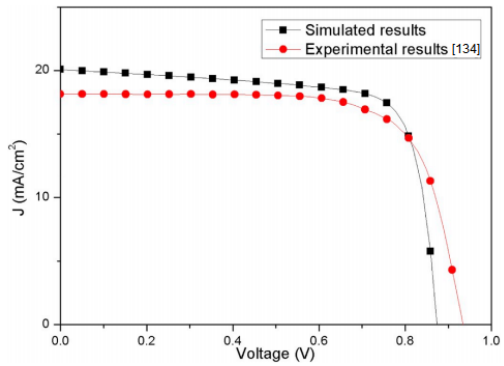

Figure 5.2 – J-V characteristics of both simulated and experimental $MAPbI_3$-based solar cell measured under reverse voltage.

Table 5.3 – Optimized performance of $MAGeI_3$-based solar cell.

Parameters		No-optimized design	Optimized design
Thickness (um)	ETM	50	50
	HTM	50	50
	PVK	400	650
Jsc (mA/cm2)		20.66	23.07
Voc (V)		0.87	0.87
FF (%)		59.79	55.37
PCE (%)		10.79	11.16

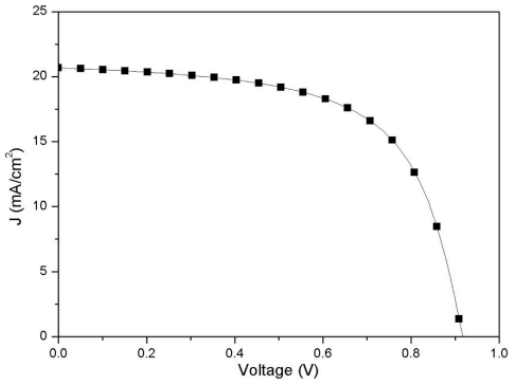

Figure 5.3 – J-V characteristic of no-optimized $MAGeI_3$-based solar cell.

Table 5.4 – Electrical parameters of both simulated and experimental $MAPbI_3$-based solar cell.

	Jsc (mA/cm^2)	**Voc(V)**	**FF(%)**	**PCE (%)**
$MAPbI_3$-based solar cell (simulated)	20.08	0.87	75.28	13.22
$MAPbI_3$-based solar cell (experimental results)	18.2	0.93	71.2	12.05

Figure 5.4 shows the optimized J-V characteristics of the Ge-based perovskite solar cell compared to that of no-optimized structure. It is evident that the optimized perovskite device shows a noticeable enhancement in PCE from 10.79% to 11.16%. Consequently, the obtained optimized characteristic parameters and layer thicknesses of different materials are reported in Table 5.3. As illustrated from the table, Ge-based perovskite device shows analogous photovoltaic performance comparable to Pb-based perovskite device.

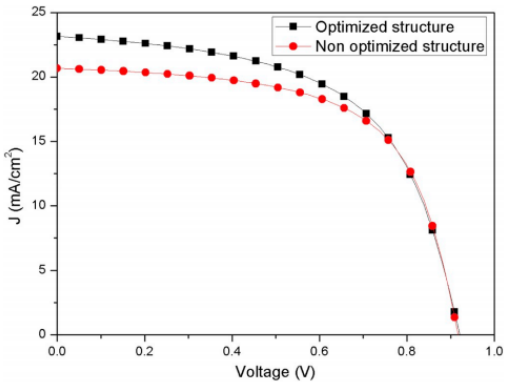

Figure 5.4 – J-V characteristic of no-optimized $MAGeI_3$-based solar cell.

To obtain strongly performance of Ge-based perovskite solar cell with more reproducibility and high stability, diverse kinds of ETL materials effect such as IGZO, SnO_2, C_{60}, TiO_2 and ZnO are studied and results are compared to PCBM. Therefore, the material proprieties of different ETL taken from literature [34,140–145] are given in Table 5.2.

Using the same optimization method mentioned above, our simulation is performed on the power conversion efficiency as function of absorber layer thickness for different types of ETLs in order to find the optimum absorber thickness. The optimized thicknesses of both absorber and ETL layers which give the higher PCE for various ETL materials is obtained for 650 nm and 50 nm, respectively. Evidently, the PCE increases with increasing of absorber thickness for all proposed ETL materials as illustrated in Figure 5.5. This increasing is due to more photons absorbed by carrier concentration in this layer creating more electron-hole pairs and led to high short-circuit current density in the device. In the case of C_{60}, TiO_2 and SnO_2 materials, the power conversion efficiencies achieve its values of 13.5%, 13.30% and 13.19% respectively, and present the highest efficiencies among other used ETL materials. In addition, C_{60}, TiO_2 and SnO_2 seem more suitable materials for perovskite solar cell which facilitate the extraction and transportation of electrons from perovskite to front contact. However, IGZO displays the lowest

PCE of 10.16% compared to the proposed ETL materials. This characteristic may be due to inadequate bands alignment between the conduction band of IGZO and the LUMO of perovskite. Thus, the optimized obtained values of device performance for different ETL materials are summarized in Table 5.5.

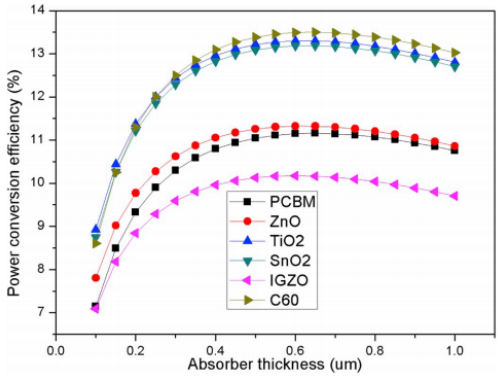

Figure 5.5 – Conversion efficiency against absorber thickness for diverse ETL materials.

Table 5.5 – Photovoltaic parameters of $MAGeI_3$-based solar cell with diverse ETLs and with PEDOT:PSS as HTL.

Various ETL materials	**Jsc** (mA/cm^2)	**Voc(V)**	**FF(%)**	**PCE (%)**
PCBM	23.07	0.87	55;37	11.16
IGZO	23.04	0.81	54.36	10.16
C_{60}	23.38	0.94	61.66	13.5
SnO_2	23.4	0.93	60.39	13.19
ZnO	20.82	0.88	60.64	11.05
TiO_2	23.44	0.93	60.75	13.30

In results illustrated in Figure 5.6, the J-V characteristics of Ge-perovskite solar cell for diverse kinds of ETL materials is presented. It is observed that the better photovoltaic performance is displayed by inserting C_{60}, TiO_2 and SnO_2 as ETL which provide very close values of Jsc, Voc, FF and PCE as shown in Table 5.5. The device performance is significantly enhanced from 11.16% to 13.5% by introducing the C_{60} compared to PCBM. This is can be explained by the use of the appropriate ETL material which could effectively improve the device stability and facilitate the electron transfer from perovskite material and hence minimizing the carrier recombination probability in perovskite cells.

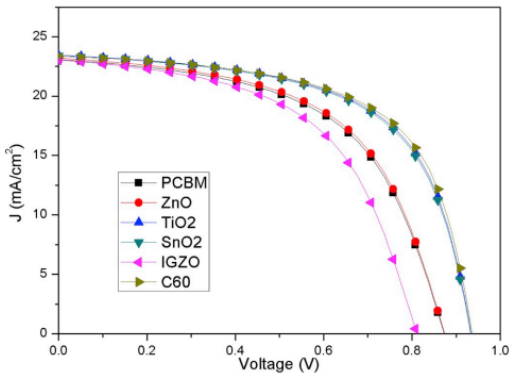

Figure 5.6 – Current density against voltage for various ETL materials.

5.3 Part 2 : Efficiency optimization of $MAGeI_3$-based solar cell using $CuSbS_2$ material

A perovskite solar cell design consists of perovskite material which is sandwiched between ETM and HTM. Accordingly, selecting an appropriate HTM seems an effective strategy for enhancing device performance as well as improving hole extraction from the perovskite and facilitate its transportation in structure. In this scenario, some studies have been used organic materials, such as Spiro-OMeTAD, PEDOT:PSS and D-PBTTT-14 as HTMs [146, 147]. However, the high processing costs and high-purity requirements of these organic materials is the major obstacles for commercialization of PSCs [148]. To solve these issues, alternative inorganic materials (p types) are the better choice because of their superior features as well as high stability and high mobility.

5.3.1 Device configuration

The proposed perovskite solar cell p-i-n structure is given in Figure 5.7, where a perovskite absorbing layer (PAL) is sandwiched between an upper electron transporting material (ETM) and a downer hole transporting material (HTM). The considered PSC design is based on the methylamine germanium tri-iodide ($CH_3NH_3GeI_3$) as absorbing layer and C_{60} as electron transporting material. This later is selected as an appropriate ETM based on results found in literature [146] which gives higher power conversion efficiency of $CH_3NH_3GeI_3$-based PSC.

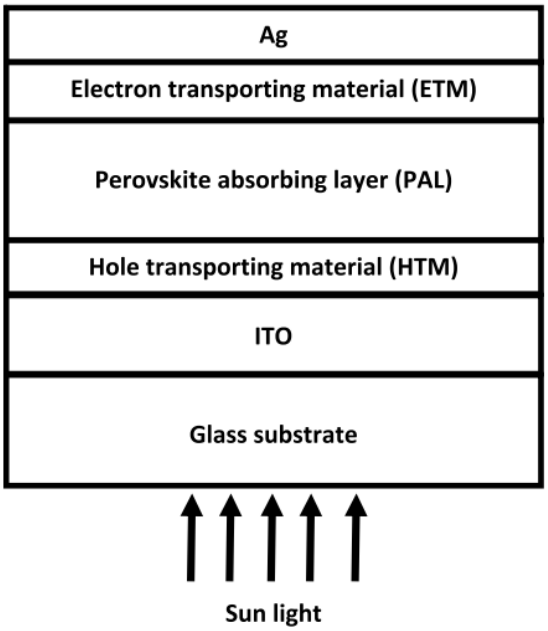

Figure 5.7 – p-i-n perovskite solar cell architecture.

Different hole transporting materials including inorganic materials, such as $CuSBS_2$, CuSCN and NiO are employed. For comparison, PEDOT:PSS is also applied as organic material to PSC structure in order to find a suitable HTM for high efficiency and high stability.

The electrical and optical parameters of different materials used in simulations are selected from literature [134–136, 144, 145, 147, 149, 150], and are exposed in Table 5.6. The perovskite absorption curve is taken from experimental results found in [131]. Therefore, ETM and HTM absorption curves are generated by SCAPS software with pre-factor $A_\alpha = 10^5$ to obtain absorption curve (α) which calculated by equation 5.1.

Noticing that our simulations are performed under the AM1.5 solar spectrum at 100 mW/cm^2 light intensity and 300 °K temperature.

Figure 5.8 shows the energy band alignment of the diverse materials used in the simulation program of our study.

Table 5.6 – Optimized electrical parameters for diverse device designs

	ITO	PEDOT:PSS	CuSCN	$CuSBS_2$	NiO	$MAGeI_3$	C_{60}
Eg (eV)	3.5	1.6	3.4	1.58	3.8	1.9	1.7
χ (eV)	4	3.4	1.9	4.2	1.46	3.98	3.9
$Nc(cm^{-3})$	2.2×10^{18}	10^{22}	2.2×10^{18}	2×10^{18}	2.8×10^{19}	10^{16}	8×10^{19}
$Nv(cm^{-3})$	1.8×10^{19}	10^{22}	1.9×10^{19}	10^{19}	10^{19}	10^{15}	8×10^{19}
$N_D(cm^{-3})$	2×10^{19}	-	-	-	-	10^{9}	2.6×10^{18}
$N_A(cm^{-3})$	-	10^{22}	2.2×10^{18}	2.2×10^{18}	2.2×10^{18}	10^{9}	-
ϵ	9	3	9	8.2	10.7	10	4.2
$\mu_n(cm^2V^{-1}s^{-1})$	20	4.5×10^{-4}	2×10^{-4}	49	12	16.2	8×10^{-2}
$\mu_h(cm^2V^{-1}s^{-1})$	10	9.9×10^{-5}	10^{-2}	49	2.8	10.1	3.5×10^{-3}
Defect density (cm^{-3})	10^{15}	2.5×10^{15}	10^{15}	10^{14}	10^{14}	10^{14}	10^{14}

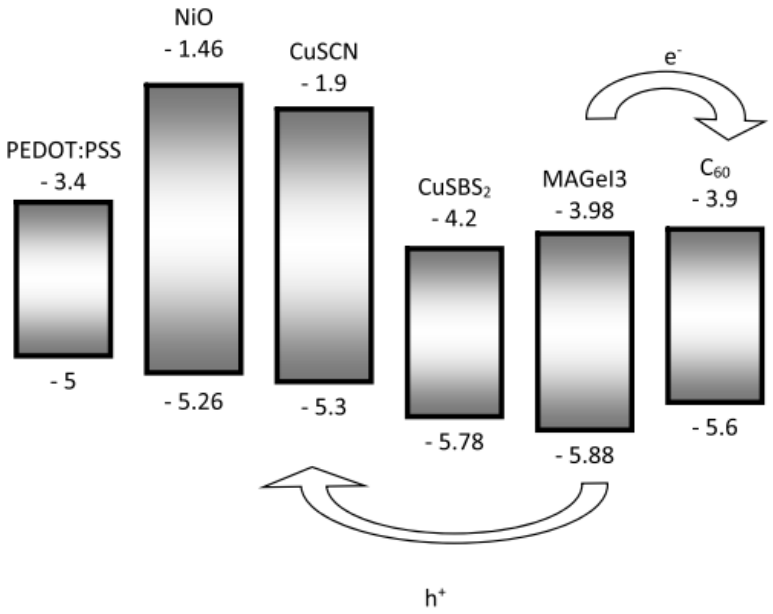

Figure 5.8 – Energy band alignment of different used materials.

5.3.2 Results and discussions

In order to investigate and study the Ge-perovskite solar cells, numerical modeling was carried out using 1D-SCAPS simulation program. Different p-i-n PSC structures are modeled and examined to show the impact of various HTMs on device performances. The p-i-n PSC design, ITO/PEDOT:PSS/$MAGeI_3$/C_{60}/Ag, with layer thicknesses of 80 nm, 400 nm and 80 nm for HTM, PAL and ETM, respectively is studied. Then, PEDOT:PSS is replaced by inorganic materials, $CuSBS_2$, CuSCN and NiO as HTMs in PSC design. Figure 5.9 plots J-V characteristics of various PSC structures introducing four different HTMs, PEDOT:PSS, $CuSBS_2$, CuSCN and NiO. As can be seen from the figure, the values of Jsc of diverse PSC designs employing PEDOT:PSS, $CuSBS_2$, CuSCN and NiO are 18.31 mA/cm^2 , 17.39 mA/cm^2 , 26.53 mA/cm^2 and 26.57 mA/cm^2 , respectively. Additionally, the Voc values are 0.93 V, 1.64 V, 1.17 V and 1.13 V for PEDOT:PSS, $CuSBS_2$, CuSCN and NiO-based PSC structures, respectively. Consequently, the power conversion efficiency of $CuSBS_2$, CuSCN and NiO-based PSC are 19.26%, 21.6% and 20.77% respectively, which are higher than PEDOT:PSS-based PSC. The photovoltaic parameters of four different PSC structures are presented in Table 5.7. It is evident that the performances of PSC are enhanced by insertion of inorganic materials as HTM due to their high mobility and adequate energy bands alignment between HTMs and perovskite material.

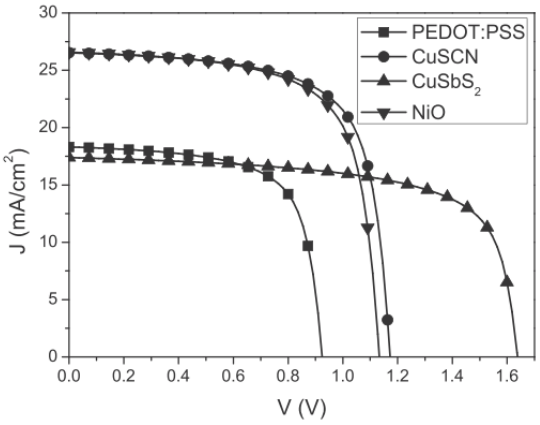

Figure 5.9 – J-V characteristics of $MAGeI_3$-perovskite solar cell based on different HTMs

Table 5.7 – Electrical parameters of $MAGeI_3$-perovskite solar cell with different HTMs.

Different HTMs	**Jsc** (mA/cm^2)	**Voc(V)**	**FF(%)**	**PCE (%)**
PEDOT:PSS	18.31	0.93	68.22	11.55
CuSCN	26.53	1.17	69.38	21.6
$CuSBS_2$	17.39	1.64	67.6	19.26
NiO	26.57	1.13	68.95	20.77

To further performance enhancement of Ge-perovskite solar cells with more reproducibility and high stability, an optimization process is applied to four different PSC designs. In results displayed in Figure 5.10, the photovoltaic parameters (Jsc, Voc, FF and PCE) are plotted as function of absorber layer in order to find the optimum absorber thicknesses of four PSC designs. It is to note that the optimized thicknesses of both ETM and HTM are identical and equal to 50 nm. It is remarkable that the Jsc increases with increasing of absorber thickness in four cases of PSC designs due to more absorbed energy in this layer which creates more electron-hole pairs as illustrated in Figure 5.10a. As shown in Figure 5.10b, above of 300 nm of absorber layer thickness, the Voc is approximately still constant for four cases of PSC structures. It is observed that CuSCN-based PSC, $CuSBS_2$-based PSC and NiO-based PSC demonstrate better behavior in terms of Jsc and Voc in comparison of PEDOT:PSS-based PSC. In addition, FF degrades slightly as absorber thickness increased (Figure Figure 5.10c) in four cases of PSC designs due to high series resistance. Moreover, the PCE increases with increasing of absorber thickness in different cases of HTMs-based PSC as displayed in

Figure 5.10d. Evidently, CuSCN-based PSC, $CuSBS_2$-based PSC and NiO-based PSC present maximum efficiencies compared to PEDOT:PSS-based PSC. This is due to adequate energy bands alignment between the valence bands of CuSCN, $CuSBS_2$ and NiO with the HUMO of perovskite material.

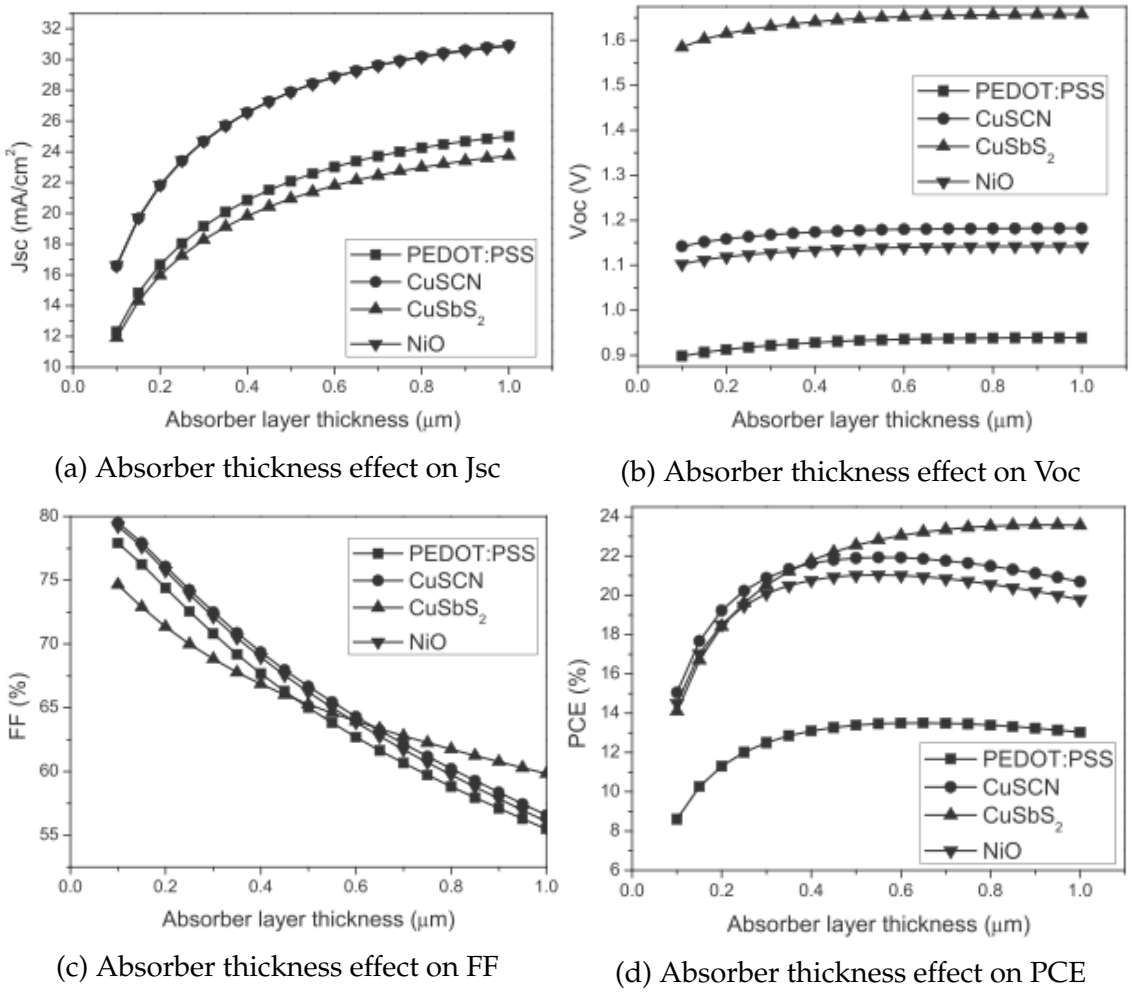

(a) Absorber thickness effect on Jsc

(b) Absorber thickness effect on Voc

(c) Absorber thickness effect on FF

(d) Absorber thickness effect on PCE

Figure 5.10 – Variation of electrical parameters against absorber thickness of $MAGeI_3$-perovskite solar cell with diverse HTMs

The optimized photovoltaic parameters of various PSC designs are reported in Table 5.8. As can be seen from the table, perovskite solar cell formed by $CuSBS_2$ shows the highest PCE reaching 23.58%. Whereas, by inserting CuSCN, NiO and PEDOT:PSS as HTM, their PCE values are 21.93%, 21.04% and 13.5%, respectively. Consequently, $CuSBS_2$ seems more appropriate material for perovskite solar cell which facilitates the extraction and transportation of holes from perovskite to back contact.

Table 5.8 – Optimized photovoltaic parameters of $MAGeI_3$-perovskite solar cell with various HTMs and with C_{60} as ETM.

Different HTMs		PEDOT:PSS	CuSCN	$CuSBS_2$	NiO
Parameters Thickness (μm)	ETM	50	50	50	50
	HTM	50	50	50	50
	PVK	650	550	950	550
Jsc (mA/cm^2)		23.38	28.42	23.59	28.42
Voc (V)		0.94	1.18	1.66	1.14
FF (%)		61.66	65.45	60.29	65
PCE (%)		13.5	21.93	23.58	21.04

The corresponding J-V characteristics of Ge-perovskite solar cell based on four different HTMs are given in Figure 5.11. It is clearly that the better performance is illustrated in case of perovskite solar cell formed by CuSCN, NiO and $CuSBS_2$ as HTM compared to that by PEDOT:PSS. This is can be explained by the introduction of the appropriate HTL material which could potentially enhance the PSC stability and facilitate the hole transfer from perovskite material.

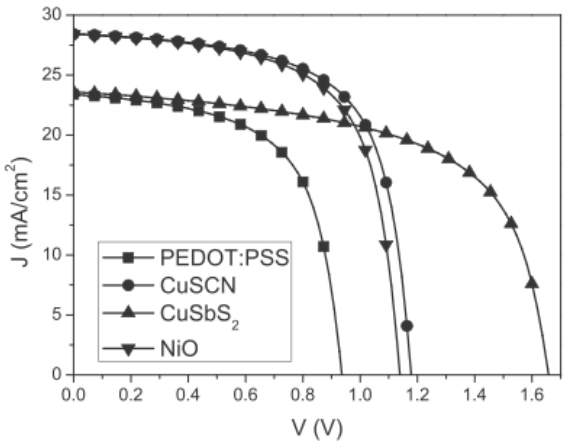

Figure 5.11 – Variation of J-V characteristics of optimized $MAGeI_3$-PSC design with different HTMs.

5.4 Conclusion

In the first part of this chapter, Germanium-based perovskite solar cell is studied and investigated using 1D-Solar Cell Capacitance Simulator (1D-SCAPS). The obtained simulation results of Ge-based perovskite solar cell demonstrate similar photovoltaic performance compared to Pb-based perovskite solar cell and there is no big difference between both structures. In addition, various ETL materials effects on Ge-based perovskite solar cell have been studied and discussed. The performance of Ge-based device was effectively improved by inserting C_{60}, TiO_2

and SnO_2 as ETL compared to other proposed ETL materials. Therefore, the perovskite device with C_{60} exhibits the highest PCE of 13.5% compared to that with other ETL materials. The obtained results designate that C_{60} is an appropriate candidate for enhancing the performance of Ge-based device. Thus, introducing C_{60} in perovskite solar cell structure may be considered as novel designing to fabricate future Ge-perovskite solar cells. On other hand, the second part of this chapter, various hole transport materials such as PEDOT:PSS, CuSCN, NiO and $CuSBS_2$ were inserted to perovskite solar cell based on $CH_3NH_3GeI_3$. The device performance was significantly improved by applying CuSCN, NiO and $CuSBS_2$ as HTM compared to that of PEDOT:PSS. Therefore, an optimization process has been applied, and the power conversion efficiency reaches its maximum value of 23.58% using PSC formed by $CuSBS_2$. This later may be considered as an excellent candidate for enhancing the performance of Ge-perovskite solar cell. Thus, our obtained results illustrated that $CuSBS_2$ is a suitable HTM for fabricating Ge-perovskite solar cell with high efficiency and enhanced stability.

CONCLUSIONS AND FUTURE WORKS

The perovskite based solar cell technologies belongs to the fourth generation photovoltaics. The rapid growth of research in this field is very promising to find out new solar cells with high power conversion efficiency, low processing costs, high stability and nature friendly. From hundreds of perovskite materials, the $MAXI_3$ family, where X is a metal cation (Ge^{2+}, Sn^{2+}, Pb^{2+}) is the most suitable for light harvesting due to the adapted band gap to solar spectra. However, this family suffers from some lead toxicity, so further enhancements and research work have to be conducted to avoid this major inconvenient. Researchers over the last decade was trying to do intensive experimental and theoretical works to overcome perovskite solar cells disadvantages.

This work was an extensive work of perovskite material-based solar cells field of research. In which we tried to carry out a software modeling and optimization of different solar cells based on three types of perovskites namely : methyl ammonium lead tri-iodide, methyl ammonium tin tri-iodide and methyl ammonium germanium tri-iodide. The choice of these materials is due to their good optical and electrical characteristics. The obtained results indicate that the lead-based perovskite is much better in term of power conversion efficiency than the tin or germanium-based perovskite. Meanwhile, $MASnI_3$ and $MAGeI_3$ are environment friendly materials which is an important characteristic for commercial production. Accordingly, simulations and optimization of both Pb-perovskite solar cell and Sn-perovskite solar cell basing on carefully selected experimental litterateur results to find out better layer thicknesses of these devices that yield high power conversion efficiency were presented and discussed in the first part. The

second part was focused on study and investigation of Ge-perovskite solar cells engineering in order to improve their performances in term of electrical and optical behavior. Then, we tried to examine the effect of electron and hole transporting materials and to find the optimal onces that enhance Ge lead free perovskite-based solar cell power conversion efficiency. It is found that Ge-perovskite solar cells using C_{60} as ETL material and $CuSBS_2$ as HTL material exhibited a high power conversion efficiency of 23.58 %. Both materials, C_{60} and $CuSBS_2$, may be considered as excellent candidates for fabricating Ge-perovskite solar cells with high efficiency and enhanced stability.

Our numerical modeling of perovskite-based solar cells provides a guidance and can be used to predict other solar cells-based devices for low nontoxic and high efficiency. However, future works can be conducted on theoretical and/or experimental parts to find out new solar cell designs such as tandem structure by inserting $MAGeI_3$, or using mixed perovskite in solar cell structure like $MAGe_xPb_{1-x}I_3$ to enhance the lead free perovskite solar cell performances, especially high power conversion efficiency and low cost processing.

BIBLIOGRAPHY

[1] Daryl M Chapin, CS Fuller, and GL Pearson. A new silicon p-n junction photocell for converting solar radiation into electrical power. *Journal of Applied Physics*, 25(5):676–677, 1954.

[2] Ashish Dubey, Nirmal Adhikari, Sally Mabrouk, Fan Wu, Ke Chen, Shangfeng Yang, and Qiquan Qiao. A strategic review on processing routes towards highly efficient perovskite solar cells. *Journal of Materials Chemistry A*, 6(6):2406–2431, 2018.

[3] Zhengqi Shi and Ahalapitiya H Jayatissa. Perovskites-based solar cells: A review of recent progress, materials and processing methods. *Materials*, 11(5):729, 2018.

[4] Disheng Yao, Chunmei Zhang, Ngoc Duy Pham, Yaohong Zhang, Vincent Tiing Tiong, Aijun Du, Qing Shen, Gregory J Wilson, and Hongxia Wang. Hindered formation of photoinactive δ-fapbi3 phase and hysteresis-free mixed-cation planar heterojunction perovskite solar cells with enhanced efficiency via potassium incorporation. *The journal of physical chemistry letters*, 9(8):2113–2120, 2018.

[5] Fan Wu, Behzad Bahrami, Ke Chen, Sally Mabrouk, Rajesh Pathak, Yanhua Tong, Xiaoyi Li, Tiansheng Zhang, Ronghua Jian, and Qiquan Qiao. Bias-dependent normal and inverted j–v hysteresis in perovskite solar cells. *ACS applied materials & interfaces*, 10(30):25604–25613, 2018.

[6] Dae-Yong Son, Seul-Gi Kim, Ja-Young Seo, Seon-Hee Lee, Hyunjung Shin, Donghwa Lee, and Nam-Gyu Park. Universal approach toward hysteresis-free perovskite solar cell via defect engineering. *Journal of the American Chemical Society*, 140(4):1358–1364, 2018.

[7] You-Hyun Seo, Eun-Chong Kim, Se-Phin Cho, Seok-Soon Kim, and Seok-In Na. Hysteresis data of planar perovskite solar cells fabricated with different solvents. *Data in brief*, 16:418–422, 2018.

[8] Samy Almosni, Ludmila Cojocaru, Debin Li, Satoshi Uchida, Takaya Kubo, and Hiroshi Segawa. Tunneling-assisted trapping as one of the possible mechanisms for the origin of hysteresis in perovskite solar cells. *Energy Technology*, 5(10):1767–1774, 2017.

[9] Jeong-Hyeok Im, Chang-Ryul Lee, Jin-Wook Lee, Sang-Won Park, and Nam-Gyu Park. 6.5% efficient perovskite quantum-dot-sensitized solar cell. *Nanoscale*, 3(10):4088–4093, 2011.

[10] Dae-Yong Son, Jeong-Hyeok Im, Hui-Seon Kim, and Nam-Gyu Park. 11% efficient perovskite solar cell based on zno nanorods: an effective charge collection system. *The Journal of Physical Chemistry C*, 118(30):16567–16573, 2014.

[11] Masood Mehrabian and Sina Dalir. 11.73% efficient perovskite heterojunction solar cell simulated by silvaco atlas software. *Optik*, 139:44–47, 2017.

[12] Hao Li, Kun Cao, Jin Cui, Shuangshuang Liu, Xianfeng Qiao, Yan Shen, and Mingkui Wang. 14.7% efficient mesoscopic perovskite solar cells using single walled carbon nanotubes/carbon composite counter electrodes. *Nanoscale*, 8(12):6379–6385, 2016.

[13] Sang Do Sung, Min Soo Kang, In Taek Choi, Hong Mo Kim, Hyoungjin Kim, MunPyo Hong, Hwan Kyu Kim, and Wan In Lee. 14.8% perovskite solar cells employing carbazole derivatives as hole transporting materials. *Chemical Communications*, 50(91):14161–14163, 2014.

[14] A Hima, N Lakhdar, and A Saadoune. Effect of electron transporting layer on power con-version efficiency of perockite-based splar cell: Comparative study. *Journal of nano- and electronic physics*, 11(1):01026–1–01026–3, 2019.

[15] Long Zhou, Jingjing Chang, Ziye Liu, Xu Sun, Zhenhua Lin, Dazheng Chen, Chunfu Zhang, Jincheng Zhang, and Yue Hao. Enhanced planar perovskite solar cell efficiency and stability using a perovskite/pcbm heterojunction formed in one step. *Nanoscale*, 10(6):3053–3059, 2018.

[16] Ming Yang, Nana Wang, Shuting Zhang, Wei Zou, Yarong He, Yingqiang Wei, Mengmeng Xu, Jianpu Wang, and Wei Huang. Reduced efficiency roll-off and enhanced stability in perovskite light-emitting diodes with multiple quantum wells. *The journal of physical chemistry letters*, 9(8):2038–2042, 2018.

[17] Ikuya Yamada, Akihiko Takamatsu, and Hidekazu Ikeno. Complementary evaluation of structure stability of perovskite oxides using bond-valence and density-functional-theory calculations. *Science and Technology of advanced MaTerialS*, 19(1):101–107, 2018.

[18] Xiaojun Qin, Zhiguo Zhao, Yidan Wang, Junbo Wu, Qi Jiang, and Jingbi You. Recent progress in stability of perovskite solar cells. *Journal of Semiconductors*, 38(1):011002, 2017.

[19] Akihiro Kojima, Kenjiro Teshima, Yasuo Shirai, and Tsutomu Miyasaka. Organometal halide perovskites as visible-light sensitizers for photovoltaic cells. *Journal of the American Chemical Society*, 131(17):6050–6051, 2009.

[20] Michael Saliba, Taisuke Matsui, Ji-Youn Seo, Konrad Domanski, Juan-Pablo Correa-Baena, Mohammad Khaja Nazeeruddin, Shaik M Zakeeruddin, Wolfgang Tress, Antonio Abate, and Anders Hagfeldt. Cesium-containing triple cation perovskite solar cells: improved stability, reproducibility and high efficiency. *Energy & environmental science*, 9(6):1989–1997, 2016.

[21] NREL. Best research-cell efficiency chart. https://www.nrel.gov/pv/cell-efficiency.html. Accessed on 2019-06-08.

[22] Martin A Green, Ewan D Dunlop, Dean H Levi, Jochen Hohl-Ebinger, Masahiro Yoshita, and Anita WY Ho-Baillie. Solar cell efficiency tables (version 54). *Progress in Photovoltaics: Research and Applications*, 27(7):565–575, 2019.

[23] James E Bishop, Thomas J Routledge, and David G Lidzey. Advances in spray-cast perovskite solar cells. *The journal of physical chemistry letters*, 9(8):1977–1984, 2018.

[24] Xiao Du, Yan Wang, Zhong Gao Xia, and Hang Zhou. Perovskite ch3nh3pbi3 heterojunction solar cells via ultrasonic spray deposition. In *Applied Mechanics and Materials*, volume 748, pages 39–43. Trans Tech Publ, 2015.

[25] I. Kemerchou, F. Rogti, B. Benhaoua, N. Lakhdar, A. Hima, O. Benhaoua, and A. Khechekhouche. Processing temperature effect on optical and morphological parameters of organic perovskite ch3nh3pbi3 prepared using spray pyrolysis method. *JOURNAL OF NANO- AND ELECTRONIC PHYSICS*, 11(3):03011 (4), 2019.

[26] Yonghui Lee, Seunghwan Lee, Gabseok Seo, Sanghyun Paek, Kyung Taek Cho, Aron J Huckaba, Marco Calizzi, Dong-won Choi, Jin-Seong Park, Dongwook Lee, et al. Efficient planar perovskite solar cells using passivated tin oxide as an electron transport layer. *Advanced Science*, 5(6):1800130, 2018.

[27] Khalid Mahmood, Saad Sarwar, and Muhammad Taqi Mehran. Current status of electron transport layers in perovskite solar cells: materials and properties. *RSC advances*, 7(28):17044–17062, 2017.

[28] Aaesha Alnuaimi, Ibraheem Almansouri, and Ammar Nayfeh. Effect of mobility and band structure of hole transport layer in planar heterojunction perovskite solar cells using 2d tcad simulation. *Journal of Computational Electronics*, 15(3):1110–1118, 2016.

[29] Zinab H Bakr, Qamar Wali, Azhar Fakharuddin, Lukas Schmidt-Mende, Thomas M Brown, and Rajan Jose. Advances in hole transport materials engineering for stable and efficient perovskite solar cells. *Nano Energy*, 34:271–305, 2017.

[30] Lei Lei, Shude Zhang, Songwang Yang, Xiaomin Li, Yu Yu, Qingzhu Wei, Zhichun Ni, and Ming Li. Influence of hole transport material/metal contact interface on perovskite solar cells. *Nanotechnology*, 29(25):255201, 2018.

[31] Ilario Gelmetti, Lydia Cabau, Núria F Montcada, and Emilio Palomares. Selective organic contacts for methyl ammonium lead iodide (mapi) perovskite solar cells: influence of layer thickness on carriers extraction and carriers lifetime. *ACS applied materials & interfaces*, 9(26):21599–21605, 2017.

[32] Ananth Saradhi and BVVSN Prabhakara Rao. Comparison of performance in p3ht: Pcbm bulk heterojunction organic solar cells of different thickness. In *2014 IEEE International Conference on Electronics, Computing and Communication Technologies (CONECCT)*, pages 1–3. IEEE, 2014.

[33] Aditi Toshniwal, Akshay Jariwala, Vipul Kheraj, AS Opanasyuk, and CJ Panchal. Numerical simulation of tin based perovskite solar cell: effects of absorber parameters and hole transport materials. *Journal of Nano-and Electronic Physics*, 9(3), 2017.

[34] Usha Mandadapu, S Victor Vedanayakam, and K Thyagarajan. Simulation and analysis of lead based perovskite solar cell using scaps-1d. *Indian Journal of Science and Technology*, 10(11):65–72, 2017.

[35] Noor Fadhilah Ramli, Suhaila Sepeai, Nur Fairuz Mohd Rostan, Norasikin Ahmad Ludin, Mohd Adib Ibrahim, Mohd Asri Mat Teridi, and Salem H Zaidi. Model development of monolithic tandem silicon-perovskite solar cell by scaps simulation. In *AIP Conference Proceedings*, volume 1838, page 020006. AIP Publishing LLC, 2017.

[36] AM Elseman, Jun Ji, Shangyi Dou, Hao Huang, Peng Cui, Dong Wei, and Meicheng Li. Novel hole transport layer of nickel oxide composite with carbon for high-performance perovskite solar cells. *Chinese Physics B*, 27(1):017305, 2018.

[37] A Hima, A Khechekhouche, I Kemerchou, N Lakhdar, B Benhaoua, F Rogti, I Telli, and A Saadoun. Gpvdm simulation of layer thickness effect on power conversion efficiency of ch3nh3pbi3 based planar heterojunction solar cell. *International Journal of Energetica*, 4(1):56–59, 2019.

[38] Int Silvaco. *ATLAS user's manual*. Santa Clara, CA, 2018.

[39] Klaus-Dieter Jäger, Olindo Isabella, Arno HM Smets, René ACMM van Swaaij, and Miro Zeman. *Solar Energy: Fundamentals, Technology and Systems*. UIT Cambridge, 2016.

[40] Tetsuo Soga. Fundamentals of solar cell. In *Nanostructured Materials for Solar Energy Conversion*, pages 3–43. Elsevier, 2006.

[41] WTRW Shockley and WT Read Jr. Statistics of the recombinations of holes and electrons. *Physical review*, 87(5):835, 1952.

[42] Re N Hall. Electron-hole recombination in germanium. *Physical review*, 87(2):387, 1952.

[43] Siegfried Selberherr. *Analysis and simulation of semiconductor devices*. Springer Science & Business Media, 2012.

[44] Andrew S Grove. *Physics and technology of semiconductor devices*. Wiley, 1967.

[45] GAM Hurkx, DBM Klaassen, and MPG Knuvers. A new recombination model for device simulation including tunneling. *IEEE Transactions on electron devices*, 39(2):331–338, 1992.

[46] GAM Hurkx, DBM Klaassen, MPG Knuvers, and FG O'hara. A new recombination model describing heavy-doping effects and low-temperature behaviour. In *International Technical Digest on Electron Devices Meeting*, pages 307–310. IEEE, 1989.

[47] GAM Hurkx, HC De Graaff, WJ Kloosterman, and MPG Knuvers. A novel compact model description of reverse-biased diode characteristics including tunnelling. In *ESSDERC'90: 20th European Solid State Device Research Conference*, pages 49–52. IEEE, 1990.

[48] Miro Zeman. Introduction to photovoltaic solar energy. *Delft University of Technology*, 2(6), 2003.

[49] Ashwith Kumar Chilvery, Ashok K Batra, Bin Yang, Kai Xiao, Padmaja Guggilla, Mohan D Aggarwal, Raja Surabhi, Ravi B Lal, James R Currie, and Benjamin G Penn. Perovskites: transforming photovoltaics, a mini-review. *Journal of Photonics for Energy*, 5(1):057402, 2015.

[50] Roger H Mitchell, Mark D Welch, and Anton R Chakhmouradian. Nomenclature of the perovskite supergroup: A hierarchical system of classification based on crystal structure and composition. *Mineralogical Magazine*, 81(3):411–462, 2017.

[51] A Kojima, K Teshima, T Miyasaka, and Y Shirai. Novel photoelectrochemical cell with mesoscopic electrodes sensitized by lead-halide compounds (2) 210th ecs meeting, cancun, mexico. *October Abstract*, 397:397397, 2006.

[52] Woon Seok Yang, Jun Hong Noh, Nam Joong Jeon, Young Chan Kim, Seungchan Ryu, Jangwon Seo, and Sang Il Seok. High-performance photovoltaic perovskite layers fabricated through intramolecular exchange. *Science*, 348(6240):1234–1237, 2015.

[53] Di Zhou, Tiantian Zhou, Yu Tian, Xiaolong Zhu, and Yafang Tu. Perovskite-based solar cells: materials, methods, and future perspectives. *Journal of Nanomaterials*, 2018, 2018.

[54] Jiachen Zhou and Jia Huang. Photodetectors based on organic–inorganic hybrid lead halide perovskites. *Advanced Science*, 5(1):1700256, 2018.

[55] Jingyu Qian, Bin Xu, and Wenjing Tian. A comprehensive theoretical study of halide perovskites abx3. *Organic Electronics*, 37:61–73, 2016.

[56] Qiaoling Xu, Dongwen Yang, Jian Lv, Yi-Yang Sun, and Lijun Zhang. Perovskite solar absorbers: materials by design. *Small Methods*, 2(5):1700316, 2018.

[57] Maria Konstantakou and Thomas Stergiopoulos. A critical review on tin halide perovskite solar cells. *Journal of Materials Chemistry A*, 5(23):11518–11549, 2017.

[58] Ahmad Esmail Shalan, Samrana Kazim, and Shahzada Ahmad. Lead free perovskite materials: Interplay of metals substitution for environmentally compatible solar cells fabrication. *ChemSusChem*, 2019.

[59] Taofeeq Ibn-Mohammed, SCL Koh, IM Reaney, Adolf Acquaye, G Schileo, KB Mustapha, and Rick Greenough. Perovskite solar cells: An integrated hybrid lifecycle assessment and review in comparison with other photovoltaic technologies. *Renewable and Sustainable Energy Reviews*, 80:1321–1344, 2017.

[60] Junfeng Yan and Brian R Saunders. Third-generation solar cells: a review and comparison of polymer: fullerene, hybrid polymer and perovskite solar cells. *Rsc Advances*, 4(82):43286–43314, 2014.

[61] Shuangyong Sun, Teddy Salim, Nripan Mathews, Martial Duchamp, Chris Boothroyd, Guichuan Xing, Tze Chien Sum, and Yeng Ming Lam. The origin of high efficiency in low-temperature solution-processable bilayer organometal halide hybrid solar cells. *Energy & Environmental Science*, 7(1):399–407, 2014.

[62] Constantinos C Stoumpos, Christos D Malliakas, and Mercouri G Kanatzidis. Semiconducting tin and lead iodide perovskites with organic cations: phase transitions, high mobilities, and near-infrared photoluminescent properties. *Inorganic chemistry*, 52(15):9019–9038, 2013.

[63] Tom Baikie, Yanan Fang, Jeannette M Kadro, Martin Schreyer, Fengxia Wei, Subodh G Mhaisalkar, Michael Graetzel, and Tim J White. Synthesis and crystal chemistry of the hybrid perovskite (ch 3 nh 3) pbi 3 for solid-state sensitised solar cell applications. *Journal of Materials Chemistry A*, 1(18):5628–5641, 2013.

[64] Martin A Green, Anita Ho-Baillie, and Henry J Snaith. The emergence of perovskite solar cells. *Nature photonics*, 8(7):506, 2014.

[65] Surya Prakash Singh and P Nagarjuna. Organometal halide perovskites as useful materials in sensitized solar cells. *Dalton Transactions*, 43(14):5247–5251, 2014.

[66] Mengyu Luan, Junling Song, Xiangfeng Wei, Fang Chen, and Jiehua Liu. Controllable growth of bulk cubic-phase ch 3 nh 3 pbi 3 single crystal with exciting room-temperature stability. *CrystEngComm*, 18(28):5257–5261, 2016.

[67] Byunghong Lee, Jiaqing He, Robert PH Chang, and Mercouri G Kanatzidis. All-solid-state dye-sensitized solar cells with high efficiency. *Nature*, 485(7399):486, 2012.

[68] AB Djurišić, FZ Liu, HW Tam, MK Wong, A Ng, Chen Surya, W Chen, and ZB He. Perovskite solar cells-an overview of critical issues. *Progress in Quantum Electronics*, 53:1–37, 2017.

[69] Hui-Seon Kim, Jin-Wook Lee, Natalia Yantara, Pablo P Boix, Sneha A Kulkarni, Subodh Mhaisalkar, Michael Grätzel, and Nam-Gyu Park. High efficiency solid-state sensitized solar cell-based on submicrometer rutile tio2 nanorod and ch3nh3pbi3 perovskite sensitizer. *Nano letters*, 13(6):2412–2417, 2013.

[70] Stefaan De Wolf, Jakub Holovsky, Soo-Jin Moon, Philipp Löper, Bjoern Niesen, Martin Ledinsky, Franz-Josef Haug, Jun-Ho Yum, and Christophe Ballif. Organometallic halide perovskites: sharp optical absorption edge and its relation to photovoltaic performance. *The journal of physical chemistry letters*, 5(6):1035–1039, 2014.

[71] Patrick Tonui, Saheed O Oseni, Gaurav Sharma, Qingfenq Yan, and Genene Tessema Mola. Perovskites photovoltaic solar cells: An overview of current status. *Renewable and Sustainable Energy Reviews*, 91:1025–1044, 2018.

[72] Jun Hong Noh, Sang Hyuk Im, Jin Hyuck Heo, Tarak N Mandal, and Sang Il Seok. Chemical management for colorful, efficient, and stable inorganic–organic hybrid nanostructured solar cells. *Nano letters*, 13(4):1764–1769, 2013.

[73] Wei Peng, Lingfei Wang, Banavoth Murali, Kang-Ting Ho, Ashok Bera, Namchul Cho, Chen-Fang Kang, Victor M Burlakov, Jun Pan, Lutfan Sinatra, et al. Solution-grown monocrystalline hybrid perovskite films for hole-transporter-free solar cells. *Advanced Materials*, 28(17):3383–3390, 2016.

[74] Nam-Gyu Park. Organometal perovskite light absorbers toward a 20% efficiency low-cost solid-state mesoscopic solar cell. *The Journal of Physical Chemistry Letters*, 4(15):2423–2429, 2013.

[75] Makhsud I Saidaminov, Ahmed L Abdelhady, Banavoth Murali, Erkki Alarousu, Victor M Burlakov, Wei Peng, Ibrahim Dursun, Lingfei Wang, Yao He, Giacomo Maculan, et al. High-quality bulk hybrid perovskite single crystals within minutes by inverse temperature crystallization. *Nature communications*, 6:7586, 2015.

[76] Qing-Dong Ou, Chi Li, Qian-Kun Wang, Yan-Qing Li, and Jian-Xin Tang. Recent advances in energetics of metal halide perovskite interfaces. *Advanced Materials Interfaces*, 4(2):1600694, 2017.

[77] Michiel L Petrus, Johannes Schlipf, Cheng Li, Tanaji P Gujar, Nadja Giesbrecht, Peter Müller-Buschbaum, Mukundan Thelakkat, Thomas Bein, Sven Hüttner, and Pablo Docampo. Capturing the sun: A review of the challenges and perspectives of perovskite solar cells. *Advanced Energy Materials*, 7(16):1700264, 2017.

[78] Istiak Hussain, Hoang Phong Tran, Jared Jaksik, Justin Moore, Nazmul Islam, and M Jasim Uddin. Functional materials, device architecture, and flexibility of perovskite solar cell. *Emergent Materials*, 1(3-4):133–154, 2018.

[79] Henry J Snaith, Antonio Abate, James M Ball, Giles E Eperon, Tomas Leijtens, Nakita K Noel, Samuel D Stranks, Jacob Tse-Wei Wang, Konrad Wojciechowski, and Wei Zhang. Anomalous hysteresis in perovskite solar cells. *J. Phys. Chem. Lett*, 5(9):1511–1515, 2014.

[80] Chi Li, Jian Wei, Mikio Sato, Harunobu Koike, Zhong-Zhi Xie, Yan-Qing Li, Kaname Kanai, Satoshi Kera, Nobuo Ueno, and Jian-Xin Tang. Halide-substituted electronic properties of organometal halide perovskite films: direct and inverse photoemission studies. *ACS applied materials & interfaces*, 8(18):11526–11531, 2016.

[81] Paolo Umari, Edoardo Mosconi, and Filippo De Angelis. Relativistic gw calculations on ch 3 nh 3 pbi 3 and ch 3 nh 3 sni 3 perovskites for solar cell applications. *Scientific reports*, 4:4467, 2014.

[82] Faisal Baig, Yousaf Hameed Khattak, Bernabé Marí, Saira Beg, Abrar Ahmed, and Khurram Khan. Efficiency enhancement of ch 3 nh 3 sni 3 solar cells by device modeling. *Journal of Electronic Materials*, 47(9):5275–5282, 2018.

[83] Constantinos C Stoumpos, Laszlo Frazer, Daniel J Clark, Yong Soo Kim, Sonny H Rhim, Arthur J Freeman, John B Ketterson, Joon I Jang, and Mercouri G Kanatzidis. Hybrid germanium iodide perovskite semiconductors: active lone pairs, structural distortions, direct and indirect energy gaps, and strong nonlinear optical properties. *Journal of the American Chemical Society*, 137(21):6804–6819, 2015.

[84] Thirumal Krishnamoorthy, Hong Ding, Chen Yan, Wei Lin Leong, Tom Baikie, Ziyi Zhang, Matthew Sherburne, Shuzhou Li, Mark Asta, Nripan Mathews, et al. Lead-free germanium iodide perovskite materials for photovoltaic applications. *Journal of Materials Chemistry A*, 3(47):23829–23832, 2015.

[85] Wenmei Ming, Hongliang Shi, and Mao-Hua Du. Large dielectric constant, high acceptor density, and deep electron traps in perovskite solar cell material csgei 3. *Journal of Materials Chemistry A*, 4(36):13852–13858, 2016.

[86] Carlito S Ponseca Jr, Tom J Savenije, Mohamed Abdellah, Kaibo Zheng, Arkady Yartsev, Tobjoörn Pascher, Tobias Harlang, Pavel Chabera, Tonu Pullerits, Andrey Stepanov, et al. Organometal halide perovskite solar cell materials rationalized: ultrafast charge generation, high and microsecond-long balanced mobilities, and slow recombination. *Journal of the American Chemical Society*, 136(14):5189–5192, 2014.

[87] Zhaoning Song, Suneth C Watthage, Adam B Phillips, and Michael J Heben. Pathways toward high-performance perovskite solar cells: review of recent advances in organo-metal halide perovskites for photovoltaic applications. *Journal of Photonics for Energy*, 6(2):022001, 2016.

[88] Zhongmin Zhou, Shuping Pang, Zhihong Liu, Hongxia Xu, and Guanglei Cui. Interface engineering for high-performance perovskite hybrid solar cells. *Journal of Materials Chemistry A*, 3(38):19205–19217, 2015.

[89] Chuantian Zuo, Henk J Bolink, Hongwei Han, Jinsong Huang, David Cahen, and Liming Ding. Advances in perovskite solar cells. *Advanced Science*, 3(7):1500324, 2016.

[90] Ming-Hsien Li, Po-Shen Shen, Kuo-Chin Wang, Tzung-Fang Guo, and Peter Chen. Inorganic p-type contact materials for perovskite-based solar cells. *Journal of Materials Chemistry A*, 3(17):9011–9019, 2015.

[91] Teddy Salim, Shuangyong Sun, Yuichiro Abe, Anurag Krishna, Andrew C Grimsdale, and Yeng Ming Lam. Perovskite-based solar cells: impact of morphology and device architecture on device performance. *Journal of Materials Chemistry A*, 3(17):8943–8969, 2015.

[92] Huanping Zhou, Qi Chen, Gang Li, Song Luo, Tze-bing Song, Hsin-Sheng Duan, Ziruo Hong, Jingbi You, Yongsheng Liu, and Yang Yang. Interface engineering of highly efficient perovskite solar cells. *Science*, 345(6196):542–546, 2014.

[93] Jun-Yuan Jeng, Yi-Fang Chiang, Mu-Huan Lee, Shin-Rung Peng, Tzung-Fang Guo, Peter Chen, and Ten-Chin Wen. Ch3nh3pbi3 perovskite/-fullerene planar-heterojunction hybrid solar cells. *Advanced Materials*, 25(27):3727–3732, 2013.

[94] Lijun Hu, Kuan Sun, Ming Wang, Wei Chen, Bo Yang, Jiehao Fu, Zhuang Xiong, Xinyi Li, Xiaosheng Tang, Zhigang Zang, et al. Inverted planar perovskite solar cells with a high fill factor and negligible hysteresis by the dual effect of nacl-doped pedot: Pss. *ACS applied materials & interfaces*, 9(50):43902–43909, 2017.

[95] Hui-Seon Kim, In-Hyuk Jang, Namyoung Ahn, Mansoo Choi, Antonio Guerrero, Juan Bisquert, and Nam-Gyu Park. Control of i–v hysteresis in ch3nh3pbi3 perovskite solar cell. *The journal of physical chemistry letters*, 6(22):4633–4639, 2015.

[96] Weijun Ke, Guojia Fang, Qin Liu, Liangbin Xiong, Pingli Qin, Hong Tao, Jing Wang, Hongwei Lei, Borui Li, Jiawei Wan, et al. Low-temperature solution-processed tin oxide as an alternative electron transporting layer for efficient perovskite solar cells. *Journal of the American Chemical Society*, 137(21):6730–6733, 2015.

[97] Tianshi Qin, Wenchao Huang, Jueng-Eun Kim, Doojin Vak, Craig Forsyth, Christopher R McNeill, and Yi-Bing Cheng. Amorphous hole-transporting layer in slot-die coated perovskite solar cells. *Nano Energy*, 31:210–217, 2017.

[98] Minchao Qin, Junjie Ma, Weijun Ke, Pingli Qin, Hongwei Lei, Hong Tao, Xiaolu Zheng, Liangbin Xiong, Qin Liu, Zhiliang Chen, et al. Perovskite solar cells based on low-temperature processed indium oxide electron selective layers. *ACS applied materials & interfaces*, 8(13):8460–8466, 2016.

[99] Aswani Yella, Leo-Philipp Heiniger, Peng Gao, Mohammad Khaja Nazeeruddin, and Michael Grätzel. Nanocrystalline rutile electron extraction layer enables low-temperature solution processed perovskite photovoltaics with 13.7% efficiency. *Nano letters*, 14(5):2591–2596, 2014.

[100] Chen Tao, Stefanie Neutzner, Letizia Colella, Sergio Marras, Ajay Ram Srimath Kandada, Marina Gandini, Michele De Bastiani, Giuseppina Pace, Liberato Manna, Mario Caironi, et al. 17.6% stabilized efficiency in low-temperature processed planar perovskite solar cells. *Energy & Environmental Science*, 8(8):2365–2370, 2015.

[101] Qifeng Zhang, Christopher S Dandeneau, Xiaoyuan Zhou, and Guozhong Cao. Zno nanostructures for dye-sensitized solar cells. *Advanced Materials*, 21(41):4087–4108, 2009.

[102] Kai Wang, Yantao Shi, Qingshun Dong, Yu Li, Shufeng Wang, Xufeng Yu, Mengyao Wu, and Tingli Ma. Low-temperature and solution-processed amorphous wo x as electron-selective layer for perovskite solar cells. *The journal of physical chemistry letters*, 6(5):755–759, 2015.

[103] Xin Wang, Lin-Long Deng, Lu-Yao Wang, Si-Min Dai, Zhou Xing, Xin-Xing Zhan, Xu-Zhai Lu, Su-Yuan Xie, Rong-Bin Huang, and Lan-Sun Zheng. Cerium oxide standing out as an electron transport layer for efficient and stable perovskite solar cells processed at low temperature. *Journal of Materials Chemistry A*, 5(4):1706–1712, 2017.

[104] Olga Malinkiewicz, Aswani Yella, Yong Hui Lee, Guillermo Mínguez Espallargas, Michael Graetzel, Mohammad K Nazeeruddin, and Henk J Bolink. Perovskite solar cells employing organic charge-transport layers. *Nature Photonics*, 8(2):128, 2014.

[105] Qi Wang, Yuchuan Shao, Qingfeng Dong, Zhengguo Xiao, Yongbo Yuan, and Jinsong Huang. Large fill-factor bilayer iodine perovskite solar cells fabricated by a low-temperature solution-process. *Energy & Environmental Science*, 7(7):2359–2365, 2014.

[106] Yixin Zhao and Kai Zhu. Organic–inorganic hybrid lead halide perovskites for optoelectronic and electronic applications. *Chemical Society Reviews*, 45(3):655–689, 2016.

[107] He Xi, Shi Tang, Xiaohua Ma, Jingjing Chang, Dazheng Chen, Zhenhua Lin, Peng Zhong, Hong Wang, and Chunfu Zhang. Performance enhancement of planar heterojunction perovskite solar cells through tuning the doping properties of hole-transporting materials. *Acs Omega*, 2(1):326–336, 2017.

[108] Jin Hyuck Heo, Sang Hyuk Im, Jun Hong Noh, Tarak N Mandal, Choong-Sun Lim, Jeong Ah Chang, Yong Hui Lee, Hi-jung Kim, Arpita Sarkar, Md K Nazeeruddin, et al. Efficient inorganic–organic hybrid heterojunction solar cells containing perovskite compound and polymeric hole conductors. *Nature photonics*, 7(6):486, 2013.

[109] Dongqin Bi, Lei Yang, Gerrit Boschloo, Anders Hagfeldt, and Erik MJ Johansson. Effect of different hole transport materials on recombination in ch3nh3pbi3 perovskite-sensitized mesoscopic solar cells. *The journal of physical chemistry letters*, 4(9):1532–1536, 2013.

[110] Hisham A Abbas, Ranjith Kottokkaran, Balaji Ganapathy, Mehran Samiee, Liang Zhang, Andrew Kitahara, Max Noack, and Vikram L Dalal. High efficiency sequentially vapor grown nip ch3nh3pbi3 perovskite solar cells with undoped p3ht as p-type heterojunction layer. *APL materials*, 3(1):016105, 2015.

[111] Bert Conings, Linny Baeten, Christopher De Dobbelaere, Jan D'Haen, Jean Manca, and Hans-Gerd Boyen. Perovskite-based hybrid solar cells exceeding 10% efficiency with high reproducibility using a thin film sandwich approach. *Advanced Materials*, 26(13):2041–2046, 2014.

[112] Yaoming Xiao, Gaoyi Han, Yunzhen Chang, Haihan Zhou, Miaoyu Li, and Yanping Li. An all-solid-state perovskite-sensitized solar cell based on the dual function polyaniline as the sensitizer and p-type hole-transporting material. *Journal of Power Sources*, 267:1–8, 2014.

[113] Wanyi Nie, Hsinhan Tsai, Reza Asadpour, Jean-Christophe Blancon, Amanda J Neukirch, Gautam Gupta, Jared J Crochet, Manish Chhowalla, Sergei Tretiak, Muhammad A Alam, et al. High-efficiency solution-processed perovskite solar cells with millimeter-scale grains. *Science*, 347(6221):522–525, 2015.

[114] Haoxin Wang, Ze Yu, Xiao Jiang, Jiajia Li, Bin Cai, Xichuan Yang, and Licheng Sun. Efficient and stable inverted planar perovskite solar cells employing cui as hole-transporting layer prepared by solid–gas transformation. *Energy Technology*, 5(10):1836–1843, 2017.

[115] Stefan Weber, Thomas Rath, Jimmy Mangalam, Birgit Kunert, Anna Maria Coclite, Martin Bauch, Theodoros Dimopoulos, and Gregor Trimmel. Investigation of nio x-hole transport layers in triple cation perovskite solar cells. *Journal of Materials Science: Materials in Electronics*, 29(3):1847–1855, 2018.

[116] Nilushi Wijeyasinghe, Anna Regoutz, Flurin Eisner, Tian Du, Leonidas Tsetseris, Yen-Hung Lin, Hendrik Faber, Pichaya Pattanasattayavong, Jinhua Li, Feng Yan, et al. Copper (i) thiocyanate (cuscn) hole-transport layers processed from aqueous precursor solutions and their application in thin-film transistors and highly efficient organic and organometal halide perovskite solar cells. *Advanced Functional Materials*, 27(35):1701818, 2017.

[117] Jeffrey A Christians, Raymond CM Fung, and Prashant V Kamat. An inorganic hole conductor for organo-lead halide perovskite solar cells. improved hole conductivity with copper iodide. *Journal of the American Chemical Society*, 136(2):758–764, 2013.

[118] Peng Qin, Soichiro Tanaka, Seigo Ito, Nicolas Tetreault, Kyohei Manabe, Hitoshi Nishino, Mohammad Khaja Nazeeruddin, and Michael Grätzel. Inorganic hole conductor-based lead halide perovskite solar cells with 12.4% conversion efficiency. *Nature communications*, 5:3834, 2014.

[119] Kuo-Chin Wang, Po-Shen Shen, Ming-Hsien Li, Shi Chen, Ming-Wei Lin, Peter Chen, and Tzung-Fang Guo. Low-temperature sputtered nickel oxide compact thin film as effective electron blocking layer for mesoscopic nio/ch3nh3pbi3 perovskite heterojunction solar cells. *ACS applied materials & interfaces*, 6(15):11851–11858, 2014.

[120] Marc Burgelman. *SCAPS manual*. University of Gent, Belgium, 2019.

[121] Abdelkader Hima, Nacereddine Lakhdar, Benhaoua Boubaker, Saadoun Achour, Kemerchou Imad, and Rogti Fatiha. An optimized perovskite solar cell designs for high conversion efficiency. *Superlattices and Microstructures*, 129:240–246, 2019.

[122] Philip Calado, Andrew M Telford, Daniel Bryant, Xiaoe Li, Jenny Nelson, Brian C O'Regan, and Piers RF Barnes. Evidence for ion migration in hybrid perovskite solar cells with minimal hysteresis. *Nature communications*, 7(1):1–10, 2016.

[123] Kenichi Ozawa, Susumu Yamamoto, Ryu Yukawa, Roya Liu, Masato Emori, Koki Inoue, Taku Higuchi, Hiroshi Sakama, Kazuhiko Mase, and Iwao Matsuda. What determines the lifetime of photoexcited carriers on tio2 surfaces? *The Journal of Physical Chemistry C*, 120(51):29283–29289, 2016.

[124] Stephan van Reenen, Martijn Kemerink, and Henry J Snaith. Modeling anomalous hysteresis in perovskite solar cells. *The journal of physical chemistry letters*, 6(19):3808–3814, 2015.

[125] Antonio Guerrero, Germa Garcia-Belmonte, Ivan Mora-Sero, Juan Bisquert, Yong Soo Kang, T Jesper Jacobsson, Juan-Pablo Correa-Baena, and Anders Hagfeldt. Properties of contact and bulk impedances in hybrid lead halide perovskite solar cells including inductive loop elements. *The Journal of Physical Chemistry C*, 120(15):8023–8032, 2016.

[126] Sandheep Ravishankar, Osbel Almora, Carlos Echeverría-Arrondo, Elnaz Ghahremanirad, Clara Aranda, Antonio Guerrero, Francisco Fabregat-Santiago, Arie Zaban, Germa Garcia-Belmonte, and Juan Bisquert. Surface polarization model for the dynamic hysteresis of perovskite solar cells. *The journal of physical chemistry letters*, 8(5):915–921, 2017.

[127] Qianqian Lin, Ardalan Armin, Ravi Chandra Raju Nagiri, Paul L Burn, and Paul Meredith. Electro-optics of perovskite solar cells. *Nature Photonics*, 9(2):106, 2015.

[128] Xiangye Liu, Wei Zhao, Houlei Cui, Yaoming Wang, Tao Xu, Fuqiang Huang, et al. Organic–inorganic halide perovskite based solar cells–revolutionary progress in photovoltaics. *Inorganic Chemistry Frontiers*, 2(4):315–335, 2015.

[129] Nakita K Noel, Samuel D Stranks, Antonio Abate, Christian Wehrenfennig, Simone Guarnera, Amir-Abbas Haghighirad, Aditya Sadhanala, Giles E Eperon, Sandeep K Pathak, and Michael B Johnston. Lead-free organic–inorganic tin halide perovskites for photovoltaic applications. *Energy & Environmental Science*, 7(9):3061–3068, 2014.

[130] Bert Conings, Jeroen Drijkoningen, Nicolas Gauquelin, Aslihan Babayigit, Jan D'Haen, Lien D'Olieslaeger, Anitha Ethirajan, Jo Verbeeck, Jean Manca, and Edoardo Mosconi. Intrinsic thermal instability of methylammonium lead trihalide perovskite. *Advanced Energy Materials*, 5(15):1500477, 2015.

[131] Ping-Ping Sun, Quan-Song Li, Li-Na Yang, and Ze-Sheng Li. Theoretical insights into a potential lead-free hybrid perovskite: substituting pb 2+ with ge 2+. *Nanoscale*, 8(3):1503–1512, 2016.

[132] Qiong Wang, Nga Phung, Diego Di Girolamo, Paola Vivo, and Antonio Abate. Enhancement in lifespan of halide perovskite solar cells. *Energy & Environmental Science*, 12(3):865–886, 2019.

[133] Rui Wang, Muhammad Mujahid, Yu Duan, Zhao-Kui Wang, Jingjing Xue, and Yang Yang. A review of perovskites solar cell stability. *Advanced Functional Materials*, 29(47):1808843, 2019.

[134] Zonglong Zhu, Yang Bai, Xiao Liu, Chu-Chen Chueh, Shihe Yang, and Alex K-Y Jen. Enhanced efficiency and stability of inverted perovskite solar cells using highly crystalline sno2 nanocrystals as the robust electron-transporting layer. *Advanced Materials*, 28(30):6478–6484, 2016.

[135] Kai Tan, Peng Lin, Gang Wang, Yan Liu, Zongchang Xu, and Yixin Lin. Controllable design of solid-state perovskite solar cells by scaps device simulation. *Solid-State Electronics*, 126:75–80, 2016.

[136] Yu-Qing Zhao, Biao Liu, Zhuo-Liang Yu, JianMin Ma, Qiang Wan, Peng-bin He, and Meng-Qiu Cai. Strong ferroelectric polarization of ch 3 nh 3 gei 3 with high-absorption and mobility transport anisotropy: theoretical study. *Journal of Materials Chemistry C*, 5(22):5356–5364, 2017.

[137] Qing-Yuan Chen, Yang Huang, Peng-Ru Huang, Tai Ma, Chao Cao, and Yao He. Electronegativity explanation on the efficiency-enhancing mechanism of the hybrid inorganic–organic perovskite abx3 from first-principles study. *Chinese Physics B*, 25(2):027104, 2015.

[138] Lijian Zuo, Zhuowei Gu, Tao Ye, Weifei Fu, Gang Wu, Hanying Li, and Hongzheng Chen. Enhanced photovoltaic performance of ch3nh3pbi3 perovskite solar cells through interfacial engineering using self-assembling monolayer. *Journal of the American Chemical Society*, 137(7):2674–2679, 2015.

[139] Aurélien MA Leguy, Yinghong Hu, Mariano Campoy-Quiles, M Isabel Alonso, Oliver J Weber, Pooya Azarhoosh, Mark Van Schilfgaarde, Mark T Weller, Thomas Bein, and Jenny Nelson. Reversible hydration of ch3nh3pbi3 in films, single crystals, and solar cells. *Chemistry of Materials*, 27(9):3397–3407, 2015.

[140] F Azri, M Labed, AF Meftah, N Sengouga, and AM Meftah. Optical characterization of a-igzo thin film for simulation of a-igzo (n)/µ-si (p) heterojunction solar cell. *Optical and Quantum Electronics*, 48(8):391, 2016.

[141] Takashi Minemoto and Masashi Murata. Impact of work function of back contact of perovskite solar cells without hole transport material analyzed by device simulation. *Current Applied Physics*, 14(11):1428–1433, 2014.

[142] Rahul Pandey and Rishu Chaujar. Numerical simulations: toward the design of 27.6four-terminal semi-transparent perovskite/sic passivated rear contact silicon tandem solar cell. *Superlattices and Microstructures*, 100:656–666, 2016.

[143] Yan Wang, Zhonggao Xia, Jun Liang, Xinwei Wang, Yiming Liu, Chuan Liu, Shengdong Zhang, and Hang Zhou. Towards printed perovskite solar cells with cuprous oxide hole transporting layers: a theoretical design. *Semiconductor Science and Technology*, 30(5):054004, 2015.

[144] Nikhil T Satyala, Wudyalew T Wondmagegn, Ron J Pieper, and Michael R Korn. Simulation of copper phthalocyanine/fullerene heterojunction photovoltaic cell with and without electron transport layer (etl). In *Materials Research Society Symposium*, volume 1212. Materials Research Society, 2011.

[145] W Abdelaziz, A Shaker, M Abouelatta, and A Zekry. Possible efficiency boosting of non-fullerene acceptor solar cell using device simulation. *Optical Materials*, 91:239–245, 2019.

[146] Nacereddine Lakhdar and Abdelkader Hima. Electron transport material effect on performance of perovskite solar cells based on ch3nh3gei3. *Optical Materials*, 99:109517, 2020.

[147] Ahmed-Ali Kanoun, Mohammed Benali Kanoun, Abdelkrim E Merad, and Souraya Goumri-Said. Toward development of high-performance perovskite solar cells based on ch3nh3gei3 using computational approach. *Solar Energy*, 182:237–244, 2019.

[148] Yanyan Liu, Zhenlong Zhang, Huiping Gao, Huafang Zhang, and Yanli Mao. A novel inorganic hole-transporting material of cuins2 for perovskite solar cells with high efficiency and improved stability. *Organic Electronics*, 75:105430, 2019.

[149] R Teimouri and R Mohammadpour. Potential application of cusbs2 as the hole transport material in perovskite solar cell: a simulation study. *Superlattices and Microstructures*, 118:116–122, 2018.

[150] Pichaya Pattanasattayavong, Guy Olivier Ngongang Ndjawa, Kui Zhao, Kang Wei Chou, Nir Yaacobi-Gross, Brian C O'Regan, Aram Amassian, and Thomas D Anthopoulos. Electric field-induced hole transport in copper (i) thiocyanate (cuscn) thin-films processed from solution at room temperature. *Chemical Communications*, 49(39):4154–4156, 2013.